Preparing for a cosmological analysis of next generation radio observations

By

Glen Rees

A thesis submitted to Macquarie University
for the degree of Doctor of Philosophy
Department of Physics and Astronomy

July 2017

Acknowledgements

As I am sure is the case with nearly all PhD theses, I could not be sitting where I am today without the guidance and help of a huge number of people.

First and foremost to my supervisors. Ray, looking back on this incredible journey, I realise that meeting you has radically altered the course of my life. Had you not accepted a request from an unknown undergraduate student to come work for a year with you in Australia, I would likely never have considered even applying for a PhD. I would not have spent any of these amazing 6 years in Australia, nor met many of the most incredible people in my life. Thank you for taking that chance, for your continual mentorship and friendship, and for helping me transition from an excited and confused undergraduate, into a still very much excited, slightly less confused academic researcher. The enthusiasm and joy you bring to both your own work and others is truly inspiring!

Lee, I cannot believe how quickly these last 3.5 years have gone. It seems only yesterday that I met you for the first time, full of wild ideas for a PhD project. Thank you for your helpful explanations, your guidance and, especially in these last few months, your endless patience! Your dedication to rigour and in some cases sanity, has been the perfect counterpoint to my tendency towards endless speculation and desire for new projects. Without you I would likely never have stayed on one topic long enough to write a paper, let alone a whole thesis! Despite my endless grumbling I have truly enjoyed our years working together. Thank you for everything!

To my adjunct supervisor David, despite requiring nearly 26 hours on a plane each way, my visits to you at Portsmouth University have been some of my favourite parts of my PhD. Thank you for taking the time each trip to help me get settled in and for spending hours teaching me the math and coding behind cosmological predictions.

Thank you to Macquarie University for both enabling and financing my PhD Thesis via the International Macquarie University Research Excellence Scholarship scheme and to my co-sponsor, CSIRO Astronomy and Space Science for their financing of several overseas conference trips and astronomy training schools, which have allowed me to develop my research in collaboration with the assistance of world-class research scientists. Thank you to also to the University of Portsmouth's Institute for Cosmology and Gravitation for their both their financial contribution to my yearly visits and for letting me stay so long! I would like to also thank Sydney Observatory and its wonderful staff, both past and present for many fun nights' work. I have learnt a great deal about engaging the public with astronomy in my time there and made many new friends. You will no doubt be seeing more of me soon!

At each of my numerous institutes there have been far too many wonderful colleagues

to list here. From serious discussion and feedback to fun lunchtime conversations my time during my PhD has never been dull. Thank you to Amy Kimball for your patience and feedback on many different radio astronomy topics, to Greg Hellbourg for always reminding me that no matter how bad things get there's always time for wine and cheese, to Shari Breen for many mid-afternoon Coke breaks and to Robin Wark for your wonderful explanations of how to un-break a telescope! To my friends at Macquarie University; Mike, thank you for all our long conversations on AGN feedback, methodology and coding practises, your insights, ideas and humour never cease to encourage me. Colin, thank you for your patience and listening to me grumble about things, it really does help! To my good friend Alessandro, I will miss our discussions about life the universe and everything, Sydney will not be the same without you, find a way back here soon. PS your thesis looks amazing don't stress too much over it! A big thank you to all of the administrative staff that have made my life easier over the years, Lisa you made my budgeting and trip organisation a breeze!

I have come to realise that the best work is done as part of a team, not because there are more hands, but because the fun and sense of discovery is greatly amplified when there are others to share it with. To the ATLAS and ZFOURGE teams, thank you for all of your wonderful comments, feedback, presentations and discussions over the years. To our weekly Exgal lunch meeting for keeping it real, I think sometimes we all forget that science is not always best described by 'Eureka' but by other less polite words, hearing other people's trials (and later successes) is a great way to help stay motivated! To the EMU cosmology team; David, Faisal, Song and Jacobo, you guys are amazing, I really think we are on to something here!

Thank you to my basketball team, for helping make sure I survive this thing by keeping me (at least semi) fit!

Thank you to my second family; Jean, Jeff and Rayner for all the support over the years, for taking me in to your home and for making me part of your family! Thank you to my parents and family, its been far too long since we last saw each other in person, I'll be home soon!

Finally, thank you Vanessa, you have been there for me through thick and thin, through all the joys and despair and I couldn't have done it without you. I'm really looking forward to sharing new discoveries and finding new adventures with you for many years to come!

List of Publications

- **Rees, G. A.**; Norris, R. P.; Spitler, L. R.; Herrera-Ruiz, N.; Middelberg, E. *Are the hosts of VLBI-selected radio-AGN different to those of radio-loud AGN?*. Monthly Notices of the Royal Astronomical Society **Volume 458**, L49-L53 (2016)

- **Rees, G. A.**; Spitler, L. R.; Norris, R. P.; Cowley, M. J.; Papovich, C.; Glazebrook, K.; Quadri, R. F.; Straatman, C. M. S.; Allen, R.; Kacprzak, G. G.; Labbe, I.; Nanayakkara, T.; Tomczak, A. R.; Tran, K.-V. *Radio galaxies in ZFOURGE/NMBS: no difference in the properties of massive galaxies with and without radio-AGN out to $z = 2.25$*. Monthly Notices of the Royal Astronomical Society, Issue 3, **Volume 455, Issue 3**, 2731-2744 (2016)

- Caroline M. S. Straatman, Lee R. Spitler, Ryan F. Quadri, Ivo Labbe, Karl Glazebrook, S. Eric Persson, Casey Papovich, Kim-Vy H. Tran, Gabriel B. Brammer, Michael Cowley, Adam Tomczak, Themiya Nanayakkara, Leo Alcorn, Rebecca Allen, Adam Broussard, Pieter van Dokkum, Ben Forrest, Josha van Houdt, Glenn G. Kacprzak, Lalitwadee Kawinwanichakij, Daniel D. Kelson, Janice Lee, Patrick J. McCarthy, Nicola Mehrtens, Andrew Monson, David Murphy, **Glen Rees**, Vithal Tilvi, Katherine E. Whitaker *The FourStar Galaxy Evolution Survey12 (ZFOURGE): Ultraviolet to Far-infrared Catalogs, Medium-bandwidth Photometric Redshifts with Improved Accuracy, Stellar Masses, and Confirmation of Quiescent Galaxies to $z \approx 3.5$*. The Astrophysical Journal, **Volume 830, Issue 1**, 51 (2016).

- Cowley, Michael J.; Spitler, Lee R.; Tran, Kim-Vy H.; **Rees, Glen A.**; Labb, Ivo; Allen, Rebecca J.; Brammer, Gabriel B.; Glazebrook, Karl; Hopkins, Andrew M.; Juneau, Stphanie; Kacprzak, Glenn G.; Mullaney, James R.; Nanayakkara, Themiya; Papovich, Casey; Quadri, Ryan F.; Straatman, Caroline M. S.; Tomczak, Adam R.; van Dokkum, Pieter G. *ZFOURGE catalogue of AGN candidates: an enhancement of 160-μm-derived star formation rates in active galaxies to $z = 3.2$*. Monthly Notices of the Royal Astronomical Society, **Volume 457, Issue 1**, 629-641 (2016)

- Tomczak, Adam R.; Quadri, Ryan F.; Tran, Kim-Vy H.; Labb, Ivo; Straatman, Caroline M. S.; Papovich, Casey; Glazebrook, Karl; Allen, Rebecca; Brammer, Gabreil B.; Cowley, Michael; Dickinson, Mark; Elbaz, David; Inami, Hanae; Kacprzak, Glenn G.; Morrison, Glenn E.; Nanayakkara, Themiya; Persson, S. Eric; **Rees, Glen A.**; Salmon, Brett; Schreiber, Corentin; Spitler, Lee R.; Whitaker, Katherine E. *The SFR-M^* Relation and Empirical Star-Formation Histories from ZFOURGE* at $0.5 < z < 4$*. The Astrophysical Journal. **Volume 817, Issue 2**, 118 (2016)

- Straatman, Caroline M. S.; Labb, Ivo; Spitler, Lee R.; Glazebrook, Karl; Tomczak, Adam; Allen, Rebecca; Brammer, Gabriel B.; Cowley, Michael; van Dokkum, Pieter; Kacprzak, Glenn G.; Kawinwanichakij, Lalit; Mehrtens, Nicola; Nanayakkara, Themiya;

Papovich, Casey; Persson, S. Eric; Quadri, Ryan F.; **Rees, Glen**; Tilvi, Vithal; Tran, Kim-Vy H.; Whitaker, Katherine E. *The Sizes of Massive Quiescent and Star-forming Galaxies at z≈4 with ZFOURGE and CANDELS*. The Astrophysical Journal Letters, **Volume 808, Issue 1**, L29, (2015)

- Allen, Rebecca J.; Kacprzak, Glenn G.; Spitler, Lee R.; Glazebrook, Karl; Labb, Ivo; Tran, Kim-Vy H.; Straatman, Caroline M. S.; Nanayakkara, Themiya; Brammer, Gabriel B.; Quadri, Ryan F.; Cowley, Michael; Monson, Andy; Papovich, Casey; Persson, S. Eric; **Rees, Glen**; Tilvi, V.; Tomczak, Adam R. *The Differential Size Growth of Field and Cluster Galaxies at z = 2.1 Using the ZFOURGE Survey*. The Astrophysical Journal, **Volume 806, Issue 1**, 3 (2015).

- Tingay, S. J.; Macquart, J.-P.; Collier, J. D.; **Rees, G.**; Callingham, J. R.; Stevens, J.; Carretti, E.; Wayth, R. B.; Wong, G. F.; Trott, C. M.; McKinley, B.; Bernardi, G.; Bowman, J. D.; Briggs, F.; Cappallo, R. J.; Corey, B. E.; Deshpande, A. A.; Emrich, D.; Gaensler, B. M.; Goeke, R.; Greenhill, L. J.; Hazelton, B. J.; Johnston-Hollitt, M.; Kaplan, D. L.; Kasper, J. C.; Kratzenberg, E.; Lonsdale, C. J.; Lynch, M. J.; McWhirter, S. R.; Mitchell, D. A.; Morales, M. F.; Morgan, E.; Oberoi, D.; Ord, S. M.; Prabu, T.; Rogers, A. E. E.; Roshi, A.; Udaya Shankar, N.; Srivani, K. S.; Subrahmanyan, R.; Waterson, M.; Webster, R. L.; Whitney, A. R.; Williams, A.; Williams, C. L. *The Spectral Variability of the GHz-Peaked Spectrum Radio Source PKS 1718-649 and a Comparison of Absorption Models.*. The Astronomical Journal, **Volume 149, Issue 2**, 74, (2015)

- Kawinwanichakij, Lalitwadee; Papovich, Casey; Quadri, Ryan F.; Tran, Kim-Vy H.; Spitler, Lee R.; Kacprzak, Glenn G.; Labb, Ivo; Straatman, Caroline M. S.; Glazebrook, Karl; Allen, Rebecca; Cowley, Michael; Dav, Romeel; Dekel, Avishai; Ferguson, Henry C.; Hartley, W. G.; Koekemoer, Anton M.; Koo, David C.; Lu, Yu; Mehrtens, Nicola; Nanayakkara, Themiya; Persson, S. Eric; **Rees, Glen**; Salmon, Brett; Tilvi, Vithal; Tomczak, Adam R.; van Dokkum, Pieter *The Distribution of Satellites around Massive Galaxies at 1 < z < 3 in ZFOURGE/CANDELS: Dependence on Star Formation Activity*. The Astrophysical Journal, **Volume 792, Issue 2**, 103, (2014)

- Spitler, Lee R.; Straatman, Caroline M. S.; Labb, Ivo; Glazebrook, Karl; Tran, Kim-Vy H.; Kacprzak, Glenn G.; Quadri, Ryan F.; Papovich, Casey; Persson, S. Eric; van Dokkum, Pieter; Allen, Rebecca; Kawinwanichakij, Lalitwadee; Kelson, Daniel D.; McCarthy, Patrick J.; Mehrtens, Nicola; Monson, Andrew J.; Nanayakkara, Themiya; **Rees, Glen**; Tilvi, Vithal; Tomczak, Adam R. *Exploring the z = 3-4 Massive Galaxy Population with ZFOURGE: The Prevalence of Dusty and Quiescent Galaxies*. The Astrophysical Journal Letters, **Volume 787, Issue 2**, L36, (2014)

- Straatman, Caroline M. S.; Labb, Ivo; Spitler, Lee R.; Allen, Rebecca; Altieri, Bruno; Brammer, Gabriel B.; Dickinson, Mark; van Dokkum, Pieter; Inami, Hanae; Glazebrook, Karl; Kacprzak, Glenn G.; Kawinwanichakij, Lalit; Kelson, Daniel D.; McCarthy, Patrick J.; Mehrtens, Nicola; Monson, Andy; Murphy, David; Papovich, Casey; Persson, S. Eric; Quadri, Ryan; **Rees, Glen**; Tomczak, Adam; Tran, Kim-Vy H.; Tilvi, Vithal *A Substantial Population of Massive Quiescent Galaxies at z ≈ 4 from ZFOURGE*. The Astrophysical Journal Letters, **Volume 783, Issue 1**, L14, (2014).

Abstract

In order to prepare for a cosmological analysis of the next generation of radio continuum surveys such as the Evolutionary Map of the Universe (EMU), we here investigate the galaxy properties and cosmological clustering of radio sources in a number of existing large area surveys with high sensitivity. In order to understand the types of galaxy likely to be observed at radio frequencies, we investigate the host galaxy properties of radio sources as a function of redshift and mass out to a redshift of z = 2.25 and use the resulting relations to produce a new simulated radio continuum sky. We compare the measured angular clustering of galaxies in this simulation to both real observations (via two of the largest μJy surveys to date) and more traditional numerical models of angular clustering at 1.4 GHz.

Using cross identification of deep Very Large Array observations at 1.4 GHz with two deep Near Infrared (NIR) surveys, the FourStar Galaxy Evolution redshift survey (ZFOURGE) and the Newfirm Medium Band Survey (NMBS), we determine the galactic properties of 424 radio sources at flux densities greater than 50μJy in the COSMOS and CDFS fields. Both of these NIR surveys use medium band infrared filters to increase the accuracy of photometric redshifts at much earlier cosmic times than optical surveys. The wealth of ancillary data in these two fields is substantial, with up to 39 bands of photometry spanning from the ultraviolet to the far-infrared. This allows us to accurately estimate galaxy stellar-masses, star-formation rates and dust contents. Using this data we identify radio-loud AGN using their 1.4 GHz and NIR+UV based star-formation rates. Objects whose radio emission is consistent with the star-formation rate are classified as star-forming dominated sources and those whose emission at 1.4 GHz is greater than three times what is expected from the NIR+UV star-formation rate are classified as radio-loud AGN. We compare the host properties of these objects in a mass ($M_\odot \geq 10^{10.5}$ $M_\odot$) and luminosity ($L_{1.4} > 10^{24}$ W Hz^{-1}) complete sample against the galaxy properties of non-AGN hosts finding them to be in agreement across a broad range of redshifts ($0.25 \leq z < 2.25$). We determine the mass and redshift dependant radio-loud AGN fraction across the redshift range ($0.25 \leq z < 2.25$) finding that while radio-loud AGN show very little change in rarity between these epochs, they exhibit a strong dependence on the stellar-mass of their host galaxy.

Extending this work further, we utilise new Very Long Baseline Interferometry observations to study if these relations hold for a sample of AGN selected on the basis of their surface brightness temperature. We find that the relationship between VLBI detected sources (which provides an unambiguous confirmation of AGN activity) and the mass and redshift similar sample of non-AGN sources is identical to that of radio-loud AGN, and that VLBI surveys selected are not only a part of the radio-loud AGN population, but a representative sample.

To prepare for the EMU cosmology analysis we measure the clustering of bright ($S_{1.4} >$ 15 mJy) radio sources in the NRAO Very Large Array Southern Sky Survey, using both the

angular power spectrum and two point angular correlation function and find excellent agreement with previous work on this survey. In addition to this, we measure the observed clustering in the Jansky Very Large Array observations of Stripe-82 and the Australian Telescope Compact Array, Large Area Survey of the South Pole Telescope Field at 300μJy. We find that the radio sky at these lower flux limits is far less dominated by extended radio sources than at higher flux densities. Fitting the correlation function with a powerlaw at scales between 0.1 and 10 degrees yields results inconsistent with previous work at flux both above and below our current limits. This is due to a substantial over density of sources measured on scales of 0.1-0.3 degrees and removing these scales from the fit results in a measured powerlaw of amplitude A = $1.6 \pm 0.24 \times 10^{-3}$, with a slope of -0.8 ± 0.3 equivalent to a γ = 1.8. Using an inversion of the cosmological Limber equation we convert this measurement into the spatial correlation length $r_0^{\epsilon=0} = 2.2^{+3.4}_{-1.7}$ h^{-1} Mpc and find this to be in good agreement with previous studies. The substantial dependence of this cosmological analysis on a small number of elevated data points, shows just how important the need for accurate modelling of observational systematics can be.

We use the relationship between radio flux and star-formation rate as well as the relations found above, detailing the prevalence of radio-loud AGN as a function of stellar mass and redshift, to convert simulated catalogues based on the dark matter halos of the semi-analytic Millennium Simulation into an expected radio sky. We compare our observations against both this newly created simulation and more traditional numerical simulations of the expected auto correlation function. Both show moderate agreement with the corrected observations and we hope that in future work the easy addition of noise, bright side-lobes and extended sources to our new simulation will allow us to better understand and remove the effects of these issues from observations.

Contents

List of Figures

List of Tables

"In the beginning the Universe was created. This has made a lot of people very angry and been widely regarded as a bad move."

Douglas Adams

1 Introduction

From the dawn of time, how the Universe came to exist and our place in it, have been two of the biggest and most enduring questions ever posed. From the earliest myths and creation stories, through various philosophical constructions, to the vast and complicated modern day projects which allow us to study the Universe in the first few nanoseconds of its existence, humanity has always been striving to better understand how the world as we know it came to be and what its ultimate fate may be. 'Cosmology' is the modern day study of these questions. It focuses not on any individual object inside our cosmos, but the study of the Universe as a whole. It does this by combining a wide array of observations on the largest of scales, with the study of the very small, the physics of individual particles and collisions on atomic scales.

In the last few decades the precision of cosmological studies has increased significantly, and with it our understanding of the make up, creation and evolution of the Universe. This is due in no small part to the advent of both multi-wavelength astronomy, the huge increase in the size and depth of astronomical observations made possible by advancing technology and the synergistic combination of multiple cosmology probes.

In Figure 1.1 we show the sensitivity of various cosmological probes to the equation of state parameter (w) and mean matter density (Ω_m). From the measurements of Type Ia supernovae as standard candles (SN Ia, Kowalski et al., 2008), to the distribution of power in the CMB (WMAP, Dunkley et al., 2009), standard rulers such as baryon acoustic oscillations (BAO, Percival et al., 2010) to the observed abundance of galaxy clusters (Mantz et al., 2010) combined with cluster f_{gas} measurements (Allen et al., 2008), each of these cosmological probes provide new information to the combined constraints (Allen et al., 2011). It is this synergy that has allowed for the development of precision cosmology far beyond the systematic uncertainties inherent to any one individual technique.

In the coming years a number of new facilities will be brought on-line, once again leading to a large increase in cosmological sensitivity. Importantly for this work, some of these facilities (namely the Australian Square Kilometre Array Pathfinder and its successor the

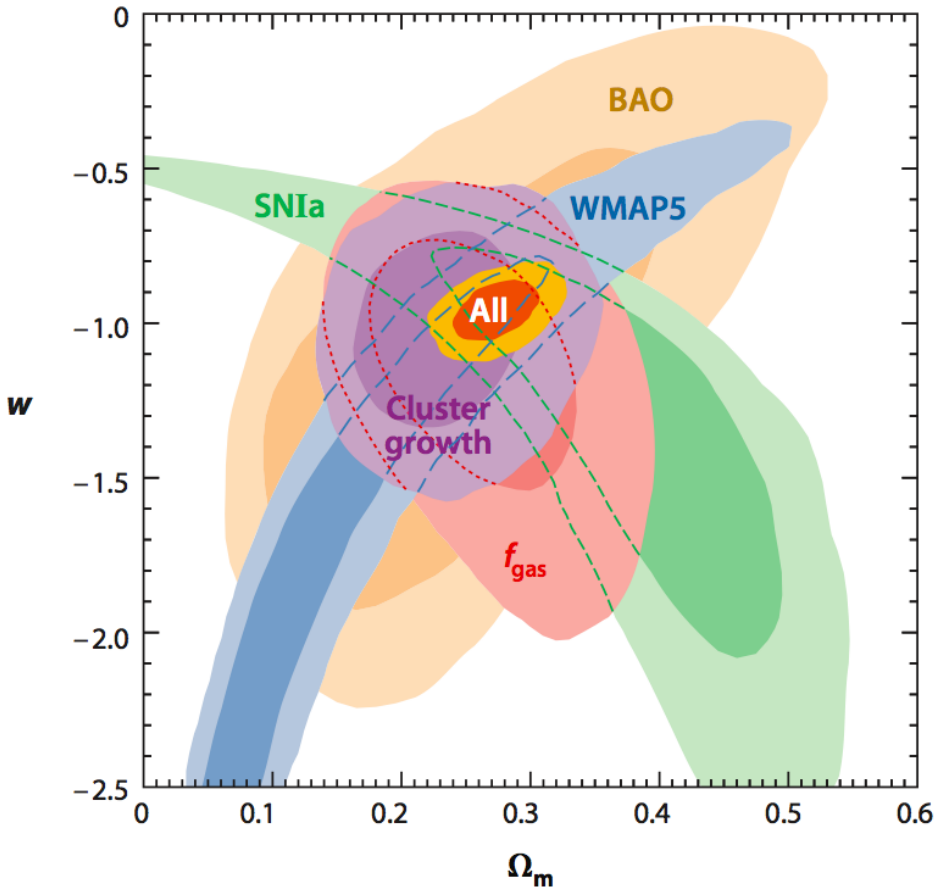

Figure 1.1: The synergy of cosmological constraints from galaxy clusters and other probes. Joint 68.3% and 95.4% confidence constraints on the dark energy equation of state, w, and mean matter density, Ω_m. Observed abundance and growth galaxy clusters (purple shading), cluster f_{gas} measurements (red shading), CMB structure (blue shading), type Ia supernovae (green shading) and baryon acoustic oscillations (orange shading) for spatially flat, constant w models. Gold contours show the results from the combination of all data sets. Figure credit: Allen et al. (2013)

Square Kilometre Array) will for the first time reach a sufficient depth and area to make cosmologically sensitive observations in the radio regime which are competitive to analyses at other wavelengths.

Before any of this work can commence however, it is important that we understand the nature of the sky we aim to study in terms of both the type of sources observed and the observational systematics that may impact our analysis. The large scale of the next generation of radio surveys makes accurate predictions for their cosmological sensitivity difficult and this is compounded by their reliance on numerous complex theoretical assumptions and simplifications needed to make such predictions possible. Similar assumptions are also used in modelling the observable effects of a given cosmology. As a result of this, both predictions for a survey's cosmological significance and the models used to fit observed cosmological effects are incapable of including systematic effects inherent to real observations. As such a more empirical process to simulate the cosmological underpinnings of real, imperfect, radio observations is needed and it is the first stages of this work that are presented in this thesis.

1.1 Motivation

1.1.1 Radio Cosmology

Until recently, the study of Cosmology at radio frequencies has been largely stymied by the relatively low number density of galaxies visible in this regime. Because of this, only a few of the largest continuum radio surveys to date, the NRAO Very Large Array Sky Survey (NVSS, Condon et al., 1998), the Faint Images of the Radio Sky at Twenty Centimetres (FIRST, Becker et al., 1995), the Sydney University Molonglo Sky Survey (SUMSS, Mauch et al., 2003) and the Westerbork Northern Sky Survey (WENSS, Rengelink & et al., 1998), reach both the depth and coverage necessary for useful cosmological analysis. See Section 1.2.4 for a more in depth discussion.

Despite this, predictions for the cosmological sensitivity for the next generation of deep radio observations are encouraging (Raccanelli et al., 2011; Camera et al., 2012). Once radio surveys reach a depth and scale where they are detecting significant numbers of galaxies, then the tendency for radio objects to inhabit higher redshifts than their optical and infrared counterparts, coupled with their high sensitivity to variations in the underlying Dark Matter halos (known as their 'bias', Kaiser, 1984; Bardeen et al., 1986) makes them an ideal tracer for cosmological effects across a wide range of redshifts.

One such upcoming radio survey is the Evolutionary Map of the Universe (EMU Norris et al., 2011). EMU is a deep, all-sky radio continuum survey that is being planned for the Australian Square Kilometre Array Pathfinder. It aims to reach a continuum sensitivity of 10 μJy across 80% of the sky and in combination with its northern hemisphere equivalent, the Westerbork Observations of the Deep APERTIF Northern-Sky (WODAN Oosterloo et al., 2009) will provide all-sky radio continuum coverage nearly 40 times deeper than previous all or near-all sky radio surveys (see Appendix A for a comparison of many existing and upcoming radio continuum surveys). At this sensitivity, EMU alone is predicted to observe $\approx$ 70 million new radio galaxies (Norris et al., 2011) and as a result of this, continuum radio surveys are now expected have sufficient source counts to produce truly competitive cosmological constraints for very the first time.

1.1.2 Cosmological Probes

The cosmological sensitivity of these predicted constraints (Raccanelli et al., 2011; Camera et al., 2012) comes from the synergy inherent to any combined analysis of several different cosmological effects. The first of these is the late time Integrated Sachs-Wolfe effect (ISW). First predicted in 1967 (Sachs & Wolfe, 1967) the ISW is the effect an accelerating space-time expansion has on light from the Cosmic Microwave Background (CMB) as it passes through the gravitational potential gradients associated with large scale structures such as super-clusters and voids. Falling into large gravitational potentials, the CMB photons gain energy, driving up their frequency. In a non-accelerating universe this energy is lost as the light begins to climb back out of the potential well, for zero net change in energy. In an accelerating Universe however this process is not balanced, the dominance of Dark Energy in the equation of state at late times means that the potential well of the cluster evolves significantly over the crossing time. Because of this the gravitational potential well is much

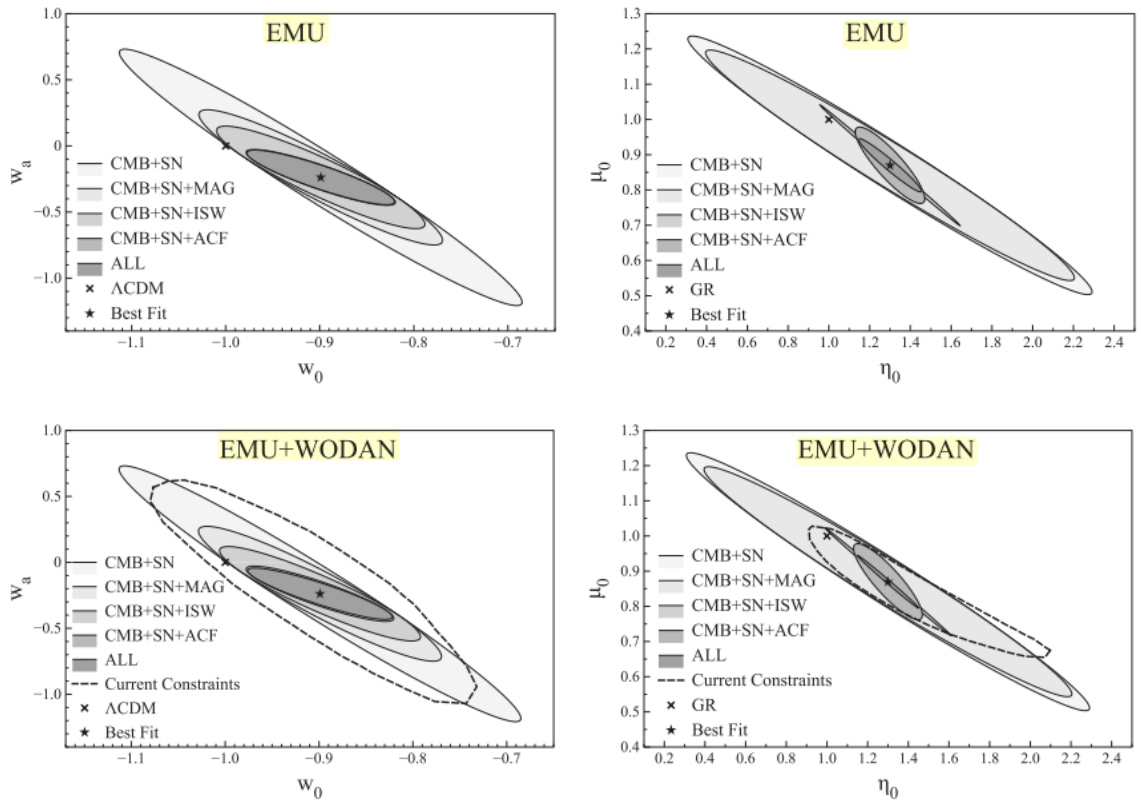

Figure 1.2: The predicted sensitivity of EMU & EMU+WODAN to the two time- and scale-dependent modified gravity functions (η_0, μ_0) and the equation of state parameters (w_0, w_a) by Fisher matrix analysis, as from Raccanelli et al. (2012). Top: The predicted EMU cosmological sensitivity when combining various cosmological probes: Cosmic Magnification (MAG), the Integrated Sachs-Wolfe Effect (ISW), and Angular Correlation Functions (ACF) with constraints from other surveys: Cosmic Microwave Background analysis and Super Nova constraints (SN). Bottom: We can see that EMU + WODAN or even EMU alone will provide new constraints on current cosmological models

shallower during the photons climb back out and hence a net gain in energy is experienced. The inverse of this process is also true, with photons spending energy to climb into voids which also diminish over the crossing time, resulting in a net loss of energy.

Detectable by correlating anisotropies in the CMB with large scale structures found in the local distribution of galaxies, the ISW will provide constraints to both the type and magnitude of Dark Energy. Galaxy density maps from a wide range of surveys such as the Wide-field Infrared Survey Explorer (WISE, Wright et al., 2010), the Sloan Digital Sky Survey (SDSS, York et al., 2000; Alam et al., 2015), the infrared 2 Micron All-Sky Survey (2MASS, Skrutskie et al., 2006), the X-ray catalogue from the High Energy Astrophysical Observatory (HEAO Wood et al., 1984) and the NRAO VLA Sky Survey of radio galaxies (NVSS, Condon et al., 1998) have all been cross correlated with CMB maps from both the Wilkinson Microwave Anisotropy Probe (WMAP, Spergel et al., 2007; Bennett et al., 2013) and Planck (Planck Collaboration et al., 2013). Unfortunately the vast majority of these attempts find only tentative detections of the ISW effect at any wavelength, with neither optical (Scranton et al., 2003; Cabré et al., 2006), infrared (Afshordi et al., 2004; Rassat et al., 2007)

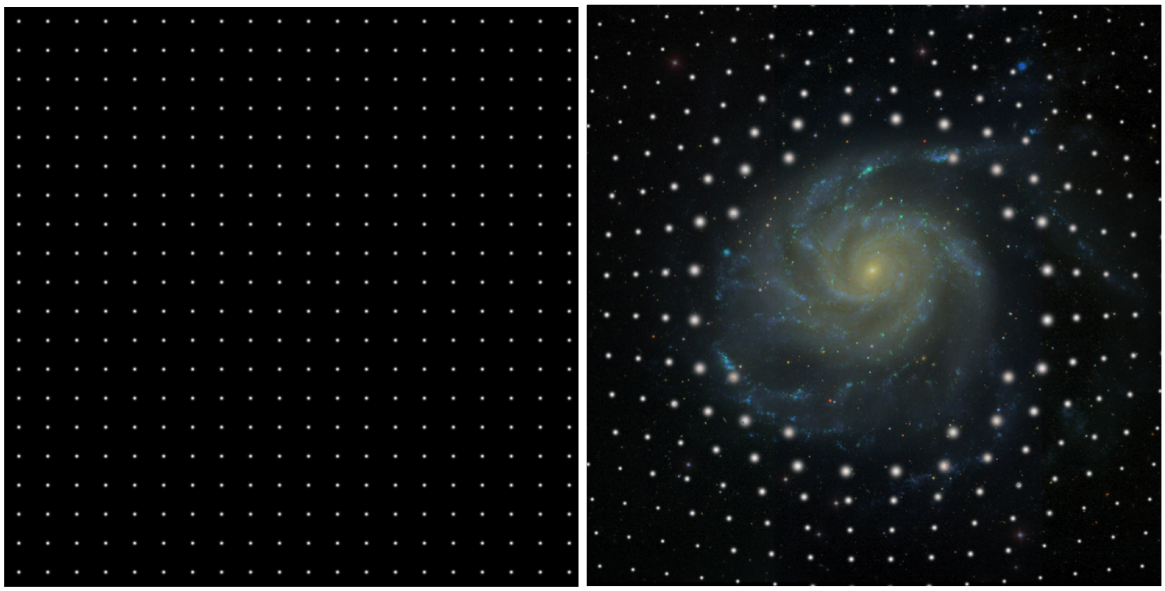

Figure 1.3: A simple example of Cosmic Magnification showing the effect of weak gravitational lensing on background sources. By placing a foreground galaxy over a uniform distribution of distant background sources, the conflicting effects of Cosmic Magnification can clearly be seen. In detail, the spreading of sources over a large area, thereby decreasing source surface density can be seen competing with the effect of boosting weak objects into a surveys sensitivity regime, thereby increasing the source surface density. Credit: Joerg Colberg, Ryan Scranton, Robert Lupton, SDSS

nor radio (Boughn & Crittenden, 2004; Nolta et al., 2004) reaching significances above 2-3σ, as ISW induced variations are small compared to the innate anisotropies of the CMB itself. Four notable exceptions to this trend are the results of Giannantonio et al. (2008); Ho et al. (2008) and later again in Giannantonio et al. (2012, 2014) who found a 3.7-4.5σ detection of the ISW using combined catalogues of all large scale galaxy data sets. With EMU, the ISW effect is expected to be readily detectable (Raccanelli et al., 2011; Camera et al., 2012; Jarvis et al., 2015).

The next cosmological effect that will be probed by the EMU survey is the Galaxy Magnification or Cosmic Magnification effect. Cosmic Magnification refers to the weak lensing of distant, background galaxies in the early universe, by their late-time local counterparts. Distinct and separate to Cosmic Shear (Mellier et al., 2003) which studies the distortion of weakly lensed galaxies shapes to determine cosmology, and strong lensing which provides accurate measurements of the dark matter content of galaxy clusters, Cosmic Magnification is the interplay of two competing lensing sub-effects. The distortion of space-time by massive foreground galaxies increases the apparent magnitude of distant sources, thereby increasing the number of detected objects for a given survey sensitivity. In opposition to this effect, the lensing will also spread out the apparent position of galaxies, lowering the source surface density at the populations average redshift (Figure 1.3).

Detectable by correlating foreground galaxy populations with background sources, Cosmic Magnification has been a popular choice for studies aiming to constrain Dark Matter properties as well as those aiming to determine the galaxy bias function (a measure of how sensitive galaxies are to Dark Matter density) which is a key component in galaxy evolution

models. Unfortunately the majority of previous studies have yielded inconclusive results, with the most solid detection of Cosmic Magnification being the 8σ (Scranton et al., 2005) detection of the Galaxy-Quasar correlation in the SDSS survey. More recently, studies in the sub-mm regime have shown promising results in the detection of this effect, as steep change in number counts with flux and high average redshift of sub-mm galaxies make them a perfect sample of background sources (Hildebrandt et al., 2009; Wang et al., 2011). For similar reasons to the sub-mm regime, the expectations of Cosmic Magnification detections in deep radio surveys such as EMU is also high, as the combination of optical, HI or near infrared foreground samples combined with high redshift (and high bias) radio galaxies will provide an ideal foreground/background selection function.

Finally the last major cosmological effect we aim to probe with EMU, and the effect most pertinent to this thesis, is the large scale structure traced by radio galaxies themselves. To explain the cosmological sensitivity of such measurements, one must consider the earliest stages of the Universe. Prior to the epoch of last scattering the Universe, consisting of a photon-baryon fluid, is dominated by the forces of radiation pressure and gravity. Shortly after this time temperatures fall low enough for photons to decouple from this fluid and pass without interaction through the now transparent Universe, to be detected after substantial redshifting, as the Cosmic Microwave Background. The uniformity of the Universe at the time of the CMB's emission was high, however tiny inhomogeneities generated by the enlargement of quantum fluctuations during the inflation period result in over dense regions of Dark Matter. The newly decoupled baryonic matter, now no longer supported by radiation pressure, collapses into the potential well of this underlying dark matter distribution and begin the formation of the first stars and galaxies. With the continual growth of dark matter halos with time (traced by galaxy clustering) the large scale structure of galaxies can provide valuable constraints on cosmology at both early and late times.

Alone, the cosmological constraints from EMU will be competitive (Raccanelli et al., 2011; Camera et al., 2012). Combined with the latest results from Planck, Supernova studies and other cosmological surveys however, they are expected to offer a significant reduction in the errors on a variety of Dark Energy and Modified Gravity properties (Figure 1.2). This is largely due to the highly synergistic nature of radio cosmology, as it best constrains cosmological parameters where other surveys are weakest. In addition to this the combined measurements are also far less sensitive to systematic uncertainties in any one observation, providing a robustness against survey dependent errors. Finally, all of these predictions assume a complete lack of redshift information for newly detected radio sources. However, the acquisition of redshift information for these sources is not beyond the realm of possibility and deep photometric or even statistical redshifts are now predicted to allow radio surveys to reach even greater cosmological sensitivity (Camera et al., 2012).

1.1.3 The problem with existing cosmology simulations

The predictions discussed in Section 1.1.2 use a Fisher Matrix analysis based on numerical simulations of the radio sky, to produce the best case constraints on a wide range of cosmological properties. Such analysis can be a powerful tool for identifying areas of research that have hidden potential and indeed, the identification of the EMU survey as having cosmological potential is an excellent example of this. Despite the usefulness of such predictions

however, they use theoretical rather than empirical distributions for galaxies and have no method by which to model the impact of observational artefacts.

To illustrate the importance of such issues, we here outline part of the process by which these predictions are made. Importantly the steps used here are also used in the modelling of each cosmological probe outlined in Section 1.1.2 and as such are part of the process that will eventually be used to fit observables, such as the correlation functions and power spectra, to cosmological parameters.

The starting point of any cosmological model is to simulate the distribution of dark matter given a set of cosmological parameters. The clustering of these dark matter halos then can be represented by a spatial power spectrum, P(k) and it is this which we sample using the radial selection function of our survey to produce the expected Angular Power Spectrum, C_ℓ,

$$C_\ell = \frac{2}{\pi} \int_0^\infty W_\ell(k)^2 P(k) k^2 dk, \tag{1.1}$$

where P(k) is the dark matter spatial power spectrum and W_ℓ(k) is the radial selection function:

$$W_\ell(k) = \int_0^\infty j_\ell(kr) B(z) \frac{dp(z)}{dz} dr. \tag{1.2}$$

Here j_ℓ is a Spherical Bessel Function and p(z) is the probability redshift distribution of galaxies normalised such that its integral between zero and infinity is equal to unity. The linear bias estimator b(z) is a dimensionless bias of order unity and is simply the ratio between the power spectra of galaxies in the chosen sample and the power spectra of dark matter (Kaiser, 1984; Bardeen et al., 1986).

Observationally the bias function of radio galaxies has been derived for a wide selection of fluxes. Using the NVSS survey at 1.4 GHz Blake & Wall (2002b) measured a constant linear bias of 1.8 for radio sources brighter than 15mJy. Results from the Galaxy and Mass Assembly (GAMA) survey have been used to constrain the linear bias of bright (S>1mJy) low redshift (z≈0.34) radio galaxies detected in FIRST to b≈1.9, and find this to increase dramatically up to b≈10 between redshift 0.3 and 1.55 (Lindsay et al., 2014). These bias constraints were later extended to fainter radio sources (S>90μJy) and higher redshifts (z_{max} ≈ 2.2) using VIDEO and CFHTLS data in combination with the VLA VIRMOS Deep Field, finding that the bias of faint radio sources is also evolving, from 0.57±0.06 at redshift of 0.3 to 8.55± 3.11 at z=2.2 (Lindsay et al., 2014). Overall the bias at these faint flux levels is considerably greater than expected, particularly at high redshifts and this is suggested to be due to low luminosity Fanaroff Riley Type I galaxies (Fanaroff & Riley, 1974) sources possessing a higher bias than previously predicted.

At high flux densities the redshift distribution of sources in the optical and infrared regime is well constrained. However at radio wavelengths the optical hosts of bright radio AGN are quite often far fainter than their radio counterparts, making spectroscopic or photometric redshift estimates exceedingly difficult to obtain for complete samples of radio galaxies. Because of this, previous analyses have used either luminosity-function models. For example, the luminosity function of Dunlop & Peacock (1990) were used in Blake et al.

(2004), or more recently for lower flux densities, the redshift distribution of the SKA Simulated Skies Semi-Empirical Extragalactic Simulation, (SKADS, Wilman et al., 2008).

The SKADS Simulations draw together a large number of observational results to predict redshift distributions for a wide variety of radio source types across several orders of magnitudes of radio fluxes. For the purpose of reproducing large scale structure, SKADS populates its underlying dark matter density field with radio galaxies using theoretical biases, resulting a in a measured correlation function at 3-30mJy that is in good agreement with results of Overzier et al. (2003). However at higher flux densities their agreement with results breaks down and it is noted that this is most likely a result of their crude estimate for bias.

At lower fluxes this problem is also noticeable, with the bias of radio sources measured by Lindsay et al. (2014): b = 3.8 ± 1.2 at z ≈ 1.3 to b = 8.55 ± 3.11 at z ≈ 2.2 for 90μJy sources, being considerably higher beyond redshift of z=1 than that predicted by SKADS at the same flux level (b=2.5 at z ≈ 1.3 to b=3.2 at z ≈ 2.3). This particular discrepancy is attributed to the underestimation of the bias of Faranoff-Riley Type I sources in the simulation but may also be due to the underestimation of host halo mass for these objects (White et al., 2007; Brown et al., 2008; Zehavi et al., 2011) which can cause a rapid apparent growth in bias with redshift. Finally recent work indicates that the redshift distribution of SKADS sources at the μJy level may not be entirely consistent with observations (Whittam, 2014).

Despite all of the above issues SKADS provides a consistent, if slightly inaccurate, framework across multiple redshifts and flux densities in which we can easily compare observations. Indeed, the primary problem with current predictions is not just that the bias or redshift distribution is inadequately modelled, but that numerical models have no way in which to include observational systematic effects. SKADS itself is one possible solution to this issue, as it is possible to produce catalogues of sources from its simulated images, thereby introducing effects such as side-lobes, noise and varying surface density to the predicted auto and cross correlation functions. Due to surface density variations the majority of analyses were performed at well over 30 times the nominal rms of the survey. Even at these high signal to noise ratios, systematics may still have a significant impact (Blake & Wall, 2002b; Overzier et al., 2003; Blake et al., 2004; Chen & Schwarz, 2015). In particular, unusual disagreement can be seen between the correlation functions of Blake & Wall (2002b), Overzier et al. (2003), Blake et al. (2003) and Lindsay et al. (2014) on scales of 0.1-0.3 degrees.

At a variety of flux density levels these scales show significant variation. In the Blake & Wall (2002a) analysis of NVSS at S > 15mJy there is little or no deficit at these scales (Figure 1.4: Top Left) but in Blake & Wall (2002b) NVSS at 10mJy (Figure 1.4: Top Right) shows a substantial deficit at these scales which is attributed to the over-cleaning of flux from sources falling within the first side-lobe of the radio telescopes beam, which is also present in the Overzier et al. (2003) analysis of NVSS sources over 10mJy.

In the FIRST survey however this under density is less well established. Blake & Wall (2002b) find a significant bump in the correlation function of FIRST at S >10 mJy and S>2 mJy between 0.08-0.1 degrees (Figure 1.4: Middle Left) followed by a deficit between 0.1-0.3 degrees. Contrary to this Overzier et al. (2003) find see no evidence for this deficit at 0.1-0.3 degrees for S > 3 mJy sources (Figure 1.4: Middle Right) or 10 mJy < S < 40 mJy

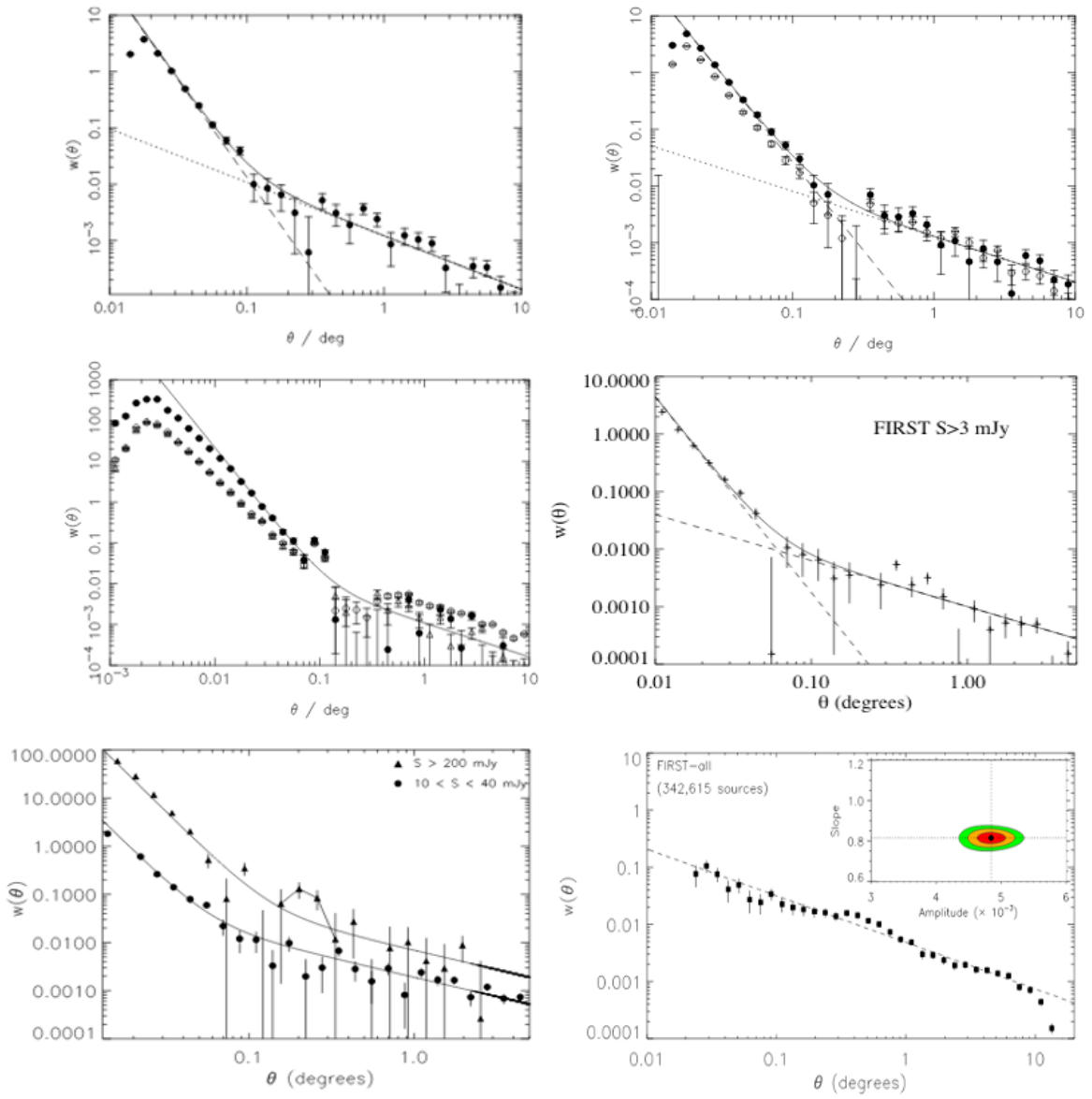

Figure 1.4: Auto correlation functions from previous work. The NVSS S > 15 mJy correlation function (top left). The NVSS S > 10 mJy and 20 mJy correlation function (top right, open and closed circles respectively). The Blake et al FIRST S > 2 mJy and 10 mJy correlation function (middle left, open and closed circles respectively). The Overzier et al FIRST S > 3 mJy correlation function (middle right, black crosses) and the Overzier et al FIRST S > 200 mJy and 10 mJy < S < 40 mJy correlation function (bottom left, black triangles and black circles respectively). Finally the Lindsay et al FIRST S > 1mJy correlation function (black circles)

.

sources (Figure 1.4: Bottom Left), but do see an elevation at 0.1-0.3 degrees for bright sources S > 200mJy (Figure 1.4: Bottom Left).

Finally Lindsay (2015) report a slight elevation at 0.2-0.6 degrees in FIRST at S > 1mJy (Figure 1.4: Bottom Right) and see a significant bump in the correlation function at 0.1-0.3 degrees when using only those FIRST S > 1mJy sources that have a GAMA counterpart. The exact cause of many of these discrepancies remains unknown, while there is some evidence to suggest these are the effects of badly masked side-lobes or the over or under cleaning of sources near bright objects. It is also possible that they are the effects of poor masking of local Galaxy structure or even real density perturbations on the scale of the local group at the typical radio galaxy redshift of z=1.

1.1.4 The problem with existing radio simulations

SKADS covers an area of approximately 25 square degrees, representing almost the complete field of view of any one instantaneous pointing with a Phased Array Feed interferometer. As such it is one of the largest radio continuum simulations to date, containing nearly 275 million sources at its simulated flux limit of 10 nJy. Despite this huge simulated volume however, SKADS is simply insufficient in size for the modelling of cosmological effects on large scales.

Of course, such issues regarding the scope of realistic simulations are not limited to the radio regime alone. The optical galaxy survey DES (The Dark Energy Survey, Dark Energy Survey Collaboration et al., 2016) provides a useful illustration of SKADS like simulations, as well as efforts being taken to overcome them. DES are seeking to produce cosmological constraints from optical galaxies using many of the same cosmological effects as outlined above. Recently DES has made use of the MICE-Grand Challenge N-body simulation (Fosalba et al., 2015) to produce expected auto and cross correlation functions and power spectra, for a 150 square degree area matching the expected sensitivity and coverage of the DES survey verification data, thereby allowing them to begin determining the expected clustering of their optical sources while including the effects of observational artefacts such as side-lobes and varying survey sensitivity. The full MICE simulations covers an area of nearly 5000 square degrees and contains not only cosmological clustering but also magnification and shear based lensing effects. As such semi-analytical N-Body simulations can be ideal test beds for determining more realistic estimates of the cosmological sensitivity as well as identifying potential issues with survey design. However, such simulations are mostly limited to the optical and infrared wavelengths. What is needed, is a way to accurately convert such large simulations into the radio regime and this thesis provides the first step in this direction.

1.2 Correlation Functions and Power Spectra

In this thesis we focus on predicting, measuring and simulating just one of the three EMU cosmology probes outlined above, the large scale structure of radio galaxies.

The most accurate representations of large scale structure is the three dimensional power spectrum P(k) which quantifies clustering as a function of co-moving wave-number k, or its

real space equivalent, the spatial correlation function ξ(r) which quantifies it as a function of co-moving separation radius, r. In practice however, determining these spatial clustering properties is prohibitively time consuming for large areas, as it requires the determination of spectral or photometric redshifts for each galaxy observed. Such ancillary observations will be not be available for the vast majority of EMU radio sources. A useful alternative then, is to use the angular positions of galaxies without any redshift information at all.

Such an analysis is made possible by the fact that, above k = 0.01 Mpc^{-1} (which corresponds to the horizon scale at the end of the radiation dominated era) the present day power spectrum is reasonably modelled by a power-law of the form:

$$\mathrm{P(k)} \propto \mathrm{k}^3 \ln(\mathrm{k}/\mathrm{k_{eq}})^2. \tag{1.3}$$

while departures from this form are now known (Zehavi et al., 2011) we still assume this form in order to compare against all previous cosmology work at radio wavelengths. This power-law like power spectrum has been shown to project onto the sphere of the sky as another power-law (Peebles, 1980) of the form:

$$\xi(r) = \left(\frac{r}{r_0}\right)^{-\gamma}, \tag{1.4}$$

$$\omega(\theta) = A\theta^{1-\gamma}, \tag{1.5}$$

for the spatial and angular correlation functions respectively where γ is the slope of the power law function.

The 2D representation of this 3D structure invariably suffer from some loss of information. However, angular clustering measurements can be carried out over much greater areas of sky and at much higher redshifts than their spatial counterparts, as without the need for extensive multi-wavelength follow-up, they require far less observing time. Furthermore, the increase in the sampled cosmic volume, allows a greater number of galaxies to be observed, driving down the sampling noise on the clustering measurement and results in the probing of much greater scales than is currently feasible in spatial clustering techniques.

Two primary methods exist for measuring the angular clustering of galaxies, the angular correlation function $\omega(\theta)$ and the angular power spectrum C(ℓ).

1.2.1 The Auto Correlation Function

The angular two point correlation function $\omega(\theta)$ can be defined as the excess in probability of finding a galaxy pair separated by the angle θ above the expected number of random pairs separated by θ in a Poissonian distribution (Peebles, 1980). One of several standard estimators of this function is the method of Landy & Szalay (1993) which determines the correlation function as:

$$\omega(\theta) = \frac{DD}{RR} - \frac{2DR}{RR} + 1, \tag{1.6}$$

where DD represents the number of galaxy pairs separated by $\theta \rightarrow \delta\theta$, RR represents the same for a randomly generated distribution of sources, DR is the random to real pair counts To account for variation in the randomly generated sources we calculate $\omega(\theta)$ for one thousand independent realisations of the randomly generated sources. The final $\omega(\theta)$ is given by the average of these runs with the error given by the standard deviation of the one thousand runs.

While this correlation function should be well fitted with a power-law of the form given in Equation 1.5, for radio galaxies $\omega(\theta)$ it has been found to be best fitted in practice, by a two component power law due to contamination at scales less than 0.1 degrees by the extended hotspots and jets of large radio galaxies (Blake & Wall, 2002a).

1.2.2 The Angular Power Spectrum

At large angular separations it is better to estimate the clustering of galaxies via their angular power spectrum $C(\ell)$ which quantifies the large scale structure of galaxies by breaking down the galaxy density field into its spherical harmonics as a function of the multipole moment, ℓ, where $\ell \approx 180/\theta$ with θ measured in degrees. $C(\ell)$ is best constrained at small values of ℓ, corresponding to large angular scales. While more in depth explanation of the methodology used to calculate $C(\ell)$ observationally is included in Section 4.4.2, it can be related to the angular correlation function using Equation 1.7, where σ_0 is the average source density in sources per steradians and P_ℓ are the Legendre Polynomials,

$$C_\ell = 2\pi\sigma_0^2 \int_{-1}^{+1} \omega(\theta) P_\ell(\cos\theta)\, \delta(\cos\theta). \tag{1.7}$$

It is possible in theory to fit multi-parameter cosmology models to either of these observations by converting simulated dark matter power spectra into predicted angular galaxy power spectra and correlation functions. However for the current generation of radio surveys the error bars on these measurements, dominated by shot noise, are not competitive with cosmological surveys at other wavelengths. Instead studies have focused on determining the amplitude and slope of angular clustering measures, in order to calculate such properties as the bias, and (via an inversion of the cosmological Limber equation) the spatial correlation length r_0 of radio galaxies.

1.2.3 The Limber Inversion

The Limber equation (Limber, 1953; Peebles, 1980) is used to relate the spatial correlation function $\xi(r)$ to the angular power spectrum $\omega(\theta)$ in terms of the observed spatial correlation length r_0. It is especially useful when direct calculation of the spatial correlation function is not possible, for example in large radio surveys with insufficient ancillary data to determine distances, and provides a characteristic length of spatial clustering, r_0, where r_0 is the spatial scale at which $\xi(r)$ is equal to one.

In order to calculate r_0 we must measure the amplitude, A, and slope, b=1-γ, of the angular auto-correlation function. We must also assume a redshift distribution for the survey,

a form for the spatial correlation function and the evolution parameter, ϵ to be used. While we have discussed the existing issues with the redshift distribution of faint radio sources in Section 1.1.3, the SKADS simulations nevertheless remain an excellent combined framework for the redshift distribution of sources at varying flux densities and hence our assumed redshift distribution for our Limber inversions is taken from this simulation. The spatial correlation function used in this calculation is given in Equation 1.7. Finally, we calculate r_0 for three differing evolution parameters, $\epsilon = 0$, γ-1 and γ-3. These three values of ϵ correspond to three differing clustering models (Phillipps et al., 1978; Kundić, 1997). $\epsilon = 0$ corresponds to a clustering model in which galaxy clusters are gravitationally bound at small scales and hence have a fixed physical scale. $\epsilon = \gamma$-3 equates to a clustering model that expands with the growth of the Universe and $\epsilon = \gamma$-1 which corresponds to cluster growth under linear perturbation theory. A fuller description of the Limber calculation is given in Section 4.4.1

1.2.4 Previous Radio Cosmology Results

The angular auto-correlation function has been independently determined multiple times for both the FIRST and NVSS surveys at 1.4 GHz as well as the SUMSS survey at 843 MHz. Blake & Wall (2002a) measured for the first time the amplitude of this correlation function at scales dominated by cosmological effects, finding the amplitude of the correlation function A $= 1.12 \times 10^{-3}$ with a fixed γ (i.e fixed slope) of 1.8 for S > 15 mJy sources. Using the Limber inversion (see Section 1.2.3) they calculated the spatial correlation length r_0 to be $r_0^{\epsilon=\gamma-3} \approx 3.6\ h^{-1}$ Mpc. However, in order to achieve this success, the vast majority of sources in NVSS must be ignored, due to varying sensitivity across the field and the fact that a number regions must be masked due to false detections caused by the side-lobe response of the telescope to very bright sources. This work was later extended to include the FIRST survey at similar flux density levels, confirming the γ value measured in previous work (Blake & Wall, 2002b).

In 2003 a similar analysis was performed at lower radio frequencies using the Sydney University Molonglo Sky Survey (SUMSS). They derive a steeper slope for the angular auto-correlation function of -1.1, equating to a γ of 2.1 (Blake et al., 2003). As this paper revised upwards the results of the two previously discussed studies, they find no evidence to suggest the correlation function changes as a function of frequency. Simultaneous to this study a combined angular auto-correlation analysis of the FIRST and NVSS surveys was produced by Overzier et al. (2003). They found that the cosmologically dominated scales of $\omega(\theta)$ at S > 10mJy in NVSS, and S > 3mJy in FIRST, were consistent with a slope of $\gamma = 1.8$ and an amplitude A $\approx 1 \times 10^{-3}$. Using the Limber inversion they calculated the spatial correlation length of NVSS as a function of flux, finding that while it decreases log linearly between 30 and 200mJy it remains nearly constant between 3-30mJy at $r_0^{\epsilon=\gamma-3} \approx 6\ h^{-1}$ Mpc. Ruling out the effects of projection as the cause of this effect, they suggest that this is possibly caused by powerful radio sources being intrinsically more clustered than average power radio sources.

This is consistent with the later findings of Lindsay (2015) which determine the bias function of high-luminosity FRII radio galaxies is higher than previously expected and significantly elevated over the bias of less luminous FRI objects.

Finally, recent work has made use of a pixel based two point correlation estimator and compared it to the Landy & Szalay (1993) method, finding this new method in good agreement at scales larger than a 5 degrees (Xia et al., 2010). Building on this work Chen &

Schwarz (2015) re-measure the angular auto correlation function of the NVSS survey using a more advanced masking method than that used in Blake & Wall (2002a). They find that their mask improves the quality of the powerlaw fit to the correlation function and that after correcting for the radio-dipole the correlation function shows no indication of primordial non-Gaussianity out to $\theta = 20$ degrees when comparing to model predictions.

In addition to the angular auto correlation function, the angular power spectrum of NVSS has also been measured observationally. Blake et al. (2004) produce two separate measures of the angular power spectrum, one via a direct spherical harmonic analysis and the other via a maximum likelihood analysis. They find that the methods yield results in good agreement with one another and are reproduceable using standard models for the present-day spatial power spectrum P(k) and the expected radial distribution of NVSS sources, p(z). Finally they determine that a linear bias of $b_0 = 1.7 \pm 0.17$ provides a good fit of the observed power spectrum when normalising over all other cosmological parameters.

1.3 Understanding the μJy Continuum Radio Sky

In order to produce a method to convert cosmological simulations at optical or infrared wavelengths to the radio regime, we must first understand both the types of objects apparent at each wavelengths and the emission processes that power them.

1.3.1 Radio Emission from Star-formation Processes

At 1.4 GHz there are two primary continuum emission processes driven by the life cycles of stars. The first of these is Free-Free radiation, also known as Thermal Bremsstrahlung as at high optical densities it results in a thermal radiation profile, refers to emission driven by the acceleration of free electrons by their interaction with ionized gas. It is commonly detected from dense HII regions that are being ionised by nearby high luminosity stars (Guesten & Mezger, 1982). Since the intensity of free-free radiation is proportional to the production rate of Lyman continuum photons (Condon, 1992), it is also indirectly proportionate to the number of local massive stars, and, via the relatively short life expectancy of massive stars, to the recent local star-formation rate. At EMU's observing frequency of 1.4 GHz we can see in Figure 1.5 the contribution from free-free emission will usually be undetected at extra galactic distances because, with the exception of very high redshift sources, our observed frequency corresponds to rest-frame frequencies where the free-free emission is proportionate to, and considerably less than the flux produced by the other main type of stellar based radio emission; synchrotron emission from electrons accelerated by supernova shocks.

The synchrotron process produces continuum radio emission as a result of relativistic electrons passing through strong magnetic fields. The magnetically induced change in direction (as the electron spirals through the magnetic field) results in a continual loss of its energy via photons. When this effect is averaged across many electrons of varying initial velocity the result is broad emission profile across a large range of frequencies. At frequencies less than 30 GHz synchrotron radiation is the dominant emission process and in the absence of additional AGN driven synchrotron emission, the majority of flux at these wavelengths is produced by cosmic ray electrons (which have been accelerated by shocks from Supernova)

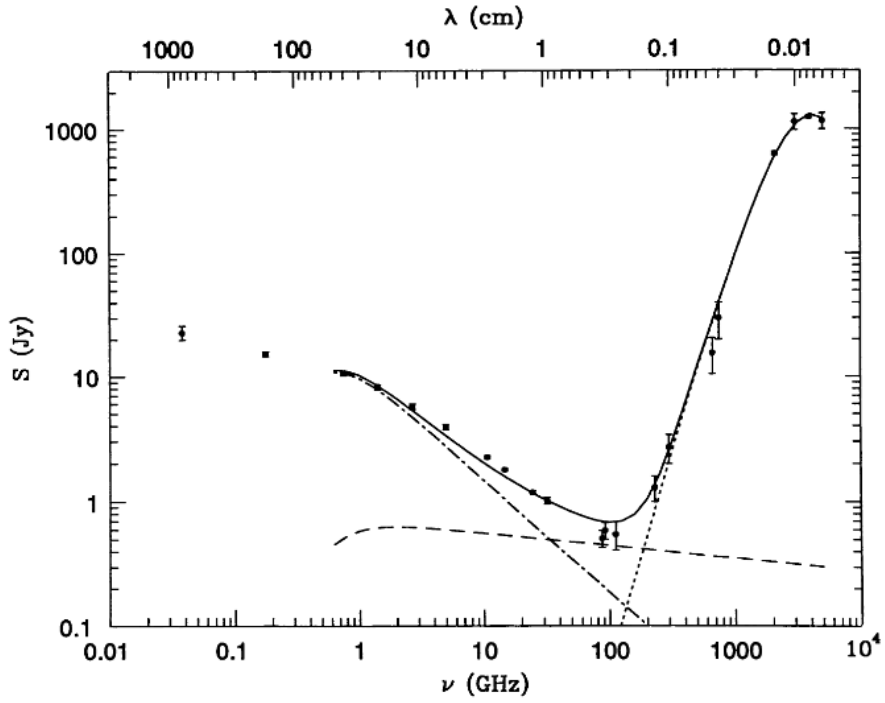

Figure 1.5: The spectral energy distribution of the star-bursting radio galaxy M82 (solid black line) broken down into the contributions of each emission mechanism; synchrotron (dot dashed), free-free emission (dashed) and thermal (dotted). Image credit - Condon (1992)

interacting with strong magnetic fields. Because of this, in the absence of AGN activity, the 1.4 GHz flux is a tracer for star-formation. As an increase in the star-formation rate of a galaxy will naturally result in a greater number of Supernova (SN) and Supernova Remnants (SNR) and hence a higher 1.4 GHz luminosity.

Moving to higher frequencies (rightward in Figure 1.5) we begin to approach the far-infrared regime, here the intense UV radiation from massive stars heat any surrounding gas and dust. As the surrounding gas warms, this energy is then re-emitted in the form of a black body spectrum in the FIR. As such this FIR emission is also tightly linked to the life-cycle of massive stars and hence provides yet another method by which to trace the star-formation rate.

Regardless of these expected proportionalities, given the large number of processes separating the synchrotron emission from supernova shocks and thermal emission from gas heated by young massive stars it is still somewhat surprising that a tight correlation is observed between the far-infrared flux (at 24, 70 or 160um) and the radio flux at 1.4 GHz. Known as the far-infrared radio correlation (van der Kruit, 1973; Condon, 1992) this tight relation spans several orders of magnitude and galaxy types (Helou et al., 1985) and seems to be consistent across a broad redshift range (Mao et al., 2012). Importantly this relation is used to define a broad number of astronomical objects and tools, from the identification of star-forming or AGN driven radio objects to the radio-luminosity to star-formation conversion used in the analysis of many separate studies (Bell, 2003), and it is a vital yet still poorly understood part of observational radio astronomy (Lacki et al., 2010).

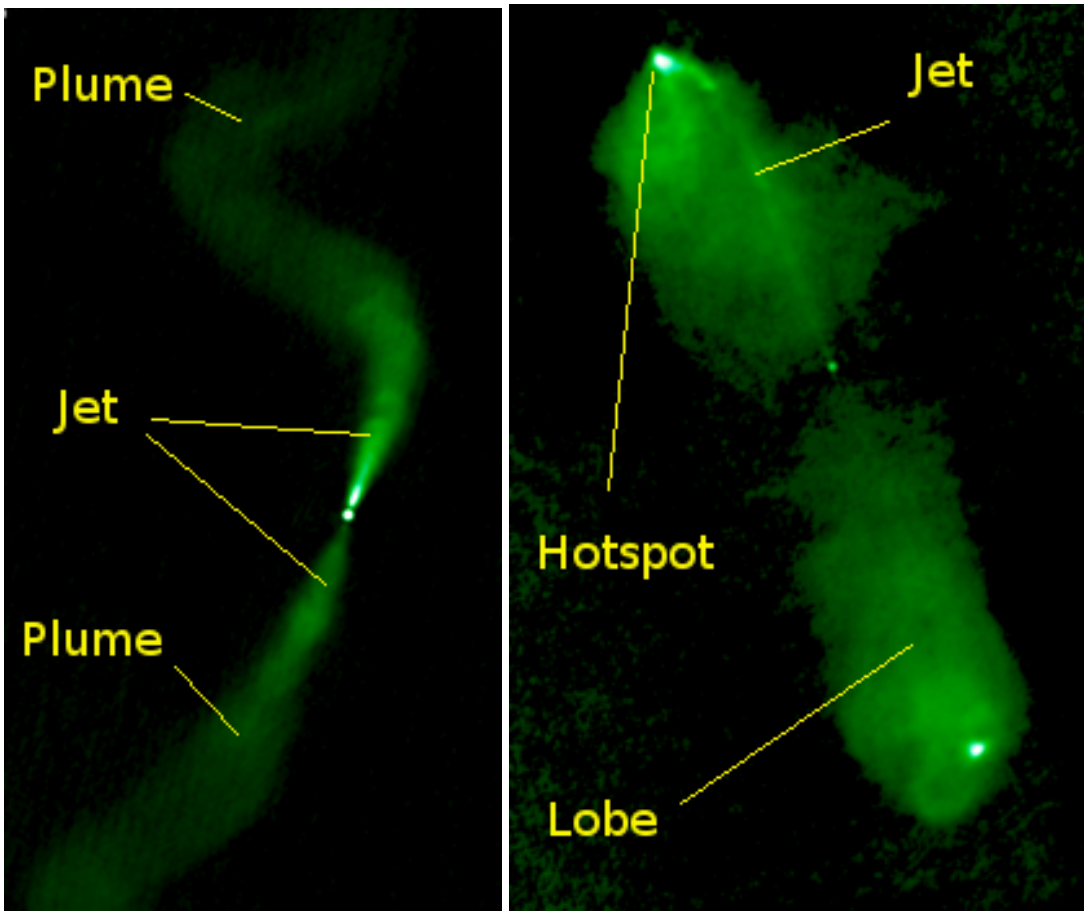

Figure 1.6: Examples of Fanaroff-Riley radio galaxies: Left: A FRI type radio galaxy characterised by the central bright core with plume like lobes of synchrotron emitting electrons. Right: A FRII type radio galaxy, characterised by its dim core with tightly collimated jets ending in bright hotspots. Credit - Rafter et al. (2011)

1.3.2 Synchrotron Emission from Radio-Loud AGN

The term Active Galactic Nuclei (AGN) refers to the emissions of actively acreting supermassive black holes at the center of a galaxy. AGN are thought to be the cause of a wide range of emissions, from infrared and optical radiation caused by super heated dust and gas in the accretion disk, to powerful continuum radio emission from relativistic electrons passing through the intensely coiled magnetic fields created near a black-hole's event horizon.

While AGN can be identified at a range of wavelengths, only a small fraction ($\approx$ 10-20%) of them show strong emission at radio frequencies (Best et al., 2005). Because of this in radio surveys, objects are often classified as one of two primary types: 'radio-loud' are those with radio fluxes more than 10 times their optical (Kellermann et al., 1989) or more recently far infrared emissions; and the 'radio-quiet', those whose radio flux is consistent with their optical or far-infrared flux. Alternatively if insufficient optical or near-infrared data is available, it is possible to classify radio galaxies based on their 1.4 GHz luminosity alone. Sources with a luminosity above 10^{25} WHz^{-1} can be considered radio-loud with those below 10^{24} WHz^{-1} limit being radio-quiet (Miller et al., 1990).

Radio-Loud AGN come in such a wide variety of sub-classes that a full categorisation of

them is beyond the scope of this thesis. However, the properties of certain classes of radio-loud AGN make them an important consideration in understanding the auto-correlation function at both large and small scales. As such we here provide a brief overview of a number of relevant radio-loud AGN classifications.

- Fanaroff - Riley Galaxies (FRI and FRII): Faranoff-Riley radio galaxies are divided into two distinct types: FRI and FRII based on their morphology at radio wavelengths. While both galaxies show a pair of lobe or plume like structures emanating from their host galaxy, Fanaroff-Riley I objects possess large, plume-like emissions with the highest luminosity regions centred around the galaxy core (Figure 1.6: Left). FRII objects on the other hand posses dim radio cores with bright hotspots at the end of highly collimated jets of relativistic electrons (Fanaroff & Riley, 1974). These hotspots are thought to be the result of the jets interacting suddenly with the intra-cluster medium, resulting in bow shocks which produce much stronger synchrotron emission (Figure 1.6: Right). It is this characteristic double-lobed radio morphology of these luminous radio sources that results in the highly elevated auto-correlation function at scales less than 0.1 degrees for bright sources. As we decrease in flux the fraction of radio objects possessing this morphology drops and hence at lower flux limits we expect them to have progressively less impact on the correlation function.

- Head-Tail (HT) and Wide Angle Tail (WAT) Radio Galaxies: Both Head Tail (elongated radio sources with a optical or NIR galaxy at one end) and Wide Angle Tail (c-shaped) radio galaxies are thought to be caused by the relative motion of the host galaxy through a dense intra-cluster medium. Due to the high ram pressure in these systems the radio jets are pushed back from their normal perpendicular relationship with the host galaxy, leaving either a c-shaped or elongated tail of emission behind depending on the angle of viewing (Christiansen et al., 1977; Jones & McAdam, 1996; Banfield et al., 2016). The effects of these galaxies on the auto-correlation function will be similar to that of FRI and FRII galaxies, however the identification of accurate host/core galaxy positions for HT and WAT sources is made all the more difficult by their unusual morphology, furthermore the non-symmetry of the sub-components in these sources will effect the correlation function at very small scales in a different way to the well modelled FRI and FRII type galaxies.

- Infrared Faint Radio Galaxies (IFRS): Infrared Faint Radio Sources (Norris et al., 2006; Middelberg et al., 2011; Collier et al., 2014; Herzog et al., 2015) are intensely bright in the radio regime but possess little, if any, optical or near infrared emission. They are thought to be high redshift radio-loud AGN but due to the lack of counterpart determining any kind of redshift information for these sources is problematic. They are a good example of the problems the radio astronomy community must address if we intend to perform precision cosmology studies, as without an accurate estimate of the redshift distribution of radio sources, we once again encounter the issues outlined in Section 1.1.3.

- Seyfert Galaxies: Seyfert galaxies are characterised by an AGN with extremely broad emission lines. These lines are thought to occur due to the high velocities of gas spiralling into a central black-hole. In addition to this Seyferts also display narrow emission lines which are believed to originate from the outer part of the AGN where

velocities are lower. The original classification of these objects was based upon the presence or lack of broad emission lines in the observational spectra. Type I Seyferts display both narrow (peculiar velocities ≈ 350 ms^{-1}) and broad emission lines (peculiar velocities ≈ 3000 ms^{-1}), whereas Type II display only the narrow spectral lines.

It has been suggested that AGN can be one of several modes: 'Cold Mode', where merger-driven accretion of a cold gas disc yields highly efficient accretion, is the highly energetic version and this process heats the surrounding gas resulting in feedback. Small weak winds formed near the accretion disk shock the in-falling cold gas, causing it to spread. This causes an increase in the surface area of the gas and thus increases the effects of ionisation and momentum-coupling from radiation. This then results in a greater radiation pressure acting on the surrounding gas slowing the accretion into the black-hole (Hopkins & Elvis, 2010). Once the radiation pressure reaches a critical level the efficiency of accretion (and thus AGN activity) drops as cold gas inflows decrease.

These lower energy forms are termed 'Hot mode' AGN and are characterised by much lower luminosities than their cold mode cousins. In summary, efficient 'cold mode' accretion is the dominant source for new or merger driven black holes and is most active in the redshift range of 2 to 4. Inefficient 'hot mode' accretion grows in overall importance until z = 0 and is responsible for the feedback which shuts off the cooling inflows of gas.

1.3.3 Synchrotron Emission from Radio-Quiet AGN

The final type of radio object discussed here is emission from radio-quiet AGN. While radio-loud AGN reach luminosities well above what can be feasibly generated by supernova shocks and free-free emission in HII regions, the exact process behind the radio emission in radio-quiet AGN is still a topic of some debate. In 1994 it was suggested that these objects may possess a central compact engine, similar to their radio-loud cousins (Kellermann, 1994) and that these compact engines may exist at luminosities spanning from Galactic center levels ($L_{1.4} = 10^{18}$ WHz^{-1}) through the radio-quiet regime ($L_{1.4} = 10^{22-24}$ WHz^{-1}) up to some of the most luminous radio objects in the Universe ($L_{1.4} = 10^{26-29}$ WHz^{-1}). This suggestion is supported by the detection of several compact cores in radio-quiet quasars in the Bright Quasar Survey and more recently by Very Long Baseline Array observations (Ulvestad et al., 2005) which have found several compact radio detections in radio-quiet AGN cores.

More recently however (Kimball et al., 2011) found that for a nearly complete sample of optically selected AGN with radio emission, an excess is seen in the number of radio-quiet quasars at radio luminosities corresponding to the upper limit of what star-formation driven emission can produce. They propose that a fraction of radio-quiet sources are purely driven by star-formation and that emission from the radio-quiet AGN population in general is simply a combination of star-formation and the lower limit of the radio-loud AGN powered emission.

1.3.4 AGN Unification Theory

Under the Unification Theory it is believed that most AGN powered objects are of similar structure and that the observed differences are primarily due to a combination of orientation

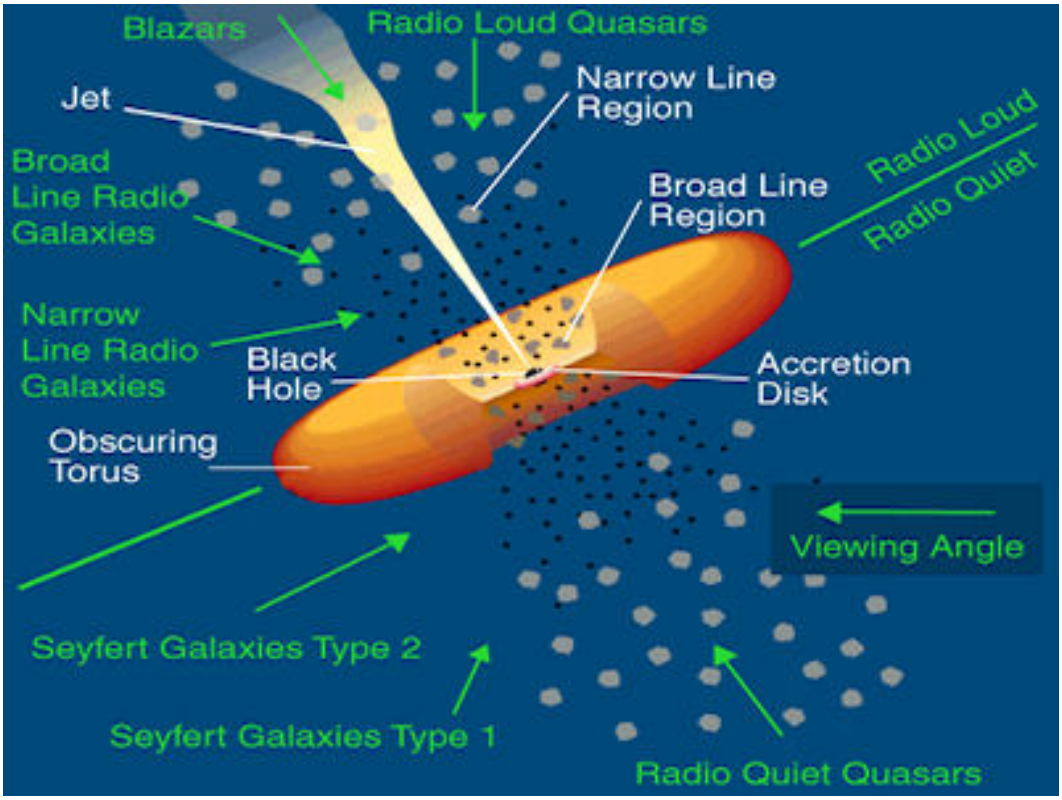

Figure 1.7: AGN Orientation and Obscuration Diagram, the relationship between various AGN classes may be explainable in terms of orientation and obscuration effect due to our line of sight. Image credit: Pierre Auger Observatory.

and dust obscuration. (Urry & Padovani, 1995). For example in AGN showing little to no broad spectral line emission it is thought that the central hot and rapidly rotating accretion region is obscured by dust and/or by our viewing angle on the galaxy. By combining AGN accretion modes, with orientation, black hole mass and spin, it is possible to produce a reasonable explanation of a wide variety of observed objects. Figure 1.7 shows a visualisation of the effects of unification theory. When first proposed unification theory was subject to several criticisms, firstly this theory does not adequately explain the strong UV/blue continuum emissions observed in most type 2 Seyfert galaxies. Secondly orientation effects fail to explain how some Seyfert galaxies have been known to swap types and finally based on orientation and obscuration alone it does not explain the differences between Radio Loud and Quiet types.

Later unification theory received a substantial boost by the inclusion of relativistic beaming, energetic gas and AGN accretion types. Seyferts could in theory swap from one type to the other due to the motion of the obscuring dust clouds. The UV/blue continuum in Seyferts can be explained by the extremely energetic gas surrounding the black hole. Finally, the addition of relativistic beaming effects can help explain the massive intensity boost Blazars display and are now understood to be aberration and time dilation effects.

For cosmological purposes the majority of interesting science regarding these objects, i.e how they form, evolve and impact their surroundings, is largely irrelevant. What we need, is a model of the radio sky that accurately samples the major source types. Radio-quiet AGN by definition are indistinguishable from standard star-formation galaxies using just radio

and FIR observations and hence any simulation that successfully models both the radio-loud AGN and star-forming populations should not suffer from ignoring this final object type.

1.4 Thesis Outline

This thesis deals primarily with the practicalities of constraining cosmology using upcoming all sky radio observations, from determining the redshift distribution and empirical bias of radio galaxies in the μJy regime, to the analysis of new observations of moderately sized (50-100 square degree) fields. The focus is on determining the auto-correlation, cross correlation and angular power spectra of existing and new data sets as well as the production of empirical radio simulations containing the cosmological effects we hope to test. Below, we give a brief summary of each chapter.

Chapter 1 has introduced the motivation for this work. We have discuss previous results from all-sky or near all-sky radio surveys as well as predictions for the cosmological sensitivity of EMU. We have introduced the concept of the radial selection function which is made up of the redshift and bias distributions unique to the flux and frequency of the observations, an understanding of which is necessary in order to relate the underlying dark matter halos produced by cosmological simulations to the observable radio sky.

Chapter 2 reproduces our paper on the redshift and host properties of radio-AGN and radio detected star forming galaxies. Framed as part of the ongoing discussion on the effect of radio-AGN jets on star-formation in the host, we determine highly accurate photometric redshifts for 91% of the radio objects with the remaining 9% having no visible near infrared (K_s-band) counterparts at the 25 magnitude level. Using this sample we study the redshift distribution of the radio sky, determine the radio-loud AGN fraction as a function of stellar-mass and redshift and find that the radio-AGN population is largely independent of host galaxy type across a broad redshift range.

Chapter 3 reproduces our follow up paper on the stellar-mass and redshift distribution of radio-AGN this time re-selecting based on a stricter definition of radio-AGN as identified at VLBI level resolution. VLBI emission at the frequencies, luminosities and surface densities observable in this mode can currently only be explained by AGN activity. We find no change in the relationships found in Chapter 2 and hence conclude that VLBI sources are not significantly different to radio-loud AGN and that our radio-AGN fractions determined in Chapter 2 are not significantly impacted by poor radio-AGN selection criteria. Importantly a number of our VLBI selected sources are radio-quiet (i.e. their radio continuum emission is still broadly consistent with their star-formation rate) and hence would be included in our later simulations as simply star-forming galaxies.

Chapter 4 summarises our attempt to produce a large scale radio cosmology simulation using the Theoretical Astrophysical Observatory. The type of numerical simulations usually used for predicting cosmological observables, like the angular correlation function, cannot by nature reproduce the effects of observational artefacts. Here we outline a process for converting semi-analytical simulations (in this case the Millennium simulation) into a simulated radio sky. This simulated sky still contains the underlying cosmological effects, while allowing for the introduction of real observable issues to the model. We take the underlying

Dark Matter halos produced by the Millennium simulation in a 10 by 10 degree field of view and populate them with galaxies using the Semi Analytical Galaxy Evolution code (SAGE). However SAGE does not operate in the radio-regime and hence does not identify radio-loud AGN or, for that matter, radio detected star-formers. To address this we develop a process to convert the SAGE galaxy catalogues to the radio regime, using the empirical AGN relations found in Chapters 2 and 3, along with known relations linking SFR to radio flux, to produce a semi-empirical radio sky which can then be limited in flux to match any survey limit down to 50μJy. We then produce the auto-correlation of this simulation at 300μJy and compare them to past and new observations. We also outline the approach used in modelling cosmological observables to be fit to our latest and upcoming observations. Taking a more traditional approach than the new simulations, we produce the spatial power spectrum of the expected dark matter halos, for a given cosmology, using the Cosmic Anisotropy Microwave Background code (CAMB). We then compress these observations into 2D and sample them via theoretical redshift and bias distributions before converting the resultant angular power spectra into auto and cross correlation functions.

Chapter 4 also details our analysis of the auto correlation function (and angular power spectrum where applicable) in three separate radio fields. Our primary data set is part of the Australian Telescope Compact Array Large Area Survey (ATLAS) and includes the newly completed 100 square degree observations South pole Telescope field (ATLAS-SPT). With a typical 1 sigma sensitivity of 100μJy ATLAS-SPT is $\approx$ 5 times deeper than the nominal NVSS sensitivity and given its incredible uniformity across the field, can be worked with at far lower signal to noise levels. We also analyse two 50 square degree fields of SDSS Stripe 82 imaged with the VLA, finding that significant source surface density variations (which these observations suffer from) can cripple cosmological analyses at these flux levels. Finally for testing of our methodology and in preparation for work at angular scales much larger than ATLAS-SPT (and with many more sources) we successfully reproduce the previous analyses of the NVSS data using both auto-correlation and angular power spectrum techniques.

Chapter 5 contains an outline of future and ongoing work to be completed in this vein of enquiry, from extending the current modelling techniques work to cover more of the potential cosmological probes discussed, to predictions and observations from the upcoming ASKAP-12 Early Science Cosmology Field, to the extension and improvements possible to our simulated radio sky. Finally Chapter 6 summarises the findings of each chapter in this thesis.

2

Radio galaxies in ZFOURGE/NMBS

Overview

Radio galaxies in ZFOURGE/NMBS: no difference in the properties of massive galaxies with and without radio-AGN out to z=2.25

G. A. Rees, L. R. Spitler, R. P. Norris, M. J. Cowley, C. Papovich, K. Glazebrook[6], R. F. Quadri, C. M. S. Straatman, R. Allen, G. G. Kacprzak, I. Labbe, T. Nanayakkara, A. R. Tomczak, K.-V. Tran

Monthly Notices of the Royal Astronomical Society, Volume 455, Issue 3, p.2731-2744, (2016)

This chapter is based upon Rees et al. (2016) and presents work cross-matching a sample of deep VLA observations at 1.4 GHz with high quality near-infrared observations from the ZFOURGE and NMBS surveys to better understand the type of objects observed at depths and frequencies similar to the EMU survey. Using this data we identify both radio-loud AGN and radio-detected star-forming galaxies and investigate their galaxy properties as a function of redshift and stellar-mass compared to a control sample of radio-non detected objects.

I was responsible for leading and writing the manuscript presented in the following chapter. I am responsible for the cross-identification of radio sources found within deep Very Large Array observations of the CDF-S and COSMOS fields with Ks-band observations of the ZFOURGE and NMBS surveys. I provided the analysis of these sources with respect to their stellar-mass and redshift similar counterparts as well as deriving 1.4 GHz luminosities, radio star-formation rates, and radio-AGN luminosities. I also provided these catalogues back to the ZFOURGE team with suitable flags for identifying radio-loud AGN. Furthermore as part of my work with the ZFOURGE team I was responsible for developing code to cross-check our observations (both photometry and astrometry for each of our bands) against several similar surveys.

L. R. Spitler and R. P. Norris supervised this work with respect to the methods used and scientific interpretation, as well as providing valuable and continuous feedback. C. M. S Straatman provided much of the primary data reduction and calibration. A. R. Tomczak

provided far-infrared star-formation rates based on 24, 70 and 160 μm observations. M. J Cowley, C. Papovich, K. Glazebrook, R. F Quadri, R. Allen, G. G. Kacprzak, I. Labbe, T. Nanayakkara and K-V.Tran provided feedback and guidance as well as numerous data products and checks inherent to all large surveys. Overall my contribution to the work presented in this Chapter is 90%.

2.1 Abstract

In order to reproduce the high-mass end of the galaxy stellar-mass-distribution, some process must be responsible for the suppression of star-formation in the most massive of galaxies. Commonly Active Galactic Nuclei (AGN) are invoked to fulfil this role, but the exact means by which they do so is still the topic of much debate, with studies finding evidence for both the suppression and enhancement of star-formation in AGN hosts. Using the ZFOURGE and NMBS galaxy surveys, we investigate the host galaxy properties of a stellar-mass limited ($M_{\odot} \geq 10^{10.5}$ $M_{\odot}$), high-luminosity ($L_{1.4} > 10^{24}$ W Hz^{-1}) sample of radio-loud Active Galactic Nuclei to a redshift of z = 2.25. In contrast to low redshift studies, which associate radio-AGN activity with quiescent hosts, we find that the majority of z > 1.5 radio-AGN are hosted by star-forming galaxies. Indeed, the stellar populations of radio-AGN are found to evolve with redshift in a manner that is consistent with the non-AGN stellar-mass similar galaxy population. Interestingly, we find the radio-AGN fraction is constant across a redshift range of $0.25 \leq z < 2.25$, perhaps indicating that the radio-AGN duty cycle has little dependence on redshift or galaxy type. We do however see a strong relation between the radio-AGN fraction and stellar-mass, with radio-AGN becoming rare below $\sim 10^{10.5}$ $M_{\odot}$ or a halo-mass of 10^{12} $M_{\odot}$. This halo-mass threshold is in good agreement with simulations that initiate radio-AGN feedback at this halo-mass limit. Despite this we find that radio-AGN host star-formation rates are consistent with the non-AGN stellar-mass similar galaxy sample, suggesting that while radio-AGN are in the right place to suppress star-formation in massive galaxies they are not necessarily responsible for doing so.

2.2 Introduction

Super-massive black-hole (SMBH) accretion is now considered to be one of the primary regulators of galaxy evolution. Because of this, understanding the ways in which this process can begin, along with the impact it has on the surrounding environment is one of the key questions in extra-galactic astronomy.

It has been suggested that actively accreting SMBHs in the center of galaxies, now commonly referred to as a Active Galactic Nuclei (AGN), can be triggered in a variety of ways. Merger driven models (Hopkins et al., 2008; Ramos Almeida et al., 2010; Karouzos et al., 2010; Sabater et al., 2013), induce accretion by both disrupting existing cold gas reservoirs in the merging galaxies and via the direct inflow of gas from the merger event itself. Alternatively, there is evidence to support the triggering of AGN in non-merging galaxies (Crenshaw et al. 2003, Schawinski et al. 2014, Draper & Ballantyne 2012 and references therein) via supernova winds, stellar bars and the efficient inflow of cold gas from the intergalactic medium.

At the same time, models have explored the various forms of feedback from AGN: pressure, mechanical energy and heating (McNamara et al., 2005; Nulsen & McNamara, 2013).

However, the exact impact of these different processes is still a topic of much debate, with observations supporting both the the suppression (Morganti et al., 2013; Nesvadba et al., 2010) and inducement (Bicknell et al., 2000; Silk & Nusser, 2010; Zinn et al., 2013; Karouzos et al., 2014) of star-formation by AGN activity.

Radio-AGN jets in particular are known to inject mechanical feedback that can heat gas and suppress star-formation. Given that radio-AGN tend to be found in massive galaxies (Auriemma et al., 1977; Dressel, 1981), it has been suggested that these processes may be responsible for the suppression of star-formation in high stellar-mass galaxies (Springel et al., 2005; Croton et al., 2006). Low redshift observations support this theory, finding that the majority of radio-AGN are located in high-mass quiescent galaxies (Best et al., 2005, 2007; Kauffmann et al., 2008). Higher redshift studies ($1 \leq z \leq 2$), which estimate redshift using the tight correlation observed between between K-band magnitude and redshift for radio-galaxies (Laing et al., 1983) agree with this, finding that radio-AGN hosts are consistent with passively evolving stellar populations formed at $z > 2.5$ (Lilly & Longair, 1984; Jarvis et al., 2001).

However, above $z \approx 2$, radio-AGN hosts begin to show magnitudes greater than we might expect from passive evolution alone, indicating that at these redshifts we may at last be probing the formation period of massive radio-detected galaxies (Eales et al., 1997). There is also growing observational evidence that star-formation may be common in high redshift radio-AGN hosts (Stevens et al., 2003; Rocca-Volmerange et al., 2013), and it has been suggested that we are witnessing these objects during the transition phase between the ignition of the radio-AGN and the quenching of star-formation by AGN feedback (Seymour et al., 2012; Mao et al., 2014a). Finally, observations at millimetre wavelengths support the existence large cold gas reservoirs in high-redshift, high-luminosity ($L_{1.4} > 10^{24}$ WHz^{-1}) radio-AGN hosts (Emonts et al., 2014), suggesting that at high redshifts the fuel for star-formation has not yet been removed by AGN feedback.

The suggestion that many high-redshift, high-luminosity radio-AGN are star-forming is interesting, as unlike their lower-luminosity Seyfert counterparts, these objects are rare at $z < 0.05$ (Ledlow et al., 2001; Keel et al., 2006; Mao et al., 2014b). One simple explanation for the apparent increase in actively star-forming radio-AGN hosts with redshift, is that high-redshift quiescent galaxies are simply more difficult to detect. This is particularly true in optically selected radio-AGN samples, as at $z \geq 1.6$ optical observations are probing the faint rest-frame UV part of the quiescent galaxy spectrum. Because of this, studies using samples of spectroscopically confirmed objects may be inherently biased towards star-forming objects.

This problem is much smaller for samples selected using detections in both radio and K-band, and the K-z relation allows for reasonably accurate redshift measurements out to $z \sim 2.5$. However, the relation is known to broaden significantly at high redshifts and lower radio fluxes (Eales et al., 1997; De Breuck et al., 2002), making the study of radio-AGN host properties difficult in these regimes as the accuracy of the objects redshift becomes increasingly uncertain.

Finally, and perhaps most importantly, radio-galaxies identified using either optical spectroscopy or the K-z relation typically lack a readily available control population free of radio-AGN to compare against. What is needed, is a rest-frame-optical (observed near-infrared) selected galaxy catalogue, supplemented with deep radio imaging and accurate redshift information in order to effectively study the effects of radio-AGN on their hosts at each epoc.

In this chapter, we present an analysis of two deep near-infrared (K-band) surveys combined with high-sensitivity 1.4 GHz radio observations. By selecting radio-loud AGN (radio-AGN hereafter) in this way, we are able to produce a stellar-mass and radio-luminosity complete sample of galaxies across a photometric redshift range of $0.25 < z < 2.25$, thereby minimizing our biases towards either star-forming or quiescent hosts. Furthermore, our observations include a large population of non-AGN galaxies at similar stellar-masses and redshifts to our radio-AGN sample, allowing us to directly compare star-formation rates between radio-AGN and non-AGN hosts in search of AGN feedback, while controlling for the effects of redshift and stellar-mass.

Section 2.3 of this paper describes our multi-wavelength data, as well as their unification into a single sample via cross-matching. Section 2.4.1 outlines our methods for classifying our sample into quiescent or star-forming hosts based on optical and Near-Infrared (NIR) stellar population emission and Section 2.4.2 covers our process for determining whether or not a galaxy is hosting a radio-AGN. The final sections contain our analysis (Section 2.5) and discussion (Section 2.6) of the resultant sub-samples.

2.3 Data

2.3.1 Near-Infrared observations

Our primary data are the pre-release K_s-selected galaxy catalogues from the FourStar Galaxy Evolution Survey (ZFOURGE, Spitler et al., 2012; Tilvi et al., 2013; Straatman et al., 2014, 2016). This survey covers the CDF-S (Chandra Deep Field South) and COSMOS (Cosmic Evolution Survey) fields (Giacconi et al., 2001; Schinnerer et al., 2004). Each $11' \times 11'$ field is imaged at a resolution of $0.6''$ down to a 80% K_s-band, point source magnitude limit of 24.53 and 24.74 AB mag for the CDF-S and COSMOS fields, respectively. This corresponds to a measured 0.6"-radius aperture limit of 24.80 and 25.16 AB mag (5 sigma) in each field (Papovich et al., 2014). The inclusion of five near-infrared medium band filters in J and H ($J1$, $J2$, $J3$, Hs and Hl) along with deep multi-wavelength data from surveys such as CANDELS (Grogin et al., 2011) allows the calculation of high-quality photometric redshifts using the photometric redshift code EAZY (Brammer et al., 2008) which uses a linear combination of 7 templates to produce the best fit SED. Additional 24μm observations from SPITZER:MIPS (Rieke et al., 2004) are used to calculate star-formation rates but are not used in the EAZY SED fitting process.

Due to the relatively small volume probed by ZFOURGE, we also make use of the less sensitive, larger area Newfirm Medium Band Survey (NMBS, Whitaker et al. 2011) to increase the number of galaxies detected. NMBS covers an area of $27.6' \times 27.6'$ in the COSMOS field and has significant overlap with the ZFOURGE COSMOS observations. While less sensitive in the K_s–selection band, NMBS still achieves a 5-sigma total magnitude of 23.5 in K–band and utilises up to 37 filters to produce accurate photometric redshifts (~1%,

Figure 2.1: Left) for approximately 13,000 galaxies.

Overall, ZFOURGE and NMBS produce redshifts with errors of just 1%-2% (Normalised Median Absolute Deviation) (Tomczak et al., 2014; Yuan et al., 2014; Whitaker et al., 2011) and are comparably accurate for radio-detected objects (Figure 2.1: Left). However, radio-detected objects show a higher catastrophic failure rate, which may be due to significant contamination of the stellar light by AGN emissions. Indeed, for the 6 radio-detected photometric redshift outliers, 2 objects have the smooth powerlaw SED shape associated with optical-AGN, 1 shows strong variability in the near-infrared (indicating potential IR-AGN activity) and the remaining 3 have poorly fitted SEDs due to coverage issues in some bands. These objects are removed during our flagging stages.

The center panel of Figure 2.1 shows a photometric versus spectroscopic redshift analysis limited to only those objects with detections in both surveys. Here we can see good agreement and comparable accuracy between ZFOURGE and NMBS out to z $\sim$ 1.0. The absence of high redshift spectra means we cannot directly test the accuracy of our photometric redshifts at values much higher than z $\sim$ 1.0, but we draw attention to the fact that both ZFOURGE and NMBS are specifically designed to produce accurate redshifts in the 1.5 < z < 2.25 regime for galaxies with strong 4000Å/Balmer breaks. The majority of our z > 1.0 radio galaxies have red SEDs with strong breaks similar to those shown in Figure 2.2 and overall are well fitted by the stellar templates. Finally we note that the photometric redshifts from both surveys show good agreement with spectroscopic redshifts out to z $\sim$ 1.5 and with each other out to z $\sim$ 3 (Figure 2.1: Right).

2.3.2 1.4 GHz radio observations

Radio detections in the CDF-S field are determined from the images and catalogues of the Very Large Array (VLA) 1.4 GHz Survey of the Extended Chandra Deep Field South: Second Data Release (Miller et al., 2013). Covering an area approximately a third of a square degree with a average RMS of 7.4 μJy per beam, this survey covers the entirety of ZFOURGE K_s-band observations in the CDF-S and has an excellent angular resolution of 2.8″ by 1.6″.

Radio detections for the COSMOS field are taken from the 1.4 GHz VLA Cosmos Deep Project (Schinnerer et al., 2010) which has an RMS of 10 μJy per beam. The COSMOS Deep Project covers the entirety of the ZFOURGE and NMBS K_s/K-band observations with a angular resolution of 2.5 ″ × 2.5 ″.

2.3.3 Cross-matching radio and K-band catalogues.

To check the astrometry between radio and K_s images we cross-match our catalogues using a 5″ separation radius and calculate the average positional offset. The COSMOS & CDF-S ZFOURGE images are found to have systematic astrometric discrepancies of 0.15″ and 0.30″ respectively when compared to the 1.4 GHz observations. The NMBS data shows only a 0.08″ offset from the COSMOS 1.4 GHz field. We apply corrections for these offsets in all subsequent cross-matching.

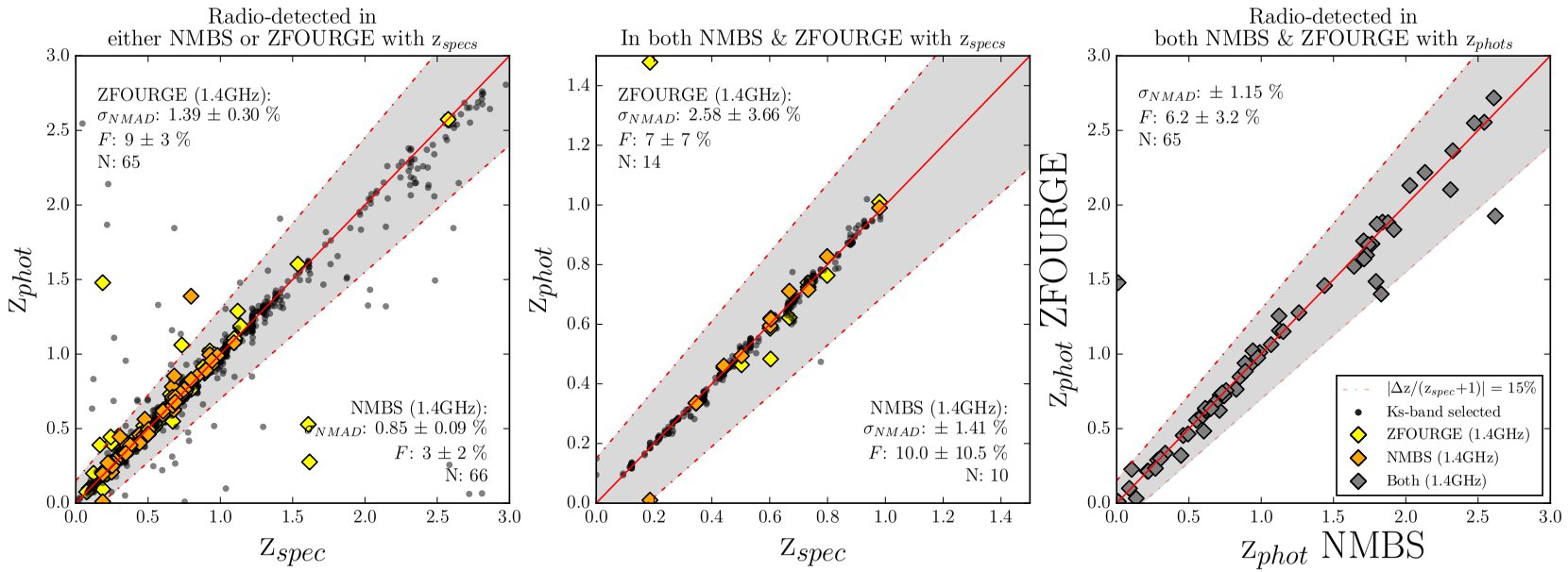

Figure 2.1: All: The Normalised Median Absolute Deviation of source redshifts (σ_{NMAD}), the catastrophic outlier fraction (F) where $\Delta z/(z_{spec}+1)$ <= 15% and the number of points included in the sample (N). Left: A photometric versus spectroscopic redshift comparison for radio-detected objects in either ZFOURGE (yellow diamonds) or NMBS (orange diamonds). K_s-selected objects with available spectroscopic redshifts from ZFOURGE are shown for reference (black circles). A 1:1 line is also plotted (solid red) along with the $\Delta z/(z_{spec}+1)$ <= 15% limits for reference (grey area). Center: A photometric versus spectroscopic redshift comparison for radio-objects detected in both ZFOURGE and NMBS. Right: A photometric versus photometric redshift comparison for radio-objects detected in both ZFOURGE and NMBS (grey diamonds). While ZFOURGE in general suffers a slightly higher outlier fraction than NMBS in the leftmost panel this is largely due to a small population of poorly fitted faint sources that are undetected in NMBS. These sources are flagged and are not included in our analysis.

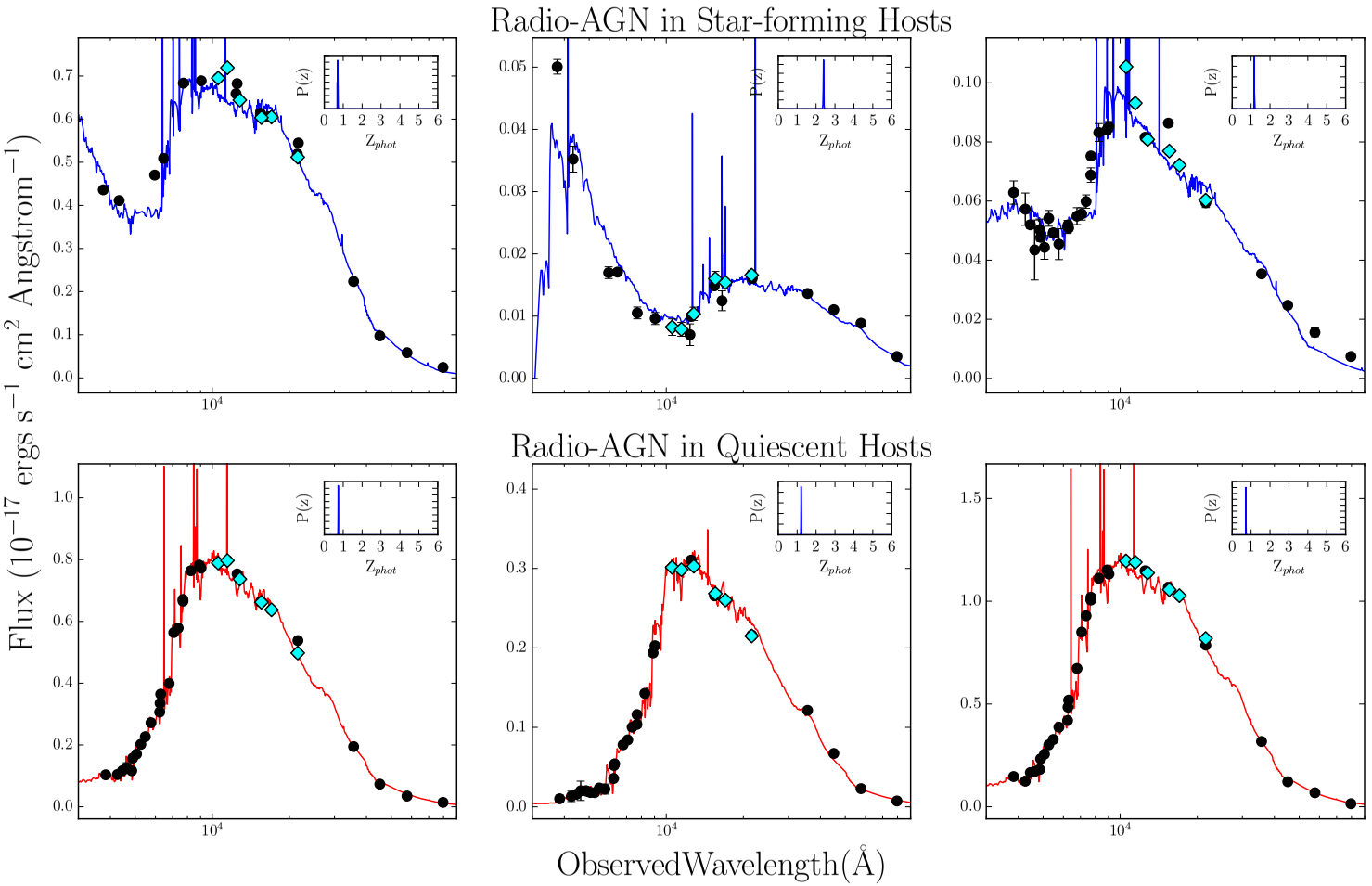

Figure 2.2: Example SED fits for two of our radio-detected populations: radio-AGN with quiescent hosts and radio-AGN with star-forming hosts (defined below). Photometric data points from ZFOURGE are shown (light blue) along with additional photometric data from other surveys used in the fitting process (black), error bars are show. The best fit EAZY SEDs are shown, colour-coded by their UVJ colour-code classification: quiescent (red) or star-forming (blue). On each panel a sub-plot displays the EAZY calculated probability distribution across redshift with narrow P(z) functions (in blue) indicating reliable photometric redshift fits. We can see that both types of radio-AGN hosts show good photometric fits and note that this is representative of the samples in general. SPITZER:MIPS 24μm fluxes were not used in the SED fitting process.

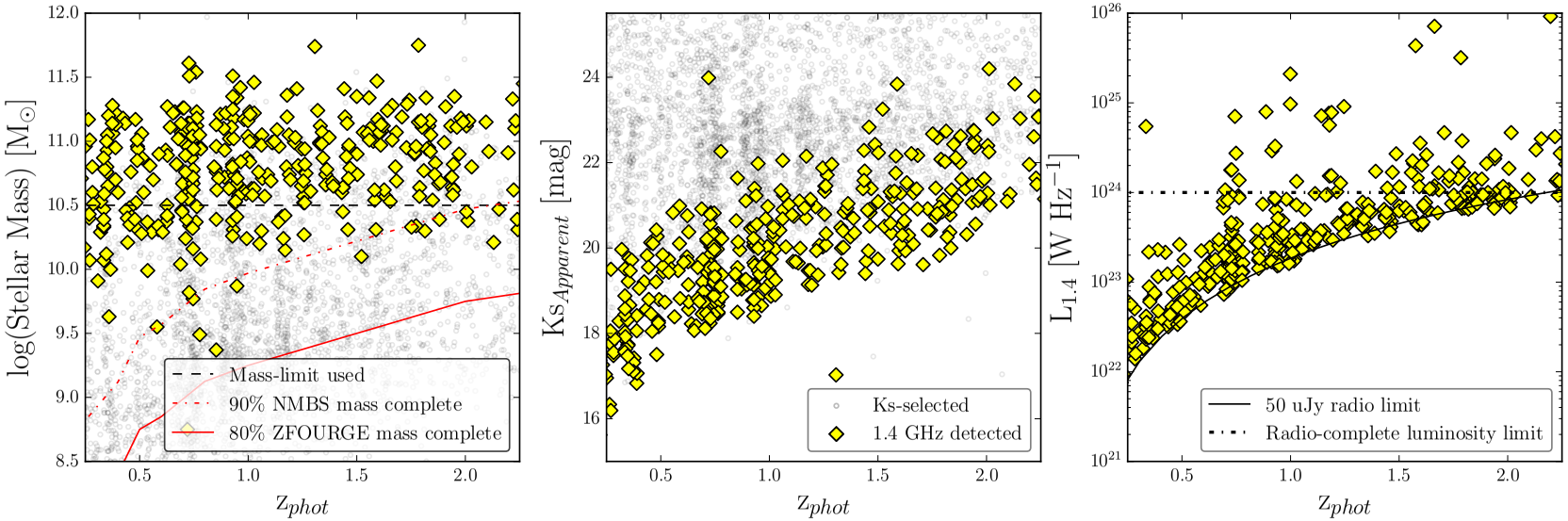

Figure 2.3: Stellar-mass, K_s magnitude and 1.4 GHz luminosities against z_{phot} for the combined ZFOURGE and NMBS fields. The entire K_s-band selected sample is shown (grey circles), alongside the 424 K_s-band objects with a 1.4 GHz counterpart within 1 $''$ (Yellow Diamonds). Left: The stellar-mass distribution of our galaxy sample shows a clear bias for radio detections to be found in massive galaxies. To account for this stellar-mass bias and to allow ready comparisons between radio detected and radio non-detected sources we define our stellar-mass limited sample as objects above $10^{10.5}$ $M_\odot$ (black dashes) and note that this is above both the 80% ZFOURGE stellar-mass-completeness limit (red line, Papovich et al. 2014) and the 90% NMBS stellar-mass completeness limit, which is the ZFOURGE 90% curve scaled to match the quoted z=2.20 (red dot dashed line, Wake et al. 2011) out to our redshift limit of z = 2.25. Centre: The K_s magnitude distribution as a function of redshift for 1.4 GHz radio detections. Right: 1.4 GHz luminosities as a function of redshift along with our luminosity completeness limit of 10^{24} W Hz^{-1} out to a redshift of z = 2.25. Note, for clarity only 10% of the radio non-detected sources are plotted.

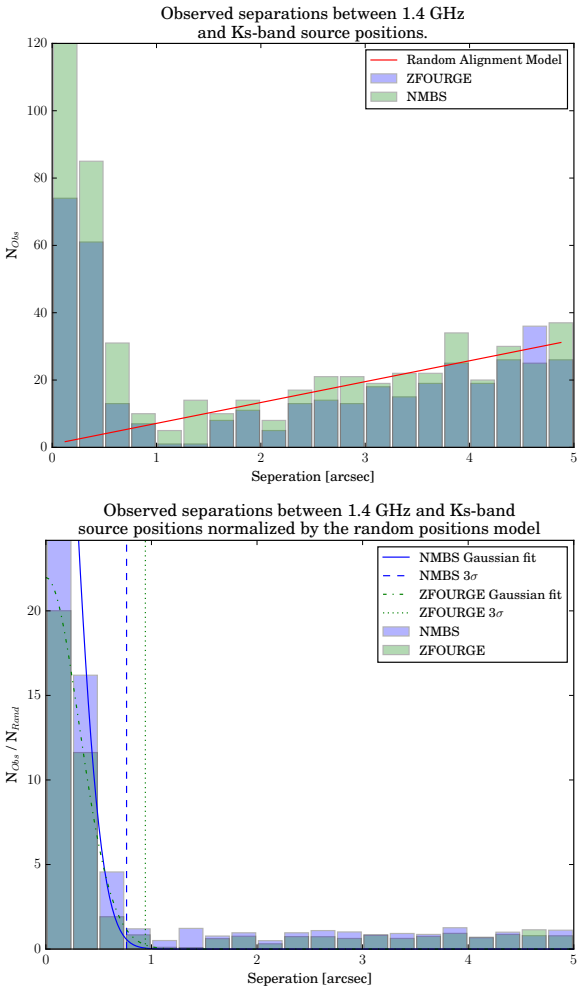

Figure 2.4: Top: Histogram detailing the number of radio to K_s-band pairs as a function of separation for the ZFOURGE (blue) and NMBS (green) surveys. The expectation for randomly positioned, point like sources shown (red line). Bottom: Same as above but normalised by the random expectation model. Gaussians are fitted to the residual ZFOURGE & NMBS populations and their three sigma limits are shown (dotted and dashed vertical lines). We use a 1″ cross-matching radius for both surveys.

We now determine the separation at which we will assume radio and K_s sources are associated by calculating the number of radio-K_s pairs as a function of angular separation (0″–5″) for both NMBS and ZFOURGE.

To remove the effects of chance alignments, we create a model of randomly positioned, point like sources and subtract this model from the observed distribution. The resultant distribution is largely Gaussian with 68% of radio-K_s pairs separated by less than 0.32″ (Figure 2.4) for ZFOURGE and 0.20″ for NMBS. Due to the quoted 0.3″ accuracy of the Miller et al. (2013) radio catalogues we therefore adopt a cross-matching radius of 1″ for all fields.

Using this limit we cross-match our radio catalogues against *Ks/K* band sources with ZFOURGE and NMBS use-flag of 1 which ensures that they have sufficient optical and IR imaging coverage, are far away from the scattered light of bright stars and are not stars themselves. We find 546 radio sources (ZFOURGE: 160 and NMBS: 386) have a K_s-detected

Table 2.1: Flagging breakdown, the number of sources remaining in the catalogues after applying each flagging stage.

Radio Sources	NMBS	ZFOURGE
With *Ks-counterpart*	388 (91+-2%)	162 (89+-2%)
Post $F_{1.4} < 50\mu$Jy flag	381	115
Post duplicate flag	317	115
Post SED flag	312	107

counterpart and note that our model for random alignments predicts that less than 14 of these are due to chance (ZFOURGE: 4 and NMBS: 10).

A visual inspection of the cross-matching shows that 2 objects in the COSMOS field seem to be missed in our automated procedure, despite being well aligned with the head of a head–tail radio galaxy and the core of a Faranoff-Riley Type I radio jet (Fanaroff & Riley, 1974). These objects were missed because our selected radio-catalogues quote the geometric center of large, extended objects. We manually add these matches to both the ZFOURGE and NMBS COSMOS sample bringing our total up to 550 (ZFOURGE: 162 and NMBS: 388) radio-K_s pairs. Thus we detect 550 radio-objects in the ZFOURGE and NMBS area, or approximately 91% (550/603) of radio objects that have good coverage in all bands and are not flagged as near stars. The remaining 9% of sources show no K_s-band counterpart within 1 arc-second and are potentially *K*-band drop-outs. We include a list of these objects in Appendix B.1.

We further flag our sample to ensure sensible handling of the overlapping NMBS and ZFOURGE fields, to minimize the difference in radio sensitivity between fields and to catch any poor SED fits missed by the automated procedure (Table 2.1).

To do this, we flag all objects with 1.4 GHz fluxes less than 50μJy in order to keep our radio sensitivity constant across all fields. This reduces our radio sample down to 496 objects (ZFOURGE: 115 and NMBS: 381).

Some NMBS and ZFOURGE sources are the same due to the overlapping observations. Inside the overlapping region between NMBS and ZFOURGE we preferentially use ZFOURGE data wherever possible as the greater signal to noise should result in more secure redshift fitting for dusty star-forming and quiescent objects (which dominate our sample) at redshifts greater than 1.5. If however, any radio-detection does not have a ZFOURGE counterpart, for example due to flagging or sensitivity issues, it will have been included in the analysis wherever possible via the NMBS observations. Outside the overlapping region we use NMBS exclusively. After duplicate flagging there remains 432 objects with reliable *Ks/K* and radio band detections shared between ZFOURGE and NMBS (Appendix B.2 and B.3). The *Ks/K*-band, radio luminosity and stellar-mass distributions of this sample are shown in Figure 2.3.

Finally we manually flag 13 objects due to poorly fit SEDs. Two of these objects objects are flagged due to saturated or missing coverage that is missed by the automated flagging due to the averaging of sensitivity coverage over 1.2 by 1.2 arc-second areas. Of the remaining 11 sources, 7 possess pure power-law SEDs whose redshift estimate cannot be trusted as there

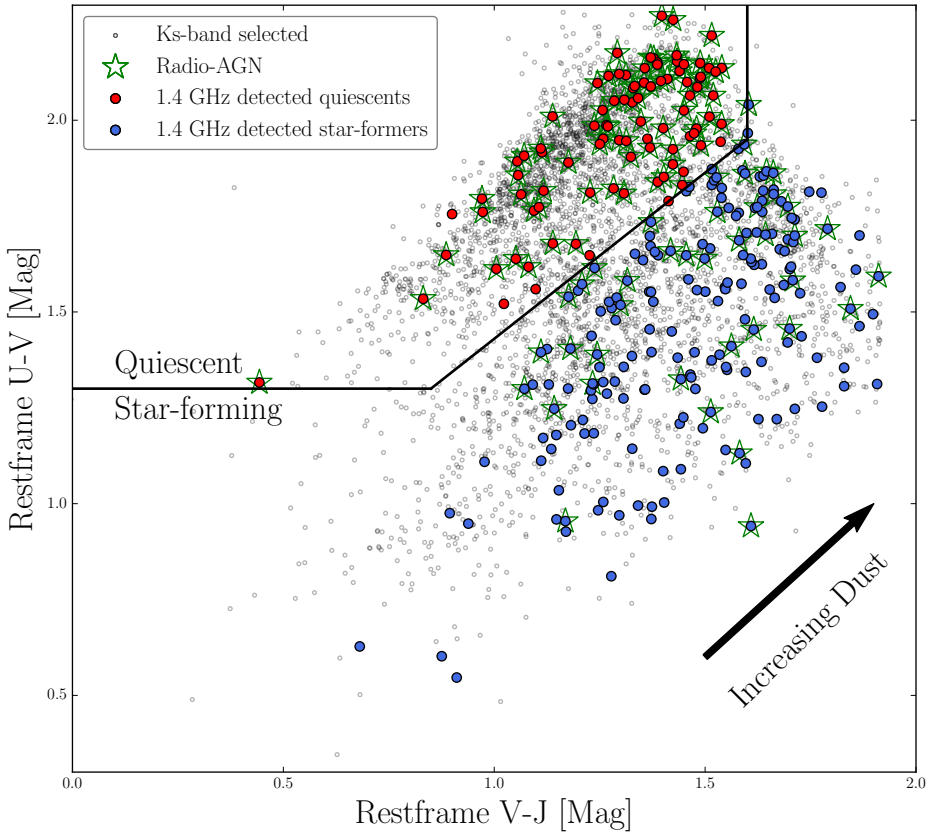

Figure 2.5: The rest-frame, UVJ colour-colour diagram for radio-detected star-formers (blue circles), radio-detected quiescent galaxies (red circles) and the ZFOURGE K_s-band stellar-mass limited sample (grey circles). Radio-AGN are selected based on their Radio to UV+24μm SFR ratios and are highlighted (green stars). For clarity only 10% of the radio non-detected sources are plotted.

is no break in the SED for EAZY to fit too and 4 SEDs showing large variability between observations in the NIR bands. Hence we have flagged 2.5% of our final radio sample due to poor SED fits.

2.4 Classifying radio galaxies

2.4.1 By Host Type

We determine the stellar population properties, including stellar-mass, dust-content, rest-frame colors and luminosities of our sample by fitting Bruzual & Charlot (2003) stellar population synthesis models with FAST (Kriek et al., 2009) using a Chabrier (2003) Initial Mass Function (IMF). Figure 2.2 shows example SEDs and fits. Finally galaxies were divided into two stellar population types: quiescent or star-forming, based upon their UVJ position (Wuyts et al., 2007), shown in Figure 2.5.

2.4.2 By Radio-AGN activity

A large number of techniques are currently used to identify radio-AGN (see Hao et al. 2014 for a review of 9 separate methods) but a key indicator is the ratio of 24μm to 1.4 GHz flux or the ratio of FIR (70μm-160μm) to 1.4 GHz flux. The resultant tight linear correlation shows no evolution out to a redshift of two (Mao et al., 2011) and is commonly known as the far-infrared radio correlation. Objects lying significantly off this correlation are typically classified as radio-AGN but the offset required for this depends on the AGN SED model and redshift.

It has been suggested that low redshift, radio-quiet AGN are dominated in radio wavelengths by host galaxy star-formation (Bonzini et al., 2013; Kimball et al., 2011) and composite sources in which AGN and star-formation both contribute to the radio emission are well–known (Emonts et al., 2008, 2014; Carilli & Walter, 2013). We therefore define a radio-AGN as an object in which the total radio flux is significantly greater than the radio emission expected from the star-formation rate determined at other wavelengths.

The baseline star-formation rate of each object in our sample is calculated using a combined optical and infrared technique (Kennicutt, 1998; Bell et al., 2005) and utilises the same IMF (Chabrier, 2003) as used in the galaxy stellar-mass fitting process.

$$SFR_{UV+FIR} = 1.09 \times (L_{IR} + 3.3 \times L_{2800})\ [M_{\odot}\mathrm{yr}^{-1}], \tag{2.1}$$

where L_{IR} is the bolometric rest-frame infrared luminosity between 8 and 1000μm. This is extrapolated from SPITZER:MIPS 24μm fluxes (Rieke et al., 2004) using the Wuyts et al. (2011) average stellar template. L_{2800} is the EAZY interpolated rest-frame 2800 Å (UV) luminosity.

This SFR allows for the accurate tracing of star-formation in a non-dusty host via UV emissions from hot young stars and complements this with the contribution from dust obscured stars using 24 μm observations.

Our radio star-formation rate estimate is just the linear, high luminosity portion of the Bell (2003) SFR estimate scaled to a Chabrier IMF (Karim et al., 2011) as all of our sources are above the given critical radio luminosity (6.4×10^{21}, W Hz^{-1}):

$$SFR_{Radio} = 3.18 \times 10^{-22} L_{1.4\,\mathrm{GHz}}\ [M_{\odot} yr^{-1}], \tag{2.2}$$

where $L_{1.4}$ is calculated using a radio spectral index α = -0.3 (where $S \propto \nu^{\alpha}$ in order to match the spectral index of the radio end of the Wuyts template used for calculating UV+IR SFR. Radio based star-formation rates are also largely unaffected by dust obscuration. Hence, they should accurately match the combined UV+IR based estimates within errors unless extra emissions from radio-AGN are present. he left panel of Figure 2.6 shows our method for identifying radio-AGN using their "Radio-AGN Activity Index":

Radio-AGN Activity Index =

$$SFR_{Radio}/SFR_{UV+IR} \tag{2.3}$$

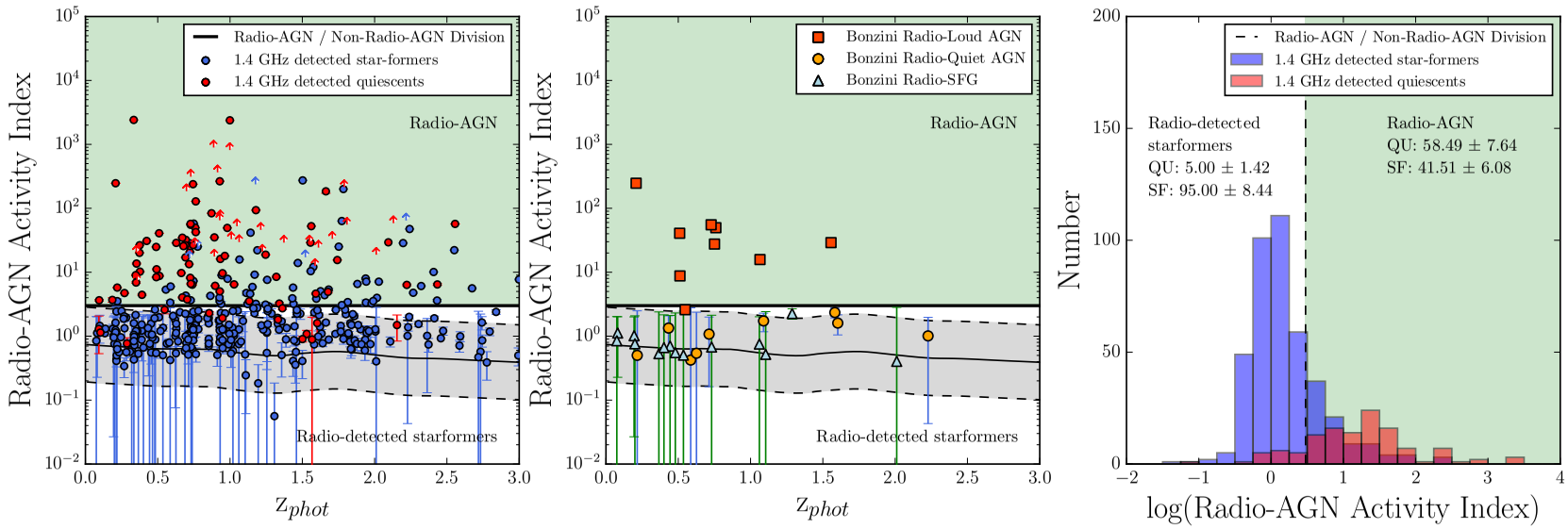

Figure 2.6: Left: the ratio of UV+IR to Radio SFR as a function of redshift, colour-coded by stellar population type. Objects with 24 μm fluxes less than the 24 μm sensitivity are shown as 3–sigma lower limits (arrows). The Wuyts et al. (2011) average star-forming galaxy SED template is shown (thin black line) along with the three sigma scatter seen the 1.4 GHz to 24μm flux ratios of local star-forming galaxies (grey shaded area). We determine that objects above the upper limit of this line (i.e $SFR_{1.4GHz}$ / SFR_{UV+IR} >= 3.0) are considered to be radio-AGN (green shading). Centre: A comparison of our classification of radio-AGN and non-radio-AGN sources to the Bonzini et al. (2013) classification scheme: Radio-Loud AGN (dark orange squares), Radio-Quiet AGN (light orange circles) and radio detected star-forming galaxies (light blue triangles). We see good agreement between Bonzini Radio-Loud AGN and our radio-AGN sample. Right: A breakdown of combined UV+24μm to radio star-formation rate ratios as a function of quiescent (red) or star-forming (blue) host galaxies. The fraction of each host type for radio-AGN (green shaded) and radio detected star-formers (white shaded) is labelled.

We use the Wuyts et al. (2011) average star-forming template to predict the expected indexes of star-forming galaxies. The Wuyts template produces a nearly flat, ratio of SFRs which is only slightly dependent upon redshift, hence we approximate the dividing line between star-formation driven radio emission and AGN driven radio emission as the three times the scatter seen in local 1.4 GHz to far-infrared flux ratios (0.39 dex, Morić et al. 2010). This divides our radio-detected sample into two: objects whose Radio-AGN Activity Index is less than 3.0 are henceforth classified as radio-detected star-formers and those whose radio-AGN activity index is greater than 3.0 are classified as radio-AGN. The center panel of Figure 2.6 compares our radio-AGN selection criteria to that of Bonzini et al. (2013). We see good agreement between our radio-AGN sample and their sample of radio-loud AGN. Finally we note that our results do not change significantly if our radio-AGN selection criteria is raised from a Radio-AGN Activity Index of 3.0, up to an Index of 5.0. The breakdown of quiescent and star-forming hosts as a function of our radio-AGN selection criteria is shown in the right panel of Figure 2.6.

While the combined UV+IR SFR should give a good estimate of total star-formation rate, independent of dust obscuration for the majority of sources, it does however, assume that the entirety of the observed 24μm flux is from star-formation and not contaminated by a hot, dusty AGN torus. To determine how much of an impact this issue will have on our analysis, we apply the Donley color wedge (Donley et al., 2012) to our final analysis sample to determine the the number of radio sources with infrared-AGN colours. We find that 10±2% (40/412) radio-detected objects in our sensitivity limited sample have IR-AGN colors and note that these objects may have artificially elevated SFRs.

But how does AGN contamination of the 24μm flux affect our analysis of SSFRs in radio-AGN and stellar-mass similar galaxies? Of the 40 IR-AGN identified, only 10 fall within our final stellar-mass and radio luminosity complete sample of 65 objects (15^{+5}_{-3}%) and only 4 of these are also classified as radio-AGN (of which there are 42). If we remove these objects from our radio-AGN analysis, along with every identified IR-AGN candidate from the stellar-mass and luminosity complete control sample of non-radio-AGN, we find no significant change in our findings.

Due to the presence of IR-AGN it is also possible that we misclassify a fraction of radio-AGN as radio-star-formers due to contamination of the 24μm flux. Any infrared flux from an AGN will artificially inflate the host galaxies SFR_{UV+IR} estimate, potentially keeping it below the division in the left panel of Figure 2.6. Because of this, it is possible that with better FIR observations some sources may move upwards from their current positions in this figure and become re-classified as radio-AGN. To quantify how common these objects are, we calculate the number of IR-AGN in the stellar-mass and radio luminosity complete sample that are not currently classified as radio-AGN. It is possible that these 6 objects should be included in our radio-AGN sample. Therefore, we estimate that our Radio-AGN sample is at worst 88^{+3}_{-6}% (42/(42+6)) complete due to this effect and note that the inclusion of these objects to our analysis makes no significant changes to our findings.

To account for these effects, the upper error bar on the quoted Radio-AGN fraction for the sensitivity limited sample given in Section 2.5.1 includes the value we attain should all 40 of the IR-AGN in the sensitivity limited sample currently identified as radio-detected star-formers were to move into our radio-AGN sample. The equivalent has been done for

our AGN fraction versus redshift analysis shown in Figure 2.12.

2.5 Analysis

2.5.1 The Radio sensitivity limited sky

The upcoming deep radio survey The Evolutionary Map of the Universe (EMU), will observe approximately 75% of the radio sky down to a limiting 5-sigma sensitivity of 50 μJy and produce a catalogue of approximately 70 million radio galaxies (Norris et al., 2011). To prepare for this large undertaking, we now characterise the radio-sky at a comparable sensitivity to EMU.

The majority of radio objects (76%) are found to have rest-frame UVJ colors associated with actively star-forming galaxies. The star-forming radio population shows a significant bias towards high dust content, with V-J values typically above the dusty, non-dusty border at V-J = 1.2 (Spitler et al., 2014).

Radio sources are found to have a median stellar-mass of $10^{10.8\pm0.5}$ $M_{\odot}$, a median redshift of z = 1.0±0.7, a median SSFR of 0.8±3.7 $M_{\odot}$ Gyr^{-1} and a median visual extinction of 1.4±0.9 mag. The errors quoted here are the standard deviations as we are characterising the populations rather than constraining the medians. We determine that only 38 $^{+6}_{-2}$% of radio sources (1-sigma BETA confidence interval error, (Cameron, 2013)) above 50 μJy are radio-AGN and this fraction shows no evolution within errors in the redshift range of 0.25 to 2.25. This confirms the result by Seymour et al. (2008) that the sub-mJy radio sky is dominated by emissions from star-formation.

2.5.2 The Stellar-mass limited and Stellar-mass similar, Radio-Complete sky

We now limit our sample in terms of stellar-mass, radio-luminosity and redshift to allow for a fair comparison between high stellar-mass radio galaxies and their non-radio counterparts using the following criteria:

1. $0.25 \leq z < 2.25$ to minimize the effects of our small survey volume and ensure completeness in both radio-luminosity and stellar-mass.

2. Radio luminosities must be greater than 10^{24} WHz^{-1} at 1.4 GHz observed. Objects above this limit are referred to hereafter as high-luminosity sources and objects below this limit as low-luminosity sources.

In addition we produce two slightly different control samples:

1. The “stellar-mass similar” population is used for comparing the properties of our test groups (both radio-AGN and radio-detected star-forming galaxies) to a control sample comprised of galaxies with similar redshifts and stellar-mass. In each case we determine the number of objects within our test population and randomly select the same

Property	Radio-detected	Stellar-mass Similar	KS P-Value
log(Stellar-mass) [$M_\odot$]	11.03 ± 0.06	11.00 ± 0.02	P = 0.98
Redshift	1.68 ± 0.06	1.54 ± 0.16	P = 0.10
SSFR [$M_\odot$ Gyr^{-1}]	3.92 ± 0.59	0.78 ± 0.21	P = 0.00
Visual Extinction [Mags]	1.60 ± 0.14	1.40 ± 0.19	P = 0.36

Table 2.2: Median properties for the 23 "radio-detected star-former" galaxies (Median $L_{1.4GHz} = 1.34 \times 10^{24}$ W Hz^{-1}) in ZFOURGE and NMBS, compared against the stellar-mass similar, redshift binned radio non-detected star-former sample.

Property	Radio-AGN (QU)	No Radio-AGN (QU)	KS P-Value
log(Stellar-mass) [$M_\odot$]	11.14 ± 0.06	11.12 ± 0.02	P = 0.98
Redshift	1.10 ± 0.13	0.99 ± 0.16	P = 0.56
SSFR [$M_\odot$ Gyr^{-1}]	0.08 ± 0.13	0.06 ± 0.02	P = 0.56
Visual Extinction [Mags]	0.55 ± 0.10	0.50 ± 0.09	P = 0.82

Table 2.3: Median properties for the 22 radio-AGN in quiescent hosts (Median $L_{1.4GHz} = 3.1 \times 10^{24}$ W Hz^{-1}) in ZFOURGE and NMBS, compared against the Stellar-mass similar, redshift binned, non-AGN quiescent population.

Property	Radio-AGN (SF)	No radio-AGN (SF)	KS P-Value
log(Stellar-mass) [$M_\odot$]	10.95 ± 0.09	10.92 ± 0.03	P = 0.97
Redshift	1.64 ± 0.12	1.55 ± 0.16	P = 0.50
SSFR [$M_\odot$ Gyr^{-1}]	1.41 ± 0.96	0.79 ± 0.25	P = 0.13
Visual Extinction [Mags]	1.45 ± 0.16	1.45 ± 0.21	P = 0.77

Table 2.4: Median properties for the 20 radio-AGN in star-forming hosts (Median $L_{1.4GHz} = 2.7 \times 10^{24}$ W Hz^{-1}) in ZFOURGE and NMBS, compared against the stellar-mass similar, redshift binned, non-AGN star-forming population.

number of K_s-detected galaxies from within each of our redshift bins (0.25-1.00, 1.00-1.65 and 1.65-2.25) whose stellar-masses are within 0.1 log($M_\odot$) of an object in the test group. We then measure and record the median value for each property of interest (e.g. SFR) for this stellar-mass similar control population and repeat the process 1000 times. The median value of all these measurements is then compared to the median of the test population (radio-AGN or radio-detected star-formers). Errors on all test population properties are standard errors and errors on the stellar-mass similar control samples are calculated using the normalised median absolute deviation of the 1000 random samples.

2. The "stellar-mass limited" population is simply all objects with stellar masses greater than $10^{10.5}$ $M_\odot$ (Figure 2.3: Left) and used solely for determining the fraction of galaxies containing a radio-AGN.

Both our stellar-mass similar and stellar-mass limited samples are above the stellar-mass completeness limit for the both the ZFOURGE (80% limit = 7.8×10^9 $M_\odot$, Papovich et al.

2014) and NMBS (90% limit = $3.0 \times 10^{10.0}$ $M_{\odot}$, Wake et al. 2011; Brammer et al. 2011) surveys at our maximum redshift of z = 2.25. Finally, all percentage and fraction errors in this paper are 1-sigma values calculated using the BETA confidence interval Cameron (2013).

Radio-detected star-formers galaxies

We now consider radio galaxies whose Radio-AGN Activity Index is less than 3.0 (i.e. objects whose radio emissions are consistent with what we would expect to detect based on their star-formation rate). In Figure 2.5 we see that these high-luminosity "radio-detected star-formers" are associated with star-forming rest-frame UVJ color (91^{+3}_{-10}%) and that the 9% of these objects found in the quiescent UVJ region are located very near the quiescent–star-forming boundary. Of these 2 objects, we find that 1 has an X-ray detection in public catalogues. In general these objects are thought to have simply scattered outside the UVJ star-forming region, but it is also possible that we are seeing the last effects of residual star-formation in a largely quiescent host.

As a whole, we find high-luminosity radio-detected star-forming galaxies to possess higher star-formation rates ($P < 0.01$) than their stellar-mass and redshift similar star-forming counterparts (Table 2.2) and we note that the low KS-test P-value for this property is likely due to the sensitivity bias of our radio observations towards high-luminosity (and hence high star-formation rate) sources.

Radio-AGN

While low-redshift radio-AGN are traditionally associated with massive, ellipticals (Lilly & Prestage, 1987; Owen & Laing, 1989; Vron-Cetty & Vron, 2001), our sample shows a variety of rest-frame colors, with only 48% ± 7% of high-luminosity radio-AGN found within quiescent galaxies. The remaining 52% ± 7% are hosted in star-formers with high dust-contents which is in good agreement with the growing number of CO detections found in high-z radio-galaxies (Emonts et al., 2008, 2014; Carilli & Walter, 2013).

Quiescent galaxy hosts with high-luminosity radio-AGN are found to possess star-formation rates and dust-contents indistinguishable from the stellar-mass similar quiescent population ($P = 0.56$ and 0.82 respectively, see Table 2.3). With Figure 2.7 showing no evidence to suggest either suppressed or enhanced star-formation in our redshift range of 0.25 and 2.25.

To determine the evolving stellar (and corresponding fixed halo) mass at which high-luminosity radio-AGN appear, we plot the masses of radio-AGN as a function of redshift (see Figure 2.8). Comparing these observations to a fixed halo-mass, which has been converted to stellar-mass using the Moster et al. (2010) stellar-to-halo mass relation (Moster EQ: 24), we determine the halo-mass that bounds the high-luminosity radio-AGN population to be 10^{12} $M_{\odot}$.

Of our high-luminosity radio-AGN, 20 are found to be embedded within star-forming hosts ("composites" hereafter). These sources contain large amounts of dust and would be easy to misclassify as quiescent without the use of our medium band near-infrared filters (*J1*, *J2*, *J3*, *Hs* and *Hl*). Comparing composites to the star-forming population we see in Figure

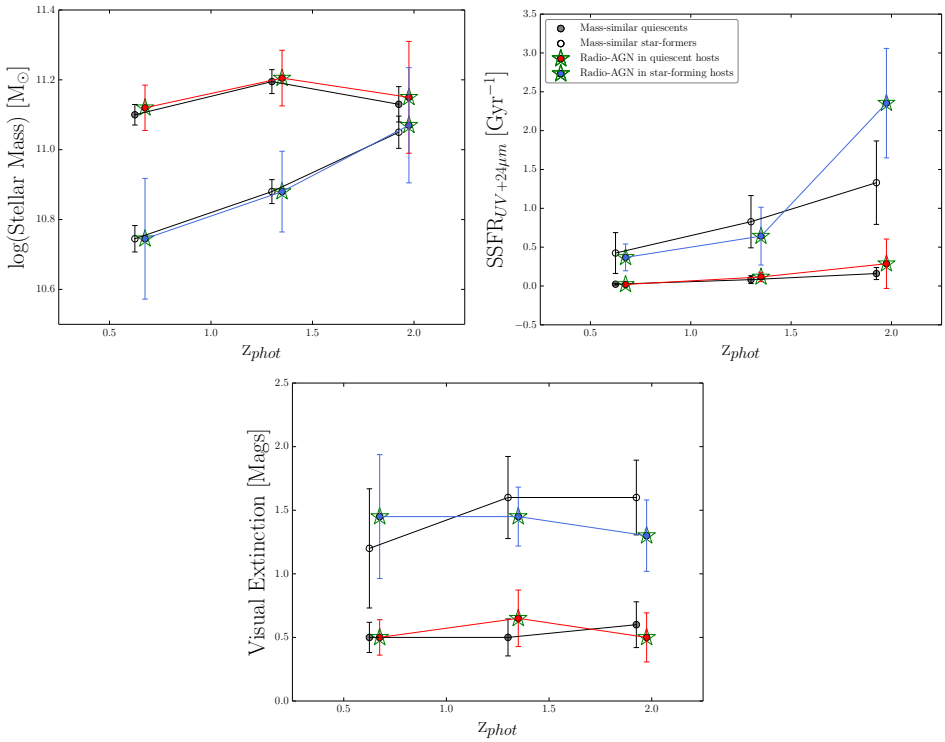

Figure 2.7: The measured median values for Stellar-mass (Top left), SSFR (Top right) and Visual Extinction (Bottom) for high-luminosity, quiescent and star-forming radio-AGN compared to their stellar-mass similar counterparts. We see no evidence for enhanced or suppressed star-formation in high-luminosity radio-AGN hosts within our redshift range. Errors are standard errors on the median and the normalised median absolute deviation, for radio-AGN and the stellar-mass similar sample respectively. Values are offset by 0.10 in the horizontal direction for clarity.

2.9 that a small number show extremely high SFR and SSFRs and are undoubtedly undergoing a star-burst phase. Despite this, Figure 2.7 shows that overall the SFRs and dust content of composite sources remain consistent with the stellar-mass similar star-forming population (P = 0.13 and 0.77 respectively). A visual inspection of Figure 2.11 shows that of the 8 composites covered by HST (CANDELS, Grogin et al. 2011), 7 have nearby companions and 3 show clear tidal interactions (objects 4, 5 and 8). However, these 3 sources do not correspond with any of the star-bursting objects visible in the bottom panel of Figure 2.9. Additionally, 4 composites are found to have strong X-ray counterparts with hardness ratios indicative of efficient accretion onto an AGN (Cowley et al, in prep) but also show no signs of elevated SSFRs. Finally, the high-luminosity composite population visible in ZFOURGE shows disk-like morphologies with a median Sersic index of 1.76 ± 0.18 (van der Wel et al., 2014).

Studying the evolution of high-luminosity radio-AGN as a whole, we can see that in terms of UVJ color, radio-AGN hosts evolve with redshift in a manner that is indistinguishable from their stellar-mass similar, non-radio-AGN counterparts (Figure 2.10).

The left panel of Figure 2.12, shows the fraction of galaxies containing a high-luminosity radio-AGN as a function of redshift. We find that across our full redshift range, an average

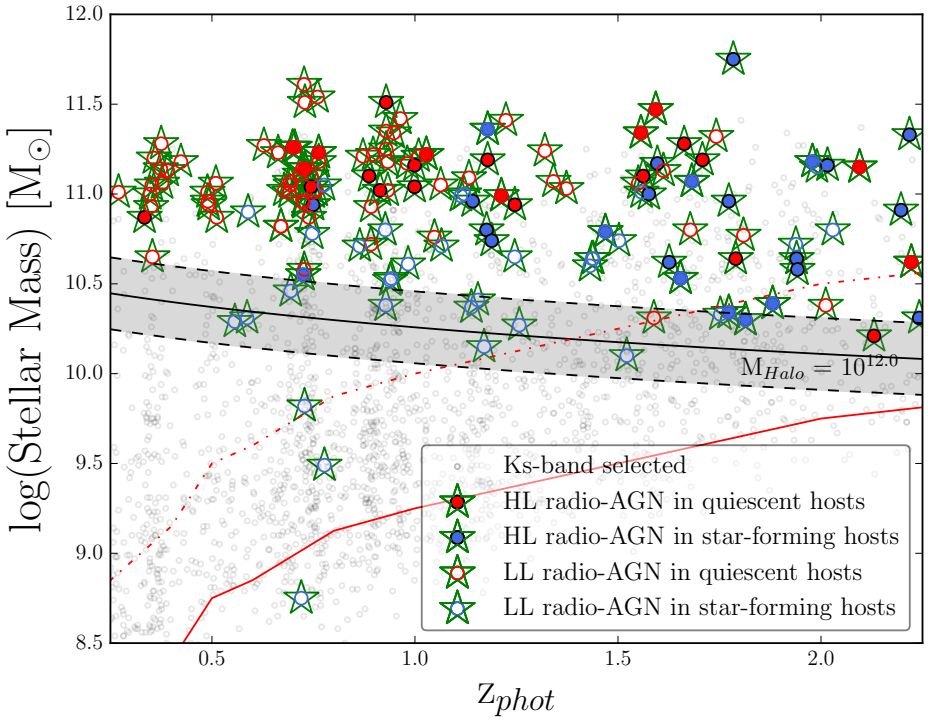

Figure 2.8: The stellar-masses of high ($L_{1.4} \geq 10^{24}$ W Hz) and low ($L_{1.4} \leq 10^{24}$ W Hz) luminosity radio-AGN. (filled and empty circles with green stars respectively). Quiescent and star-forming host types are also shown (red and blue circles respectively). The stellar-mass equivalent of a 10^{12} $M_{\odot}$ halo-mass (black line) along with the K_s-selected sample (grey circles) are plotted for reference, for clarity only 10% of the K_s-selected sample is plotted. Finally, the 80% ZFOURGE stellar-mass completeness limit is shown (red line, Papovich et al. 2014) along with the 90% NMBS stellar-mass completeness limit, extrapolated down from z=2.20 (red dot dashed line, Wake et al. 2011). Radio-AGN in quiescent hosts are only found in objects with halo masses above 10^{12} $M_{\odot}$ (black line), 100% of high-luminosity radio-AGN in our sample are found above this line. The 1-sigma local scatter in the stellar-to-halo mass relation is shown (grey shaded region). Finally we note that for this plot we do not limit our radio-AGN sample by mass in any way.

of $1.0^{+0.3}_{-0.2}$% of quiescent, $1.1^{+0.3}_{-0.2}$% of star-former and only $1.0^{+0.3}_{-0.1}$% of all massive galaxies ($M \geq 10^{10.5}$ $M_{\odot}$) host a high-luminosity radio-AGN, with little evolution in these values as a function of redshift. In the centre panel of Figure 2.12, we see a tight dependence between high-luminosity radio-AGN and stellar-mass, with a significant decrease in the abundance these objects from approximately 10% at $M_{\odot} \geq 10^{11.5}$ down to less than 1% at $M_{\odot} \geq 10^{10.5}$. We draw attention to the sharp drop-off seen in right panel of Figure 2.12 where the fraction of star-forming high-luminosity radio-AGN hosts declines rapidly below a redshift of z = 1.5. This is consistent with the declining percentage of high-mass galaxies that are star-forming in general, within our stellar-mass limited sample. This may explain the rarity of low redshift composites as simply due to the lack of suitable high-mass star-forming galaxies in the local universe. Finally, we note that in both the left and right panels of Figure 2.12, the star-forming and quiescent high-luminosity radio-AGN fractions follow the same trend within errors.

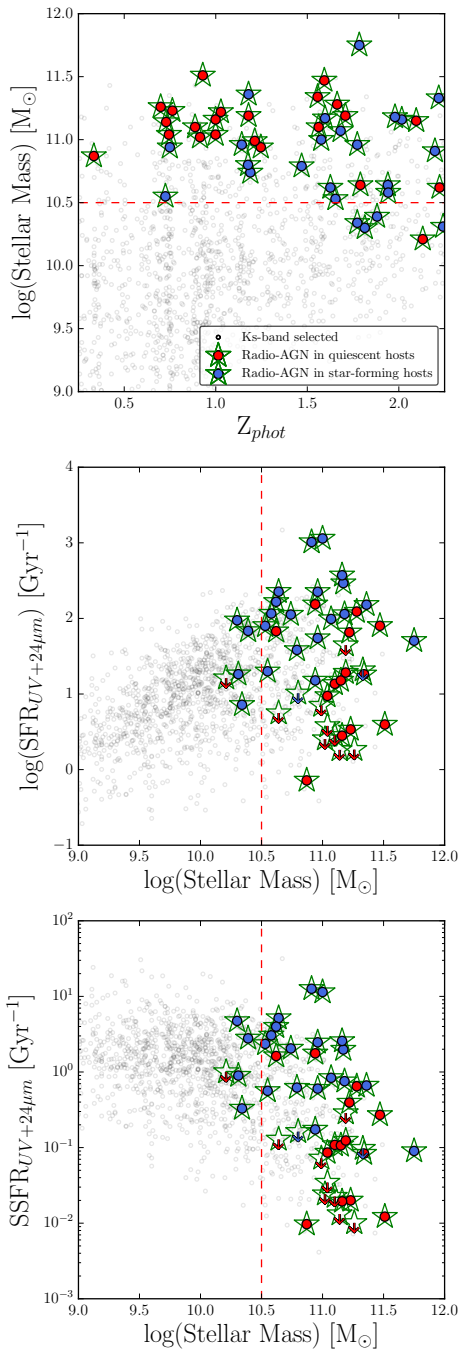

Figure 2.9: Top: The stellar-mass-redshift relation for high-luminosity radio-AGN in star-forming hosts (blue circles with green stars) and high luminosity radio-AGN in quiescent hosts (red circles with green stars). For reference, the K_s-selected, sample is also shown (grey circles) along with the stellar-mass limit used for our analysis of the various populations (red dashed line). For clarity only 10% of the K_s-selected sample is plotted. Middle: The stellar-mass versus SFR plot colour-coded as before. Bottom: The stellar-mass vs SSFR plot colour-coded as before .

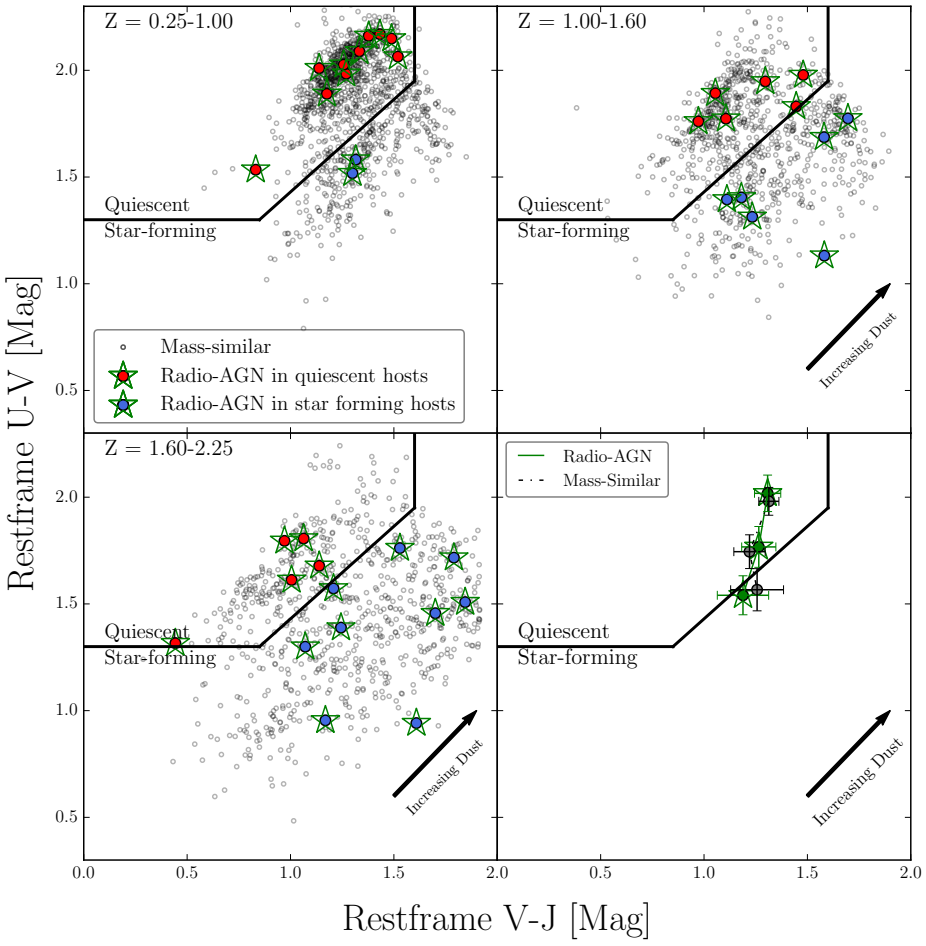

Figure 2.10: The UVJ diagram for high-luminosity radio-AGN compared to the stellar-mass similar sample in three redshift bins: 0.25-1.0 (top left), 1.0-1.60 (top right) and 1.60-2.25 (bottom left). Bottom right: The median position for radio-AGN and the randomly sampled stellar-mass similar population across the three redshift bins. Errors are standard error on the median and the Normalised median absolute deviation respectively. For clarity only 10% of the K_s-selected sample is plotted

2.6 Discussion

Using our high luminosity ($L_{1.4} > 10^{24}$ W Hz^{-1}) stellar-mass limited radio-AGN sample, we are able to study the fraction of massive galaxies that host radio-AGN to a redshift of z = 2.25. Figure 2.8 shows that high luminosity radio-AGN become rare beneath a stellar-mass limit of $\sim 10^{10.5}$ M$_\odot$ at low redshifts (z = 0.25). Interestingly this limit evolves with time, such that it mimics the expected evolution of the stellar-to-halo mass relation for a fixed halo-mass of 10^{12} M$_\odot$. The implication of this result is that there may be a link between galaxies with high-mass halos and the triggering of high-luminosity radio-AGN. Indeed, the apparent halo-mass limit for hosting radio-AGN is consistent with the critical halo-mass at which simulations typically have to invoke AGN feedback in order to reproduce the local galaxy mass function (Croton et al., 2006; Springel et al., 2005).

As seen in Figure 2.8, only a small number of high-luminosity radio-AGN fall below our 10^{12} M$_\odot$ halo-mass line (converted to stellar-mass using the Moster et al. (2010) stellar-to-halo mass relation). At z > 1 this may be partially due to the incompleteness of NMBS

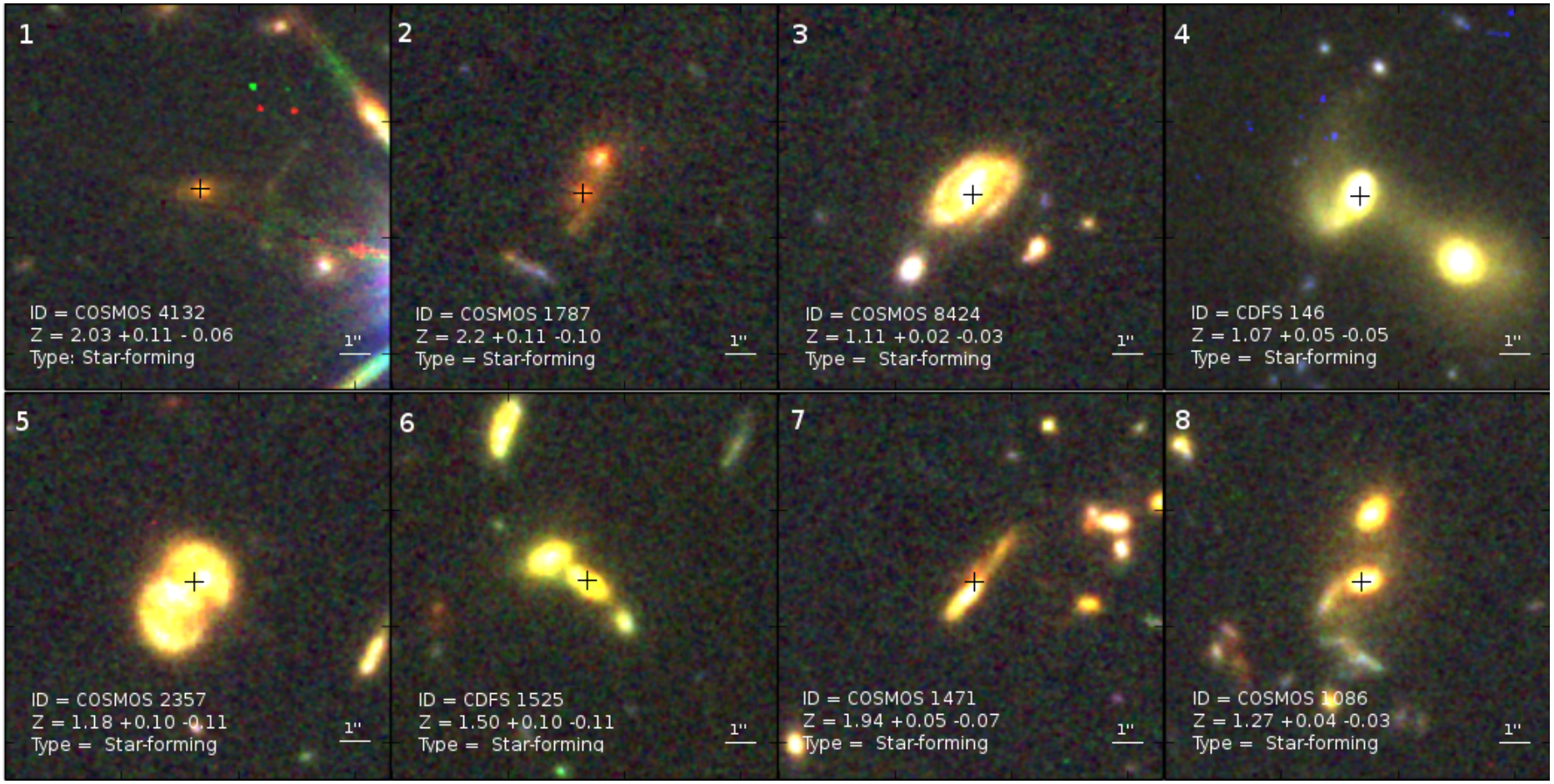

Figure 2.11: RGB thumbnails of composite sources using F125W, F160W and F814W filters, 3 sources show sure signs of merger activity (# 4,5 & 8), and 7/8 show nearby companions or distorted morphologies (with the exception of composite #1)

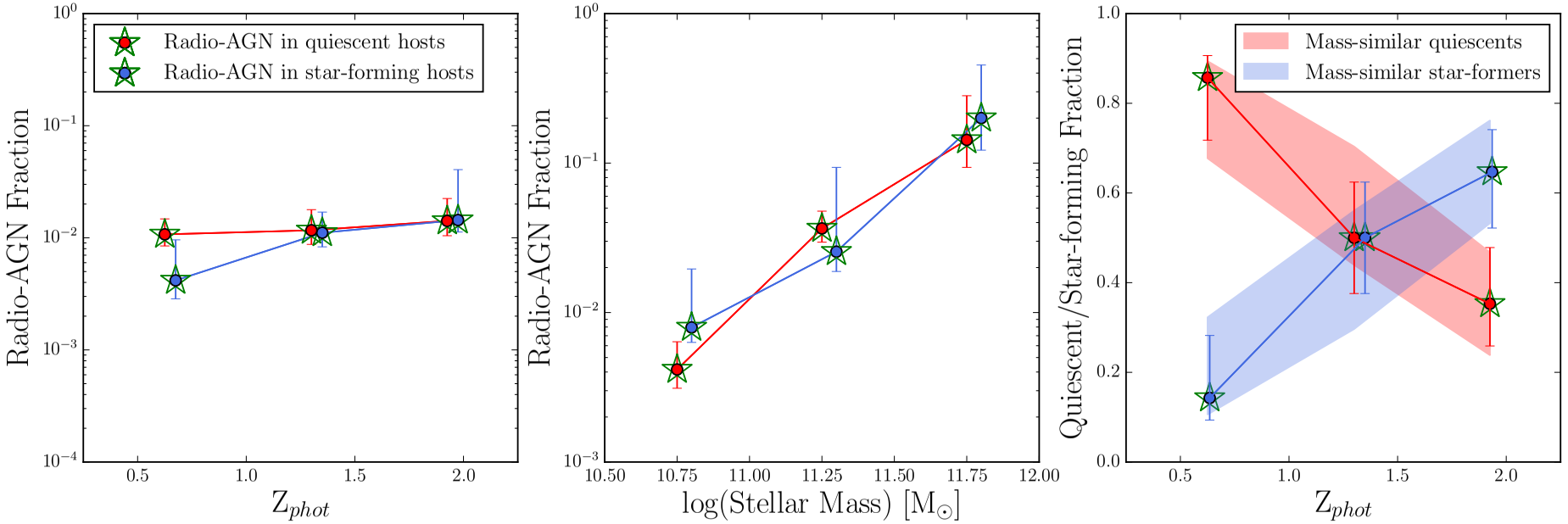

Figure 2.12: Left: The evolving radio-AGN fraction for quiescent (red with green stars) and star-forming (blue with green stars) high-luminosity radio-AGN above our stellar-mass limit of $10^{10.5}$ $M_\odot$. Center: The radio-AGN fraction for each host type as a function of stellar-mass shows a sharp drop-off in radio-AGN fraction as we progress to lower stellar-masses, in excellent agreement with Best et al. (2005). Left and Center panels show the number of quiescent or star-forming Radio-AGN hosts divided by the number of quiescent of star-forming galaxies in the given bin. Right: The breakdown of quiescent and star-forming high-luminosity radio-AGN hosts as a function of redshift. The fraction of quiescent (red shaded) and star-forming (blue shaded) galaxies of similar stellar-masses to the radio-AGN hosts is shown for comparison. All Errors are BETA confidence intervals and NMAD errors from 1000 random samples for the radio-AGN and stellar-mass similar samples respectively.

below $10^{10.5}$ $M_{\odot}$. However even at z < 1, where our completeness is well above 80% we see very few radio-AGN in low stellar-mass galaxies. Assuming that this halo-mass is required for powerful radio-AGN activity, the few objects that are found in lower stellar-mass galaxies may reflect scatter in the stellar-to-halo mass relation ($\simeq 0.2\pm$ dex at z = 0 More et al. 2009; Yang et al. 2009; Reddick et al. 2013; Behroozi et al. 2013). In addition to this, Kawinwanichakij et al. (2014) find that quiescent galaxies at high redshift have unusually large halo-masses for a given stellar-mass (by up to $\simeq 0.1-0.2$ dex), hence it is possible that some of our low stellar-mass radio-AGN hosts may actually reside in halos larger than the Moster et al median.

Alternatively, the observed halo-mass limit we discussed above may simply correspond to the stellar-mass where the high-luminosity radio-AGN fraction becomes negligible. The left nad center panels of Figure 2.12 shows the fraction of massive galaxies containing a high-luminosity radio-AGN as a function of redshift and stellar-mass. While we find little evolution in the high-luminosity radio-AGN fraction as a function of redshift, we do observe a strong correlation with stellar-mass in good agreement with previous results which indicate nearly 30 percent of the highest stellar-mass galaxies contain powerful radio-AGN (Fabbiano et al., 1989; Sadler et al., 1989; Brown et al., 2011). Figure 2.13 shows a comparison between the stellar-mass dependent radio-AGN fraction of our study to those of previous work in three redshift bins: 0.4 < z < 0.8, 0.8 < z < 1.2 (to match previous studies) and 1.2 < z < 2.25. Our high-luminosity radio-AGN fraction is slightly higher than that found in previous studies (0.03 < z < 0.1, Best et al. 2005 and 0.4 < z < 1.2, Simpson et al. 2013) and we speculate that this may be due to differences in the techniques used to identify our radio-AGN samples. Despite this offset, the lack of evolution between redshift bins in our study is consistent with the lack of evolution seen between redshifts in these previous investigations. This raises the question of whether the universal radio-AGN fraction is simply a function of stellar-mass, with the most massive galaxies being much more likely to host radio-AGN activity than low stellar-mass galaxies. In extremity, extrapolating upward in stellar-mass suggests that above stellar-masses of 10^{12} $M_{\odot}$, nearly all galaxies should contain a radio-AGN.

To investigate the impact of radio-AGN on host galaxy properties, we also use our stellar-mass similar sample to compare radio-AGN hosts to non-hosts. We find that the high number of close companions and mergers seen in our high-luminosity composite (radio-AGN in star-forming hosts) sample seems to support a merger driven AGN triggering model. Despite this, we see no evidence for the enhanced star-formation rates expected during merger scenarios (Table 2.4) as composite SFRs are indistinguishable from the stellar-mass similar star-forming sample. This may only reflect the short time-scales of a merger-induced starburst. Finally, the right panel of Figure 2.12 shows that the fraction of radio-AGN hosted within quiescent and star-forming hosts evolves in a similar fashion to the non-AGN galaxy population. These results suggest that the radio-AGN and non-radio-AGN populations are hosted by galaxies with similar properties.

2.7 Conclusions

We have combined a deep K_s-band selected sample, which is ideal for selecting galaxies across a wide redshift range (Rocca-Volmerange et al., 2013) with high quality photometric

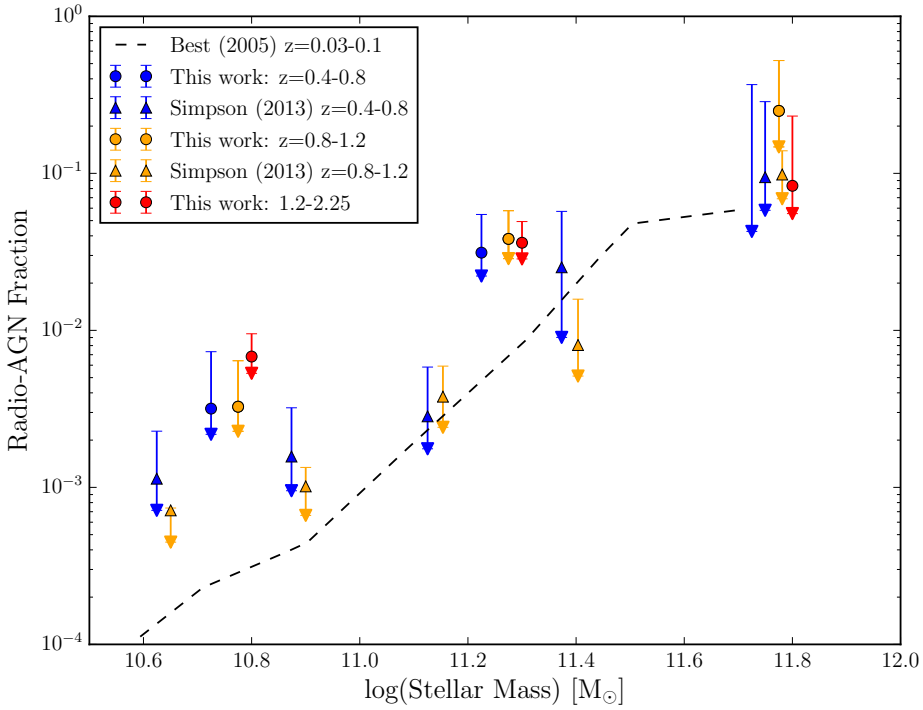

Figure 2.13: The fraction of galaxies containing radio-AGN with luminosities greater than 10^{24} W Hz as a function of stellar-mass for three redshift bins: $0.4 < z < 0.8$ (blue circles), $0.8 < z < 1.2$ (orange circles) and $1.2 < z < 2.25$ (red circles). We see no evolution between our redshift bins. This is in good agreement with previous studies by Best et al (2005) at $0.03 < z < 0.1$ (blue dashes) and Simpson et al (2013) at $0.4 < z < 0.8$ and $0.8 < z < 1.2$ (color coded as before). Our low stellar-mass radio-AGN fraction is elevated at all redshifts compared to previous studies, which may be due to differences in how we select our radio-AGN samples.

redshifts and sensitive 1.4 GHz VLA observations to identify 412 radio sources in the CDF-S and COSMOS legacy fields. This sample is split into two sub-groups: radio-AGN and radio detected star-forming galaxies using the ratio of the UV+24μm-based and radio-based star-formation rates. Using this sample we study the host properties of radio-AGN and compare them to a non-radio sample of similar stellar-masses and redshifts out to redshifts of 2.25. Due to a variety of issues arising from optical and IR based AGN, we note that our radio-AGN sample may be incomplete. Primarily this incompleteness stems from the flagging of pure powerlaw/variable SED fits for 2% of radio sources (which could add as much as 14% to the radio-AGN population) and a number of radio objects showing signs of IR-AGN activity, which may result in as much as 11% of the potential radio-AGN population to be misclassified as radio-detected star-formers. As such we estimate that our radio-AGN population is at least 75% complete and note that the inclusion of the IR-AGN contaminated and SED flagged population with their best fit properties make no significant changes to our results.

1. We find that the fraction of galaxies that contain radio-AGN at a given stellar-mass shows little dependence on redshift or star-formation activity. This is in good agreement with the findings of Best et al. (2005) and Simpson et al. (2013) and extends the analysis of radio-AGN fractions to higher redshift ranges than previously explored.

2. The type of galaxies that host radio-AGN shows strong evolution as a function of redshift, from predominantly dusty, star-forming hosts in interacting or merger environments ($1 < z < 2.25$), to predominantly quiescent hosts at $z < 1$.

3. This evolution is in line with the overall evolution of massive galaxies onto the red-sequence.

4. The above findings are in good general agreement with earlier work, particularly that of Rocca-Volmerange et al. (2013) and De Breuck et al. (2002).

5. Radio-AGN become particularly rare at halo masses below 10^{12} $M_{\odot}$, suggesting that radio-AGN activity may be closely linked to high-halo masses.

6. Finally, our radio-AGN hosts show star-formation and specific star-formation rates consistent with non-radio-AGN hosts of similar stellar-mass and redshift, in good agreement with earlier work out to $z \sim 0.7$ (Johnston et al., 2008; Chen et al., 2013).

In summary we find that radio-AGN hosts show no statistical differences from non-hosts across a broad redshift range ($0.25 \leq z < 2.25$) and that the fraction of galaxies containing radio-AGN at a given stellar-mass is independent of both redshift and host type. Ultimately, by including these observations into models of AGN feedback and triggering, we hope that new insights may be gained into how these powerful objects both form and evolve.

We would like to thank the Mitchell family for their continuing support of the ZFOURGE project. We would also like to thank the Carnegie Observatories and the Las Campanas Observatory for providing the facilities and support needed to make ZFOURGE what it is today. Australian access to the Magellan Telescopes was supported through the National Collaborative Research Infrastructure Strategy of the Australian Federal Government. This research has made use of NASA's Astrophysics Data System. This research has made use of the NASA/IPAC Extragalactic Database (NED) which is operated by the Jet Propulsion Laboratory, California Institute of Technology, under contract with the National Aeronautics and Space Administration. This research made use of APLpy, an open-source plotting package for Python hosted at http://aplpy.github.com. This research made use of Astropy, a community-developed core Python package for Astronomy (Robitaille et al., 2013). This work made use of the IPython package (Pérez & Granger, 2007). This research made use of matplotlib, a Python library for publication quality graphics (Hunter, 2007). PyRAF is a product of the Space Telescope Science Institute, which is operated by AURA for NASA. This research made use of SciPy (Jones et al., 2001–). GGK was supported by an Australian Research Council Future Fellowship FT140100933."

3

VLBI vs radio-loud AGN hosts

Overview

"Are the hosts of VLBI selected radio-AGN different to those of radio-loud AGN?"
G. A. Rees, R. P. Norris, L. R. Spitler, N. Herrera-Ruiz, E. Middelberg
Monthly Notices of the Royal Astronomical Society: Letters, Volume 458, Issue 1,
p.L49-L53, (2016)

This chapter is based upon Rees et al. (2016) and presents work cross-matching a sample of deep VLBI observations with high quality near-infrared observations from the NMBS survey. We perform a similar analysis to the previous chapter, finding that VLBI sources are not only a sub-set of the radio-loud AGN sample but are representative of the radio-loud AGN population in terms of their host galaxy properties.

I was responsible for leading and writing the manuscript presented in the following chapter. I was also responsible for the cross-identification of radio sources found within deep VLBI observations in the COSMOS field with K_s-band observations in the NMBS surveys and all subsequent analysis of these sources.

L. R. Spitler and R. P. Norris supervised this work with respect to the methods used and scientific interpretation, as well as providing valuable and continuous feedback. N. Herrera-Ruiz and E. Middelberg planned, performed and reduced the VLBI observations. Overall my contribution to the work presented in this Chapter is 90%.

3.1 Abstract

Recent studies have found that radio-AGN selected by radio-loudness show little difference in terms of their host galaxy properties when compared to non-AGN galaxies of similar stellar-mass and redshift. Using new 1.4 GHz VLBI observations of the COSMOS field we find that approximately 49±8% of high-stellar-mass ($M > 10^{10.5}$ $M_\odot$), high luminosity

($L_{1.4} > 10^{24}$ W Hz^{-1}) radio-AGN possess a VLBI detected counterpart. These objects show no discernible bias towards specific stellar-masses, redshifts or host properties other than what is shown by the radio-AGN population in general. Radio-AGN that are detected in VLBI observations are not special, but form a representative sample of the radio-loud AGN population.

3.2 Introduction

Very Long Baseline Interferometry (VLBI) achieves angular resolutions at the milli-arcsecond level and as such traces only the most compact and intense sources of radio emission. On extra-galactic scales such compact emission can be attributed to either Active Galactic Nuclei (AGN), extreme clusters of Supernovae (SNe) or Supernova Remnants (SNRs). It is only in the local Universe and in the most active of star-forming galaxies however that SNe and SNRs can reach sufficient brightness to be detected by VLBI (Kewley et al., 2000; Norris et al., 2007). Indeed, even the deepest VLBI observations (RMS $\sim$ 10 μJy) struggle to detect SNe and SNRs at high redshifts ($z > 0.1$). Above this, objects detected in such high sensitivity VLBI observations correspond to brightness temperatures of over 3×10^5K and are thus inconsistent with radio emission from star-formation (Condon et al., 1991). Above $z > 0.1$, VLBI-detected sources also possess radio luminosities several times brighter than can be generated by reasonable SNR and SNe rates (Kewley et al., 2000) or even by multiple simultaneous occurrences of the brightest supernovae currently known (Parra et al., 2010). As a result, VLBI observations offer an unambiguous way of identifying radio-AGN.

Many techniques for identifying radio-AGN focus on selecting objects with extreme radio luminosities or excesses emission in the radio-band when compared to other wavelengths. Radio-AGN identified in this way trace large scale jets and diffuse radio lobes associated with much larger temporal and physical scales than those selected by VLBI. Because of this it is possible that these two distinct methods of selecting radio-AGN may result in very different samples. Indeed VLBI observations tend to detect only 10-50% of radio-loud AGN (Middelberg et al., 2011, 2013; Chi et al., 2013; Deller & Middelberg, 2014; Herrera Ruiz et al., 2016). Is this because these are the earliest phases of the radio-AGN life-cycle or are they perhaps special in some other way?

To test VLBI selected AGN against radio-loud AGN we can either study the properties of the AGN itself or investigate the impact it has on its host galaxy. In Chapter 2 we found that the likelihood of a galaxy hosting a radio-loud selected AGN increases strongly with increasing stellar-mass. At a given stellar-mass, ellipticals and star-forming galaxies are equally likely to be radio-loud, and the optical/IR properties of radio-loud galaxies are indistinguishable from those of radio-quiet galaxies in the redshift range $0.25 < z < 2.25$. So do VLBI-detected radio-AGN hosts follow the same evolutionary trends as their radio-loud counterparts?

In this Chapter we analyse the host galaxy properties of VLBI-detected and radio-loud selected AGN in the COSMOS (Cosmological Evolution Survey) field and compare the resulting samples across a broad redshift range in terms of their host star-formation rate, color, infrared-AGN detection rate, stellar-mass, dust content and radio-loudness.

3.3 Data

Our primary infrared data set is the Newfirm Medium Band Survey (NMBS, Whitaker et al. 2011) COSMOS field (Giacconi et al., 2001; Schinnerer et al., 2004), which covers an area of $27.6' \times 27.6'$ down to a 5-sigma total magnitude of 23.5 in K–band. Using these observations along with a large amount of ancillary data, NMBS produces high quality photometric redshifts ($\Delta z \sim$ 1-2%), stellar-age, stellar-mass, dust-content, star-formation rates for approximately 24,000 galaxies in the COSMOS Deep field. Using Figure 3.1 we split this sample into Quiescent or Star-forming hosts using the classifications of Wuyts et al. (2007).

Low resolution radio data for the field is taken from the 1.4 GHz Very Large Array (VLA) Cosmos Deep Project (Schinnerer et al., 2010) which has a central RMS of 10 μJy per beam. The COSMOS Deep Project covers the all of the NMBS K_s/K-band observations with an angular resolution of $2.5'' \times 2.5''$.

Our high resolution 1.4 GHz radio data consists of deep targeted milli-arcsecond VLBI observations of each of the 2865 radio sources in the COSMOS field (Herrera-Ruiz et al., in prep). These observations were carried out on the Very Long Baseline Array and were designed to match both the maximum depth of the of the VLA Cosmos Deep Project (10 μJy per beam) and the variation in this parameter across the field. The radio-IR identifications, in the area of overlap between the VLBI and NMBS data, are taken from Rees et al. (2016). The resulting sample contains 385 VLA sources with NMBS counterparts and of these 64 have VLBI-detected emission.

We further categorise all our radio sources into either radio-loud AGN or radio detected star-forming galaxies based upon their radio based star-formation rate (radio-SFR) versus a combined ultraviolet and bolometric infrared star-formation rate (UV+IR-SFR) (Figure 3.2).

3.4 Analysis

The result of this process is a large sample of galaxies with information on stellar-mass, SFR, dust content, redshifts and host type which can be flagged to select radio-AGN by either radio-loudness or by VLBI detection.

3.4.1 Defining the analysis samples

To compare the VLBI and radio-loudness selection techniques we create several different sub-samples. Our "Sensitivity Limited sample" is limited to sources with VLA fluxes > 50μJy to achieve uniform sensitivity across the field. Combining the requirements of the "Sensitivity Limited" sample with further limits on stellar-mass ($M > 10^{10.5}$ $M_\odot$), redshift ($0.25 \leq z \leq 2.25$) and VLA radio luminosity ($L_{1.4} \geq 2\times10^{24}$ WHz^{-1}) in order to have a complete sample of radio objects within our redshift range, produces our "High-Mass/High-Luminosity" (HM/HL) sample of radio-AGN.

We also produce a "stellar-mass limited" sample of non-AGN which are simply those in NMBS above $10^{10.5}$ $M_\odot$ and note that this is above the 90% NMBS stellar-mass completeness limit out to z=2.20 (Wake et al., 2011).

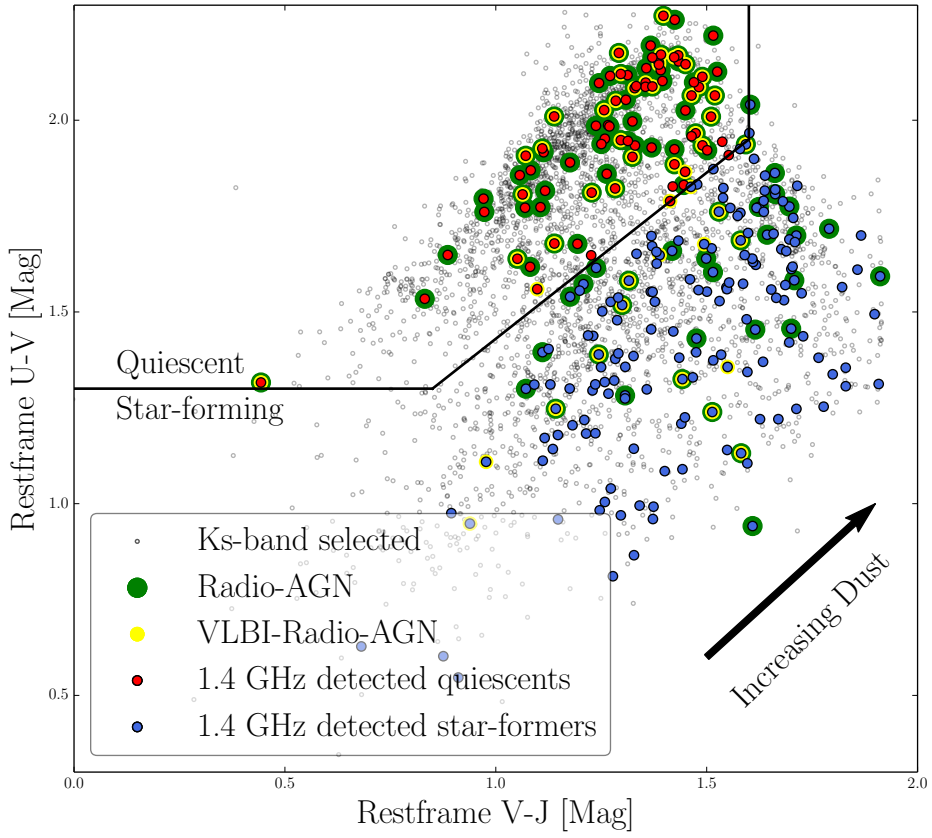

Figure 3.1: A rest-frame, UVJ colour-colour diagram for radio-detected star-formers (blue circles), radio-detected quiescent galaxies (red circles) and the NMBS K_s-band stellar-mass-limited sample (grey circles). Radio-loud AGN are highlighted (large green circles) and those selected based on VLBI detections are also shown (large yellow circles). For clarity only 10% of the radio non-detected sources are plotted. Interestingly a large number of VLBI detections are found in actively star-forming hosts.

Finally we build the "stellar-mass similar" control sample by randomly sampling NMBS detected galaxies of similar redshift (same bin) and stellar-mass (± 0.1 $M_\odot$) for each VLBI-detected radio-AGN. The median value of the control samples properties is then measured. This process is repeated 1000 times to probe the range of values seen in the control sample and the median of these runs is then plotted with the standard deviation between the 1000 runs shown as the associated error. A full description of this process can be found in Chapter 2.

3.4.2 Are VLBI selected radio-AGN special?

Figure 3.3 shows the Cumulative Distribution Functions for our VLBI selected and radio-loud selected sensitivity limited samples in terms of stellar-mass, specific star-formation rate (SSFR), redshift and dust content (as visual extinction). KS-testing these two populations shows no significant differences between them with P values ranging from P = 0.32 and up (Table 3.1). Table 3.1 also shows the KS-test statistics when comparing the HM/HL VLBI sample to both HM/HL radio-loud AGN and the stellar-mass-similar sample. Even in this stellar-mass and radio luminosity complete regime we see little difference between VLBI selected radio-AGN and the radio-loud AGN or stellar-mass-similar samples.

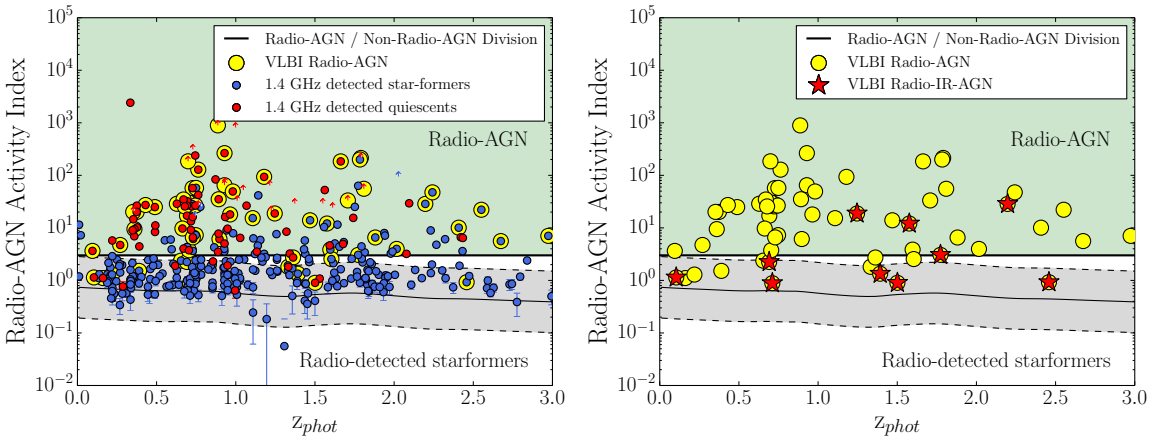

Figure 3.2: The Radio-AGN Activity index: This is simply the ratio of radio based SFR (Bell, 2003; Karim et al., 2011) to UV+IR based SFRs (Bell et al., 2005; Kennicutt, 1998). Both of these SFRs are normalized to a Chabrier Initial Mass Function (IMF) (Chabrier, 2003) and radio-SFR is calculated using a radio spectral index α = -0.3 (where S $\propto \nu^{\alpha}$) in order to match the spectral index of the radio end of the Wuyts et al. (2011) template used for calculating UV+IR SFR for star-forming objects. Objects with a radio-SFR more than 3 times higher than their UV+IR SFR (5 sigma above the Wuyts average star-former template) are classified as radio-loud AGN (green shading). Objects identified as Radio-AGN by VLBI detection are highlighted (yellow circles). We see good agreement between the techniques with the majority of VLBI sources. Right: VLBI objects below the radio-loud line are radio-quiet and of these 13 sources, 6 (46^{+13}_{-12}%) possess infrared colors identifying them as infrared-AGN using the Donley et al. (2012) wedge (red stars).

	All: VLBI vs RL	HM/HL: VLBI vs RL	HM/HL VLBI vs Stellar-mass Sim
P Value	0.86, 0.58, 0.32, 0.91	0.99, 0.86, 1.00, 0.77	0.98 0.20 0.98 0.36
D Value	0.09, 0.11, 0.14, 0.08	0.10, 0.16, 0.10, 0.17	0.13 0.30 0.13 0.26
Numbers	64, 143	21, 37	21, 1217

Table 3.1: A comparison of the stellar-mass, specific star-formation rate redshift and dust-contents (through visual extinction) of our three samples using the KS-test statistics. Column 1 compares the VLBI-selected against the radio-loud selected AGN samples (both sensitivity-limited). Column 2 applies a luminosity and stellar-mass cut-off to both samples to ensure they are complete across our redshift range. Column 3 uses the same luminosity and stellar-mass cut-off for the VLBI sample and compares it against the stellar-mass and redshift-similar non-AGN population. We find that in all three cases, the samples are indistinguishable from each other.

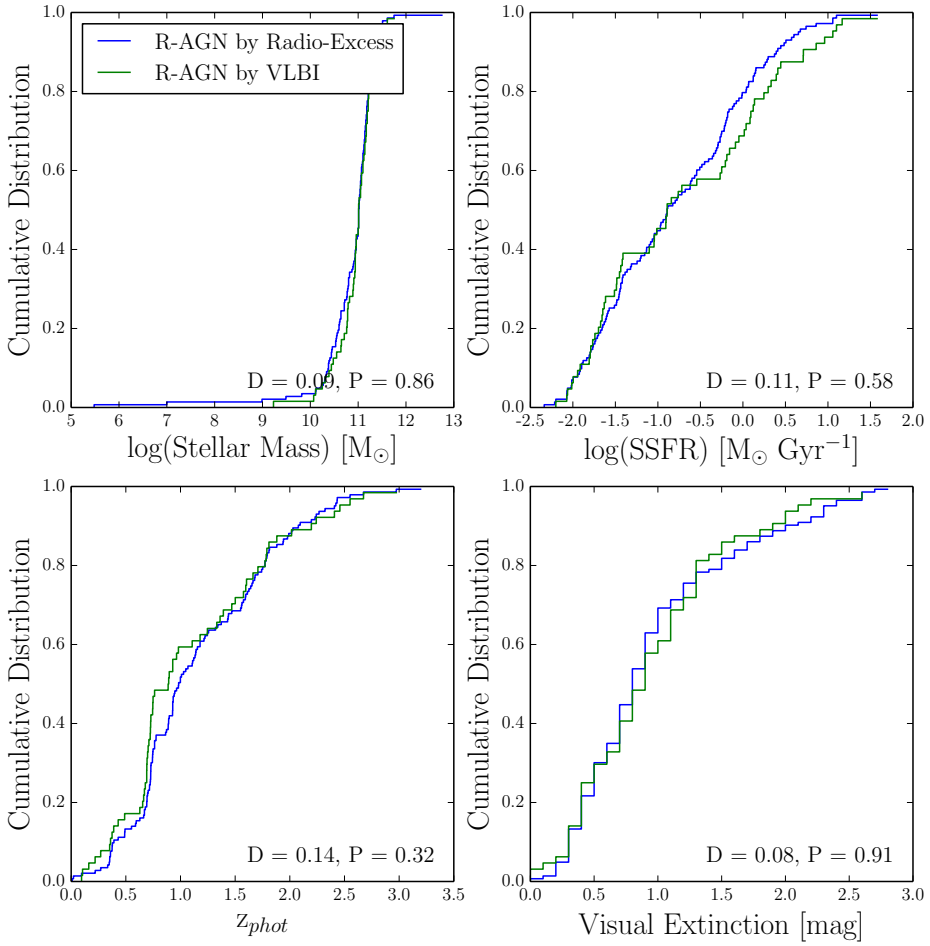

Figure 3.3: The Cumulative Distribution Functions for VLA detections above 50μJy, split by VLBI and radio-loud selected AGN, against stellar-mass, SSFR, redshift and visual extinction. We find no significant differences between the two populations using a KS-test where significant is considered to be P values < 0.10 and note that this similarity continues to hold when comparing only the HM/HL radio-AGN population.

Overall we find that VLBI detections are present for 51/143 (36±4%) [1] of our sensitivity limited radio-loud AGN population and 18/37 (49±8%) of the HM/HL radio-loud AGN population. Combining this with the result above suggests that VLBI selects a representative sample of radio-loud AGN and that studies using either selection method should be largely comparable.

It is also possible to study where the radio-loud selection techniques fail. In Figure 3.2 we can see that for the sensitivity limited sample, 13/64 VLBI-detected radio-AGN are missed by the radio-loudness identifier. Limiting to the high-stellar-mass, high-luminosity sample we find that this radio-quiet fraction is considerably lower with only (3/21) VLBI sources failing the radio-loudness criteria. This is in good agreement with the predicted incompleteness of the same sample in Chapter 2 where we estimated that 12^{+6}_{-3}% of their radio-loud AGN to appear radio-quiet due to simultaneous infrared emission from the AGN which causes an artificial increase in the UV+IR SFR.

[1] All percentage and fraction errors in this chapter are 1-sigma values calculated using the beta confidence interval as described by Cameron (2011).

So how many of our radio-quiet VLBI sources contain IR-AGN? Using the Donley wedge (Donley et al., 2012) to identify AGN by infrared color we find that 6/13 (46^{+13}_{-12}%) of the sensitivity limited radio-quiet VLBI sources are identified as IR-AGN. Correspondingly in the high-stellar-mass, high luminosity sample, this value increases to 2/3 or 66^{+15}_{-28}%. For both of these samples the median ratio of VLBI to VLA flux is 54±8%. This supports the idea that near and far infrared emission from AGN activity can result in a significant number of radio-loud AGN being mis-classified as radio-quiet or radio star-forming galaxies.

3.4.3 Comparing VLBI-detected radio-AGN, radio-loud AGN and the stellar-mass similar sample

Our HM/HL VLBI selected AGN samples are shown in Figure 3.4. This is simply the number of HM/HL VLBI-detected sources divided by the number of stellar-mass-limited objects, as a function of redshift (left panel) and stellar-mass (center panel). We see no evolution in terms of redshift for the range provided and a correlation with stellar-mass, both trends are in good agreement with the those seen previous work on the radio-loud AGN population (Best et al., 2005; Simpson et al., 2013; Rees et al., 2016). Lastly, evolution of VLBI radio-AGN host types (Quiescent or Star-Forming as defined in Figure 3.1) are shown to be in reasonable agreement with the evolution of their stellar-mass and redshift similar control sample (right panel).

3.5 Discussion

The idea that VLBI selected sources and radio-loud sources are highly similar is interesting as we might reasonably expect to identify some differences between the samples. Radio-AGN selected by radio-loudness preferentially picks out objects with relatively high radio emission for their IR emission. VLBI on the other hand selects samples with high surface brightness emission from compact sources. Despite this, we see no indication that the host galaxies of VLBI scale radio-AGN ($F_{1.4} \geq 50\mu$Jy, $\theta \sim 1$ mas) form a special subset of radio-loud AGN.

One obvious way to explain this result is the idea, proposed by Hickox et al. (2014), that each active period of AGN activity is too short to directly correlate with changes in their host properties. Under this scenario, radio-AGN move periodically from active to inactive states far more rapidly than they can impact their host. As such, our sample of VLBI-detected radio-AGN are simply a random sub-sample of radio-loud AGN and hence would show little difference in their host galaxy properties.

Finally, we find that 10% of VLBI-detected sources are classified as radio-quiet despite having on average more than 50% of their radio flux being emitted on VLBI scales. This implies that even though we might expect star-formation to provide the majority of radio emission in radio-quiet AGN below 100 μJy (Padovani et al., 2011; Bonzini et al., 2013), a significant fraction of the radio emission from radio-quiet AGN above 50 μJy is in fact from the AGN core. Furthermore, a high fraction of these VLBI-detected radio-quiet AGN show strong signs of AGN-based emission in the infrared, acting as a mask for their strong radio-emission.

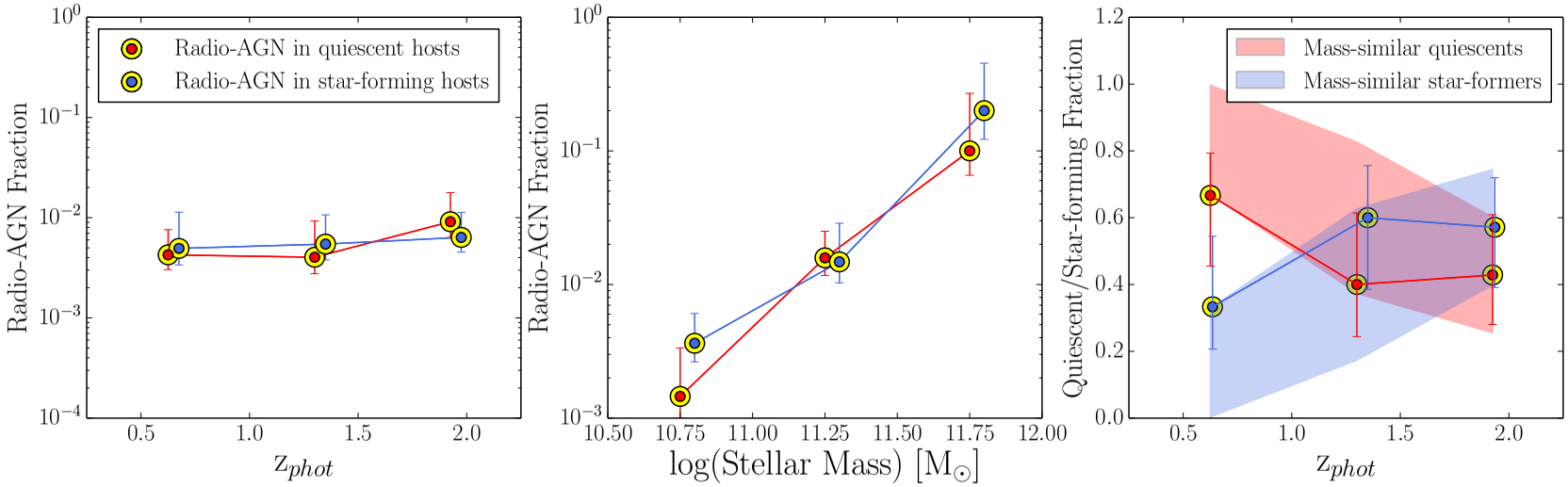

Figure 3.4: HM/HL VLBI detection fractions. Left: Detection fractions broken up into star-forming (blue circles) and quiescent (red circles) hosts. Essentially this is the number of HM/HL VLBI-detected sources divided by the number of NMBS sources above $10^{10.5}$ $M_\odot$ as a function of redshift. Center: Same as left panel but as a function of stellar-mass. Right: Here we plot the fraction of each host type as a function of redshift for HM/HL VLBI-detected sources and the stellar-mass similar sample.

3.6 Conclusions

We find that:

1. VLBI selected sources account for 36±4% of radio-loud AGN detected above 50μJy. For our complete sample comprised of high stellar-mass, high radio luminosity sources, this fraction increases to 49±8%.

2. Importantly while VLBI-detected radio-loud AGN only account for a moderate proportion of the overall radio-loud AGN sample their hosts are statistically representative of the whole radio-loud population.

3. Specifically VLBI selected radio-loud AGN hosts possess stellar-masses, SSFRs, redshifts and dust contents indistinguishable from the hosts of radio-loud AGN.

4. This means that studies conducted using VLBI-selected samples should be in good agreement with those performed on radio-loud selected samples.

5. Finally we find that 20^{+6}_{-4}% of VLBI-detected sources are radio-quiet (14^{+11}_{-4}% for the high stellar-mass, high radio luminosity VLBI-detected sample). This implies that the radio luminosity from some radio-quiet AGN can not be attributed primarily to star-formation activity.

This work made use of data taken on the National Radio Astronomy Observatory's Karl G. Jansky Very Large Array. The NRAO is a facility of the National Science Foundation, operated under cooperative agreement by Associated Universities, Inc

"But it's turtles all the way down!"

A little old lady

4

Measuring cosmology using deep 100 square degree radio continuum surveys

Overview

Measuring cosmology using deep 100 square degree radio continuum surveys
Contributors: G. A. Rees, R. P. Norris, L. R. Spitler, D. Parkinson, A. N. O'Brien, I. Heywood, F. Rahman, D. Bacon.

This chapter presents work measuring and modelling of the auto-correlation function and power spectra for two deep and one large radio continuum surveys. It will shortly be submitted as a paper to the Monthly Notices of the Royal Astronomical Society.

I was responsible for leading and writing the work presented in the following chapter. This project is part of a collaboration to produce a standard cosmology pipeline for EMU and as such a substantial proportion of my time was spent on producing not just singular data products but on developing, testing and applying new and existing software for the rapid and easy application of a wide range of analysis techniques to the EMU. Specifically I produced scripts to help automate many of the analysis techniques used in this chapter. Making use of the Healpy software package and completely new code, I automated the production of maps and masks of the radio sky in both Healpix and pair-counting scripts. I calculate both the angular power spectrum using Polspice and the auto-correlation function using a KD-Tree pair counting implementation and fit these using appropriate power law functions. I developed scripts to convert between measured correlation functions and power spectra, estimate errors on observed functions and calculate a range of observable parameters such as survey area, source surface density and the bias and redshift distribution of the SKADS simulation. Furthermore I also was responsible for documenting my own and others contributions to the pipeline using standard formatting.

R. P. Norris, L. R. Spitler, D. Bacon and D. Parkinson supervised this work with respect to the methods used and scientific interpretation, as well as providing valuable and continuous feedback. A. N. O'Brien scheduled, observed and reduced the ATLAS-SPT observations

which we used for one section of our analysis and I. Heywood observed and reduced the JVLA observations of the STRIPE-82 field. This work would not have been possible without the help of D. Parkinson and F. Rahman who as part of the EMU Cosmology team have helped de-bug, test and write sections of code. Specifically, I would not have achieved the fast numerical modelling of the angular power spectrum for radio galaxies accurately at low values of ℓ without their significant help. Overall my contribution to the work presented in this chapter is 85%.

4.1 Abstract

As preparation for measuring cosmological parameters with the Evolutionary Map of the Universe survey, we have measured the angular correlation function of radio sources in two medium-deep radio surveys. We find that it differs from that measured at higher flux densities in showing a lower gradient at small angular separations, which we attribute to the smaller number of double-lobed radio sources at lower flux densities. We also measure the NRAO Very Large Array Sky Survey (NVSS) survey auto correlation function and angular power spectrum finding them in excellent agreement with previously reported results. We semi-empirically model the radio emission from a simulated data set, obtained from the Millennium simulation via the Theoretical Astrophysical Observatory, and find that the auto correlation function of the resulting simulated radio sources agrees well with the clustering of real sources at scales greater than 0.1 degrees, but lacks the excess power caused by double lobed radio sources at scales less than 0.1 degrees. We numerically model the expected auto correlation function for each of our surveys using the redshift distribution of the Square Kilometre Array Design Studies Semi-empirical Extragalactic Simulation and a linear bias of 1.8, finding that the Lambda Cold Dark Matter version of these models shows good agreement with the measured values despite the large errors associated with such small fields. Finally, in line with more traditional methods for radio cosmology we also measure the spatial correlation length $r_0^{\epsilon=0} = 2.2 \pm 0.9$ h^{-1}Mpc for the Australia Telescope Compact Array survey of the South Pole Telescope field and find it to be in good agreement with the correlation lengths measured at higher fluxes.

4.2 Introduction

In the standard model of cosmology the Universe undergoes a brief period of rapid inflation in the first few moments after the Big Bang. As a result of this, observations of the early Universe, for example the cosmic microwave background, show a incredible level of isotropy, with variations in temperature of less than 0.00003K (Smoot et al., 1992; Fixsen et al., 1996; Bennett et al., 2013; Planck Collaboration et al., 2016). Despite this incredible uniformity at early times, the Universe has clearly evolved from this initial state into the collection of galaxies, clusters and voids we see today. Dominated by gravity for much of its evolution, these structures have formed from the growth of minute inhomogeneities in the initial state. Areas of over-density collapsed to form galaxies, clusters and filaments, while under-dense regions, stripped of what little matter they already contained, grew, becoming progressively less populated with galaxies at later epochs. Because of this, the positions of galaxies are accurate, albeit potentially exaggerated, tracers of the underlying distribution of matter.

By analysing the patterning of galaxies caused by these effects, it is possible to measure the underlying cosmological properties of our Universe, and over the years, many such attempts have been made. Finding that the clustering of galaxies depends strongly on both the redshift (Davis & Peebles, 1983; Le Fevre et al., 1996; Carlberg et al., 2000; McCracken et al., 2001) and type of galaxy selected by the sample, with ellipticals typically showing much stronger clustering than star-forming galaxies across a wide range of redshifts (Longair & Seldner, 1979; Guzzo et al., 1997; Willmer et al., 1998; McCarthy et al., 2001; Daddi et al., 2002; Norberg et al., 2002), these early studies suggest that certain galaxy samples are far more effective at tracing the underlying dark matter distribution than others.

In this regard, large samples of radio galaxies have been shown to have great promise. Being almost completely unaffected by extinction, radio surveys can provide accurate source counts across very large areas of sky. This combined with a much broader source redshift range, allows them to sample much larger cosmic volumes and probe cosmology at much earlier epochs than studies at other wavelengths. Finally, radio galaxies have been shown to have a much higher 'bias' than galaxies selected at other wavelengths (Blake & Wall, 2002a; Lindsay et al., 2014; Jarvis et al., 2015), making them extremely sensitive to variations in the underlying distribution of matter and hence excellent probes of cosmology.

Unfortunately the broad redshift range of radio galaxies also makes the detection of a cosmological signal more difficult, as we observe many separate instances of spatial clustering flattened onto the sky. Because of this, there was initially some concern that the clustering of radio galaxies would be undetectable (Webster & Pearson, 1977; Griffith, 1993). Despite these worries, marginal detections were eventually found in the observations of both the 1.4 GHz Green Bank survey (Kooiman et al., 1995) and the Parkes-MIT-NRAO survey (Loan et al., 1997).

In more recent years, large radio surveys such as FIRST (Becker et al., 1995), WENSS (Rengelink & et al., 1998), SUMSS (Mauch et al., 2003) and NVSS (Condon et al., 1998), have reached a sufficient size and depth to provide the first stepping stones towards new constraints on modern cosmology (Blake & Wall, 2002b,a; Blake et al., 2003; Overzier et al., 2003; Blake et al., 2004; Chen & Schwarz, 2015; Lindsay et al., 2014; Lindsay, 2015). In the future, these constraints are expected to become truly competitive, with deep all-sky radio surveys (such as the Evolutionary Map of the Universe, (Norris et al., 2011) and The GaLactic and Extragalactic All-sky MWA survey, GLEAM, (Wayth et al., 2015)) predicted to produce exceedingly accurate constraints on a wide range of cosmological parameters, including but not limited to: primordial non-gaussianity, modified gravity and dark energy (Norris et al., 2011; Raccanelli et al., 2011; Camera et al., 2012).

Whilst the most common technique for clustering analysis at other wavelengths is the precision measurement of spatial (or 3D) clustering via photometric or even spectroscopic redshifts, this is not yet possible in the radio continuum regime, without the use of cross-matching with super deep optical and near infrared surveys. Since the majority of the highest redshift sources will not be detectable in large optical and infrared surveys, this technique results in the loss of the high redshift sources unique to radio cosmology studies, thus removing one of the prime benefits of a radio selected sample.

Despite this setback, the clustering of radio galaxies can still be determined without the

use of any distance information using techniques such as the Angular Power Spectrum (C_ℓ) and Angular Correlation Function, $\omega(\theta)$. These methods determine the clustering of galaxies not in the full three dimensions they are truly mapped in, but in the two angular dimensions they are projected onto. While some information is lost with these techniques, they are made possible by the power-law like form of the spatial correlation function. Projecting a power-law spatial correlation function onto a sphere has been shown to result in another power-law (Peebles, 1980) and as such the vast majority of information in the spatial power-law is conserved and measurable in the angular projection of it.

The angular two point correlation function quantifies the clustering of galaxies as the number of galaxy pairs at any given separation, above what one might expect from a random distribution. In a naive application of this technique, the CPU time required scales with the number of sources squared and also increases in difficulty with maximum separation used, as the calibration of source positions over large areas becomes increasingly important. As such rapidly calculating it for very large surveys can be exceedingly challenging.

The Angular Power Spectrum measures the variation in the density of galaxies on the sky as the sum of a series of spherical harmonic functions. While this technique works well on large scales it becomes more difficult to calculate at smaller separations. Because of this these two techniques are synergistic, allowing rapid calculations of the clustering of galaxies at both large and small scales. The transformation between them can be achieved using

$$\omega(\theta) = \frac{1}{4\pi} \sum_{0}^{\infty} (2\ell + 1) C_\ell P_\ell(cos\theta), \tag{4.1}$$

and

$$C_\ell = 2\pi\sigma_0^2 \int_{-1}^{+1} \omega(\theta) P_\ell(cos\theta)\ \delta(cos\theta), \tag{4.2}$$

where σ_0 is the source surface density and P_ℓ is the Legendre polynomial.

In preparation for the next-generation radio-continuum survey the Evolutionary Map of the Universe (EMU, Norris et al. (2011)) we are developing software to implement a number of cosmological techniques for both the modelling and analysis of correlation functions and power spectra. Here we apply them to surveys of either similar depth or area to the predicted EMU survey parameters. We first reproduce the Blake & Wall (2002a) and Blake et al. (2004) analysis of the NVSS survey before applying the same techniques to two, 100 square degree, μJy sensitivity fields, observed with the Jansky Very Large Array (JVLA) and Australian Telescope Compact Array (ATCA) as part of the ATCA Large Area Survey (ATLAS). We next develop a new method of predicting auto-correlation functions for deep radio surveys, based on empirical relations linking radio flux to galaxy stellar-mass and star-formation rates and compare these predictions to both the observed correlations and those predicted using more traditional numerical modelling techniques.

In Section 4.3 we outline the various surveys used for this analysis. Section 4.4 outlines the methodology behind our correlation function and angular power spectrum techniques and

Section 4.5 applies these techniques to each of our selected data sets. Sections 4.6 outlines our development of a empirical process for converting semi-analytic N-body cosmology simulations and the resultant auto-correlation function produced, whereas Section 4.7 details our approach for numerically modelling radio auto correlation functions for any given cosmology. Finally in Section 4.8 we consider the implications of these results along with outlining ideas for future work on this topics and Section 4.9 outlines our conclusions.

Throughout this paper we assume a cosmology of $\Omega_m = 0.25$, $\Omega_\Lambda = 0.705$, $\Omega_b = 0.045$, $\sigma_8 = 0.9$, h = 0.73, n = 1 unless otherwise stated.

4.3 Data

4.3.1 NVSS

The NVSS survey covers the entire sky north of -40 deg declination down to a limiting RMS of 0.45 mJy/beam at 1.4 GHz. With a beam FWHM of 45 × 45 arc-seconds, the survey nevertheless reaches very good astrometric accuracy for bright sources ($S_{1.4}$ > 15mJy) of < 1″ uncertainty in RA and DEC. Our sample is drawn from the Condon et al. (1998) catalog of NVSS sources.

Due to sensitivity variations across the NVSS survey, only sources with fluxes greater than 15mJy (≈33 sigma) are considered for this analysis in order to keep the source surface density constant across the field. This reduces the number of sources to be analysed (and increases the shot noise) but minimizes the impact of varying source surface density across the field caused by the location dependent survey sensitivity. In addition to this, several large extended radio sources appear in NVSS as a collection of smaller components and thus add a large number of false correlations on small to medium scales. These were masked manually in the initial analysis by Blake & Wall (2002a), with all sources within a given area around the central bright source being removed from our sample. Because we mask certain areas of the NVSS survey, it is also necessary to equally mask the random catalogues used for the correlation function analysis. Hence any source generated for the random catalogue (See section 4.4) that falls within a masked area, is also removed. Finally, the galactic plane is also masked, where all sources (real and random) in the galactic latitudes ℓ ±5deg are removed from the analysis. All masks are listed in Appendix C for reference purposes.

4.3.2 JVLA Stripe-82

Our secondary data set is the new JVLA observations of Stripe-82 (S82 hereafter) in the compact CnB configuration (Heywood et al., 2016). Importantly for our work, the observations are split into two nearly equal strips separated by 20 degrees in RA. However due to unfortunate observing constraints a large section in the center of the Western field was not observed. Therefore we only include the Eastern field of this data set in our analysis. While these observations have a lower resolution than the well known Hodge et al. (2011) observations of the same field, they still achieve a FWHM of 16″ × 10″ per beam and a mean noise of 88 μJy per beam. Furthermore the Heywood et al. (2016) images achieve far better survey uniformity, and to minimize the effects of survey sensitivity variation even further, we here utilise only the central portion of the Eastern field in the region -1.0 < Dec < 0.3

and 330.3 < RA < 350.0, in doing so we reach a superb survey uniformity, with the RMS reaching more than twice the survey average in only 2 pointings (or ≈2% of used pointings). In order to remove the effects of both the decreased sensitivity and typical pointing pattern variations inherent to the edges of small fields, we remove all sources within 0.1 degrees of the designated field edge from our analysis.

4.3.3 ATLAS-SPT

Our final data set is the pre-release 1.4 GHz selected catalogues from the Australian Telescope Compact Array South Pole Telescope Survey (ATLAS-SPT) (O'Brien et al., 2015). These observations cover a continuous area of 100 square degrees (10 × 10 degrees) down to a average RMS of 100 μJy per beam with an angular resolution of 8 arc-seconds. We remove all sources within 0.1 degrees of the designated field edge from our analysis. The final 98 square degree field is extremely uniform in sensitivity with the maximum RMS never reaching more than 136μJy or 1.7 times the minimum RMS of the field. We therefore analyse all sources over 300μJy (3 sigma) in the catalogue.

4.4 Methodology

4.4.1 Auto Correlation Function via Machine Learning

The first of our analysis techniques is the angular two point correlation Function w(θ). In its simplest form this can be thought of as the excess probability of finding two galaxies separated by a given angle (θ) compared to a Poissonion distribution (Peebles, 1980),

$$\delta P = \sigma_0[1 + \omega(\theta)]\delta\Omega, \tag{4.3}$$

where δP is the probability, σ is the mean surface density and $\delta\Omega$ is the surface area element.

Observationally $\omega(\theta)$ can be calculated in its simplest form by calculating the number of pairs of galaxies at each angular separation (DD) and dividing this by the number of pairs of random sources at each angular separation in a equal area of sky (RR). Hence,

$$\omega(\theta) = \frac{DD}{RR} + 1. \tag{4.4}$$

More advanced forms of this estimator help to minimize the variance in this calculation by adding additional terms such as the cross-pair count (DR(θ)) (Landy & Szalay, 1993) and it is this particular form of the correlation function that we employ here,

$$\omega(\theta) = \frac{DD - 2DR + RR}{RR}. \tag{4.5}$$

The traditional method to calculate the error on this function is via the Possionian error on the DD counts alone. This is justified by assuming that over numerous instances of RR and DR, the error on the average of these functions will be insignificant in comparison to the variance on DD. Hence the errors on $\omega(\theta)$ may be approximated as:

$$\Delta\omega = \frac{1 + \omega(\theta)}{\sqrt{DD}}. \tag{4.6}$$

In practice, this approximation has been found to under represent the true error on $\omega(\theta)$, particularly at high angular separations (Blake & Wall, 2002a). To address this issue, an alternate approach is to perform a bootstrap analysis of the observed correlation function. Bootstrapping randomly samples the initial data, and hence each object can be chosen multiple times for the sub-sample, or not at all. Because of this, each sub-sample will result in a slightly different correlation function, and by running this sampling process thousands of times, we produce a map of the true variance in the correlation function and take the average of this spread to be our observed $\omega(\theta)$.

As with all auto correlation functions based on pair counts, there exists several issues with their implementation and effective use. Firstly naive pair-counting scales with N^2 and requires several thousand iterations of random counts to effectively model the 'expected' random (RR) and real-random (DR) counts. For large surveys this effect is minor at small scales, as there are a large number of small patches in any one random realisation of the full field.

Finally for small survey areas, there is one important effect to be corrected for; the integral constraint (Groth & Peebles, 1977), which applies a negative offset of ρ^2 to the correlation function,

$$\rho^2 = \frac{\sum RR(\theta)\omega(\theta)}{RR(\theta)}. \tag{4.7}$$

After correcting for this effect, the final auto correlation function is then fitted using the best fitting sum of two power-laws of the form $\omega = A\theta^b$. The best fit parameters of the powerlaw dominated by galaxy clustering and extended sources are referred to hereafter as by the subscript 'Clustering' and 'Size' respectively.

Using an inversion of the cosmological Limber Equation (Limber, 1953; Peebles, 1980) it is possible to calculate an estimate of the three dimensional spatial correlation length, r_0. To do this we need an estimate of the redshift distribution of sources, p(z), the amplitude (A) and slope (b) of the fitted auto correlation function, an assumed form for the spatial correlation function (ξ), a clustering parameter (ϵ) and a cosmology.

We choose to use an epoch independent form of the spatial correlation function (de Zotti et al., 1990; Overzier et al., 2003; Blake & Wall, 2002a; Lindsay et al., 2014) to allow for redshift dependant clustering,

$$\xi(r_p, z) = \left(\frac{r_p}{r_0}\right)^{-\gamma} (1 + z)^{-(3+\epsilon)}, \tag{4.8}$$

where r_p is the proper distance and r_0 is the spatial correlation length at z=0. However we need this value in terms of co-moving co-ordinates r_c where $r_c = r_p(1+z)$:

$$\xi(r_c, z) = \left(\frac{r_c}{r_0}\right)^{-\gamma} (1 + z)^{\gamma-(3+\epsilon)}. \tag{4.9}$$

Here ϵ is usually selected to be one of three primary clustering models: ϵ=0 is equivalent to stable clusters of a fixed physical scale, ϵ=γ-3 models clusters of fixed co-moving size and finally ϵ=γ-1 which represents the growth of clustering in linear perturbation theory. The slope of the spatial power spectrum, γ is related to the slope of the measured auto correlation function, as the spatial power spectrum has been shown to project onto the sky as another powerlaw of the form $w(\theta) = A\theta^{1-\gamma}$ (Peebles, 1980), hence

$$\gamma = -b + 1. \tag{4.10}$$

We assume the form of the spatial correlation function in Equation 4.9. The inverted Limber equation for this form is given in (Overzier et al., 2003; Kovač et al., 2007; Kim et al., 2011; Elyiv et al., 2012; Lindsay, 2015) and can be re-arranged to give r_0:

$$r_0 = \left[\frac{c\, A\, [\int_0^\infty p(z)\, dz]^2}{H_0\, H_\gamma\, \int_0^\infty N^2(z)(1+z)^{\gamma-(3+\epsilon)}\, \chi^{1-\gamma}(z)\, E(z)\, dz} \right]^{1/\gamma}, \tag{4.11}$$

where χ(z) is the co-moving distance given by:

$$\chi(z) = \frac{c}{H_0} \int_0^z \frac{dz\prime}{E(z\prime)}, \tag{4.12}$$

where E(z) describes the universe's cosmological expansion history:

$$E(z) = [\Omega_{m,0}(1+z)^3 + \Omega_{k,0}(1+z)^2 + \Omega_{\Lambda,0}]^{\frac{1}{2}}, \tag{4.13}$$

and H_γ is related to the Gamma function (Γ)

$$H_\gamma = \Gamma(\frac{1}{2})\Gamma(\frac{\gamma-1}{2})\Gamma(\frac{\gamma}{2}). \tag{4.14}$$

4.4.2 The Angular Power Spectrum

The second method by which we can calculate the clustering of galaxies on angular scales is by determining the Angular Power Spectrum (C_ℓ). Rather than using pair counts to determine over or under densities compared to a Possionian distribution, C_ℓ represents variations in source surface density (much as we do with a Fourier transform) as the sum of its spherical harmonics (i.e sinusoidal angular density fluctuations of different wavelengths).

The spherical harmonics, $Y_{\ell m}$, are defined as:

$$Y_{\ell m} = \sqrt{\frac{2\ell+1}{4\pi}\frac{(\ell-m)!}{(\ell+m)!}} P_\ell^m(cos\theta) e^{im\phi}, \tag{4.15}$$

where the multipole ℓ = 0,...,∞ is a measure of the angular scale and can be roughly equated to θ by $\ell = \pi/\theta$ (in radians) or by $\ell = 180/\theta$ in degrees, -ℓ < m < ℓ and P_ℓ^m are the Legendre Polynomials.

The surface density of the sky can be represented by applying the co-efficients ($a_{\ell m}$) to the spherical harmonic functions, such that the density at any given point on a sphere can be expressed as:

$$\sigma(\theta, \phi) = \sum_{\ell=0}^{\infty} \sum_{m=-\ell}^{\ell} a_{\ell m} Y_{\ell m}(\theta, \phi). \tag{4.16}$$

To determine $a_{\ell m}$ we integrate the measured density field $\sigma(\theta, \phi)$ scaled by the conjugate of the spherical harmonics across a full sphere.

$$a_{\ell m} = \int_{\theta=0}^{\pi} \int_{\phi=0}^{2\pi} \sigma(\theta, \phi) Y^*_{\ell m}(\theta, \phi) d\Omega. \tag{4.17}$$

The angular power spectrum C_ℓ is defined as the variance in these spherical harmonic coefficients over many realisations of this sampling process. If the assumption of isotropy holds, C_ℓ is a function of ℓ only and can be expressed as:

$$C_\ell =< |a_{\ell m}|^2 > . \tag{4.18}$$

To determine the spherical harmonic coefficients of the observed survey field we may estimate the density field by summing over the N galaxy positions (θi, *phi*i):

$$A_{\ell m} = \sum_{i=1}^{N} Y^*_{\ell m}(\theta_i, \phi_i). \tag{4.19}$$

Since no survey has 100% sky coverage, we need to correct for the effects of a partial sky. Our correction for the partial sky coverage of the survey is performed within our chosen spherical harmonic transform software 'Polspice', (Szapudi et al., 2001) but this operation can be expressed, as in Blake et al. (2004) as:

$$C^{obs}_{\ell m} = \frac{|A_{\ell m} - \sigma_0 I_{\ell m}|^2}{J_{\ell m}} - \sigma_0, \tag{4.20}$$

where σ_0 is the number of unmasked sources divided by the unmasked survey area and

$$I_{\ell m} = \int_{\Delta\Omega} Y^*_{\ell m} d\Omega, \tag{4.21}$$

$$J_{\ell m} = \int_{\Delta\Omega} |Y_{\ell m}|^2 d\Omega. \tag{4.22}$$

Finally, we average Equation 4.20 over all values of m to determine the angular power spectrum

$$C^{obs}_{\ell} = \frac{1}{2\ell + 1} \sum_{m=-\ell}^{\ell} C^{obs}_{\ell m}. \tag{4.23}$$

To measure C_ℓ we make use of two separate software packages for our analysis, Healpy (a python wrapper for HEALPIX, Górski et al., 2005) to construct our galaxy density maps and Polspice (Szapudi et al., 2001) to perform the Spherical Harmonic Transforms.

HEALPIX allows the user to partition a spherical map into exactly equal area quadrilateral pixels of varying shape. The exact number of pixels used to represent the sky surface density is dependant upon the N_{side} value chosen for the analysis, which is the number of divisions (along the side of each of the 12 base-resolution pixels) needed to reach the desired resolution. It is related to the total number of pixels on the sphere by

$$N_{pix} = 12N_{side}^2. \tag{4.24}$$

The number of pixels used in the map sets the maximum multipole value (and hence smallest angular scale) at which the analysis is valid and both programs recommend against any analysis of $\ell > (2N_{side} - 1)$.

In order to maximise the constraining power of a harmonic analysis, it may be tempting to select a N_{side} of extremely high value. Indeed, since both Healpy and Polspice $C(\ell)$ computation times scale proportional to $N_{pix}^{1/2}$ and ℓ_{max}^2, an analysis of extremely large pixel maps may no longer seem to be computationally prohibitive, however the number of sources per pixel must be considered as largely empty sky maps can result in oversampling of the map. Thus we limit our N_{side} to a maximum of 32.

To convert the observations into a HEALPIX source density map we iterate through the entire survey component catalogues, summing the number of components that fall within each pixel to produce the map seen in the top left panel of Figure 4.1. No component to source matching is performed. We mask sources associated with Galactic emission (|b > 5 degrees|) and side-lobes around bright sources using the bright source mask of Blake et al. (2004), (Figure 4.1: Top Right), before normalising the map such that

$$M_i^{normed} = (M_i - \sigma_0)/\sigma_0, \tag{4.25}$$

where M_i is the value of each pixel of index 'i' in the map and σ_0 is defined as the average value of all unmasked pixels,

$$\sigma_0 = \frac{\sum M_i^{unmasked}}{N_{pix}^{unmasked}}. \tag{4.26}$$

This produces a normalised source surface density map of the survey (Figure 4.1: Bottom Left). Finally, due to the known presence of significant power at $\ell > 3(N_{side}\text{-}1)$, the normalised map is not band-width limited and as such needs to be smoothed by a Gaussian kernel with a FWHM on the order of 2 times the pixel scale (Hivon et al., 2016) (Figure 4.1: Bottom Right)

The resultant maps are fed into the PolSpice program. Polspice utilises the isolatitude pixelisation scheme of the Healpix map to the reduce computation time necessary for the determining the power spectrum of large, all-sky thermal or source-density maps. It also applies the necessary partial sky corrections needed for a accurate analysis based upon the mask file provided.

While the corrections for the un-surveyed parts of the sky are applied, partial sky coverage is also known to result in a mixing of the harmonic coefficients, thus making each

measured C_ℓ dependent upon its neighbours. Luckily for large surveys (with a sky coverage fraction, $f_{sky} \approx 0.75$) this effect is small, on the order of 15% and can be neglected due to the smoothness of the radio angular power spectrum and the comparative size of other sources of error (Blake et al., 2004).

There are two primary sources of uncertainty on any measurement of the angular power spectrum. The first of these is 'Cosmic Variance' which derives from the limited cosmic volume which we can sample. Since we only have one universe to observe, this results in a limit to the number of m modes that any survey can sample. 'm' can only be sampled between -ℓ and ℓ and as such we have only (2ℓ+1) samples of m, for any given multipole (Blake et al., 2004),

$$C_\ell^{obs} = \frac{1}{2\ell+1} \sum_{m=-\ell}^{\ell} |a_{\ell m}|^2. \tag{4.27}$$

Furthermore the density field is real and thus $C_{\ell m} = C_{\ell -m}$, resulting in only $\ell + 1$ independent measurements.

$$C_\ell^{obs} = \frac{1}{\ell+1} \sum_{m=0}^{\ell} C_{\ell m}^{obs} \tag{4.28}$$

As a result of this there is a fundamental error of $\Delta C_\ell = \sqrt{1/\ell+1}$ associated with any C_ℓ measurement. Combining this with the second major source of error, shot noise, and our sky coverage fraction, the final errors on our angular power spectrum can be calculated using Equation 4.29

$$\sigma(C_\ell^{obs}) = \left(\frac{1}{\sigma_0} + C_\ell\right) \frac{\sqrt{\ell+1}}{\ell+2} \frac{1}{f_{sky}} \tag{4.29}$$

Finally we fit a single power law to our observed data such that $C(\ell) = A\ell^b$.

4.5 Analysis

4.5.1 NVSS

To check the implementation of our methodology we begin by attempting to reproduce the results of the Blake & Wall (2002a) analysis of the NRAO VLA Sky Survey (NVSS) auto correlation function and angular power spectrum. While advanced analyses using specially crafted masks have been performed elsewhere (see Overzier et al. (2003); Chen & Schwarz (2016)), the primary purpose of this section is to check the implementation of our auto-correlation function and angular power spectrum codes and the reproducibility of previous work. Hence for all analysis of the NVSS we mask all sources within 5 degrees of the galactic plane. Along with selected areas around bright extended sources (See Appendix C).

Overall we find reasonable agreement between our NVSS correlation function and previous studies on both small and large angular scales (Figure 4.2). However there are some slight discrepancies that are worth noting. In the top panel of Figure 4.2 we can see that at scales above 0.1deg (i.e scales dominated by the clustering of radio galaxies) our calculated amplitude is above the Blake et al measurement of $(1.12 \pm 0.12) \times 10^{-3}$. Even if we

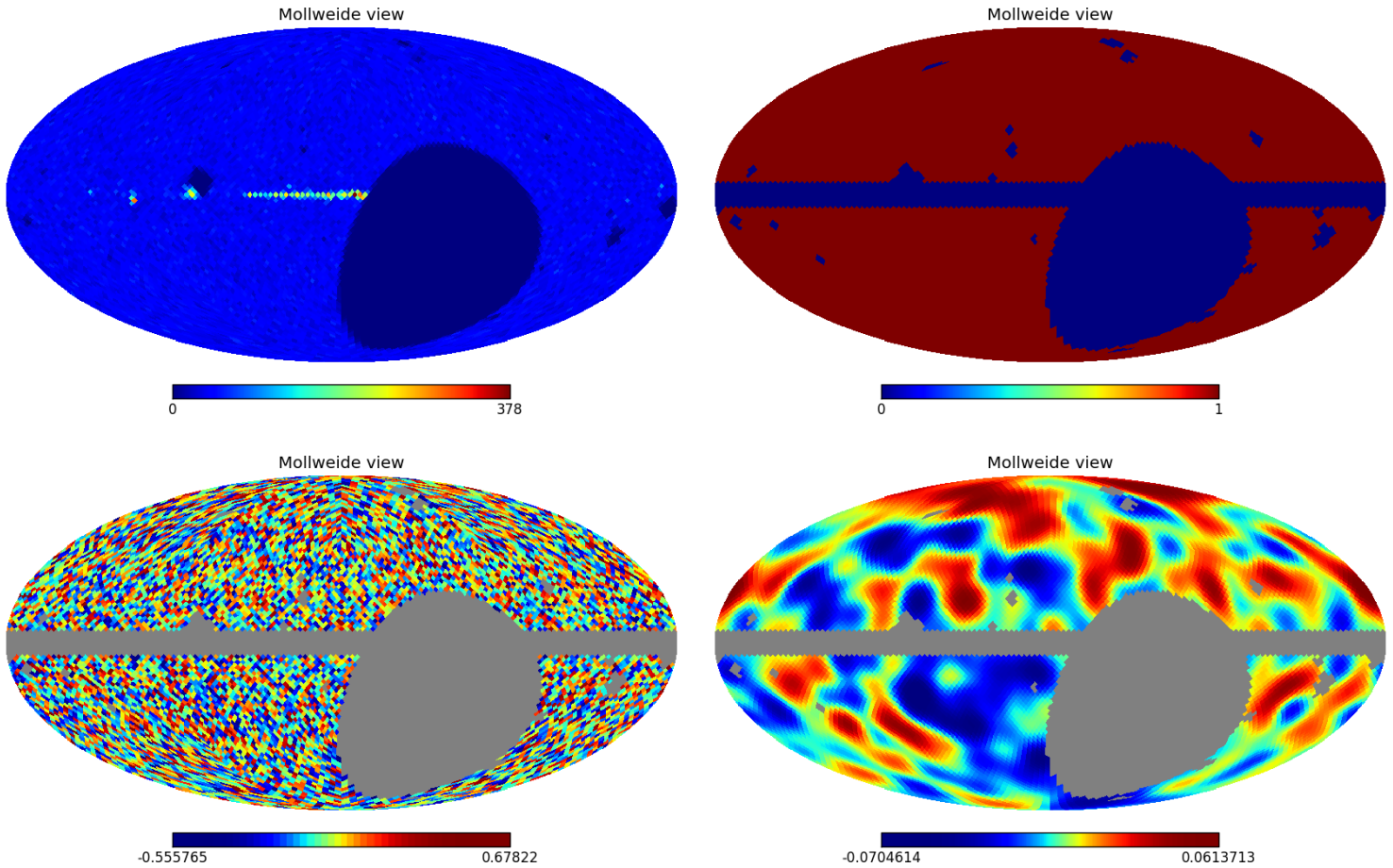

Figure 4.1: Top Left: A Healpix density map of NVSS using a N_{side} of 32 in a Mollwiede Galactic projection. Top Right: The applied sky mask, based on the location and extent of large extended sources along with a region ± 5 degrees of the galactic plane, same projection and N_{side}. Bottom Left: The resultant masked anisotropy map after applying the sky mask and subtracting and dividing out the average masked source surface density. Bottom Right: The masked anisotropy map after smoothing with a Gaussian such that there is 3 pixels per the Gaussian beam.

constrain our fitted slopes to match their analysis to -0.8 and -3.4 for the clustering and size power-laws respectively, we still determine a clustering amplitude of $(1.6 \pm 0.1) \times 10^{-3}$. At scales well known to be dominated by extended sources however (i.e. $\theta < 0.1$ deg) we are in excellent agreement with previous results. Inverting these measurements using the Limber Inversion, assuming a redshift distribution taken from the SKADS Semi Empirical Extra Galactic Simulation cut at 15 mJy, we determine a spatial correlation length $r_0^{\epsilon=0}$ of 5.5±0.2 h^{-1} Mpc. Naively this is slightly above the quoted equivalent Blake et al measurement of 5.1 ± 0.2. Importantly however Blake et al use a different p(z) distribution to us for the Limber Inversion. Correcting for this by using their fitted parameters (A = $1.12 \pm 0.12 \times 10^{-3}$, b=-0.8) with our assumed p(z) distribution from SKADS, results in a update Blake et al measurement of $r_0^{\epsilon=0} = 6.3^{+0.4}_{-0.4}\ h^{-1}$ Mpc. Hence we find a slightly shorter spatial correlation length than previous studies.

In the bottom panel of Figure 4.2 we show the angular power spectrum calculated using Polspice on a Healpix over/under density map of the NVSS, smoothed using a FWHM of 2 times the pixel scale. We appear to have excellent agreement with previous work, However, in Blake & Wall (2002a) a constant vertical offset (caused by extended sources) of $\Delta C_\ell = 2.4 \times 10^{-5}$ was discovered and corrected for. Despite the fact that the effect should be equal in our own analysis we find no indication that this correction is required. Further investigation into the exact method by which ΔC_ℓ is calculated leads to some confusion. Blake et al derive ΔC_ℓ to be equal to:

$$\Delta C_\ell = 2e\sigma_0 \tag{4.30}$$

where e, the fraction of radio galaxies with multiple components for a given flux limit, is deduced (and explicitly stated) as e = 0.07±0.05 and σ_0 is derived and stated as the source surface density ($N/\Delta\Omega$) which equals 16.9 deg^{-2} and 9.5 deg^{-2} at 10mJy and 20mJy respectively. Using these values we cannot to reproduce the stated ΔC_ℓ of 2.4×10^{-5}. The closest equation that gives the quoted ΔC_ℓ value is

$$\Delta C_\ell = 2e\sigma_0^{-1} \tag{4.31}$$

with σ_0 in units of sources per steradians. While this may be a typographical error in Blake & Wall (2002a) the change suggested here would not match the derivation used for the expected effects of two component sources. Given the lack of apparent offset in our Polspice analysis, the confusion in the offset correction and the relatively small scale of the stated effect, we choose here not to apply a correction to our Polspice calculated power spectrum. Despite this issue, we find good agreement between our analysis of the angular power spectrum of NVSS and previous work.

4.5.2 JVLA Stripe-82

In the top panel of Figure 4.3 we show the auto correlation function for the JVLA Stripe-82 observations. At scales below 0.1 degrees (dominated by extended structures in NVSS) the 246μJy ACF possesses a much smaller amplitude and shallower slope ($A = 1.6 \pm 0.4 \times 10^{-5}$) than the equivalent NVSS fit, consistent with the increased fraction of star-formation driven radio sources at μJy levels resulting in a lower fraction of extended two component radio

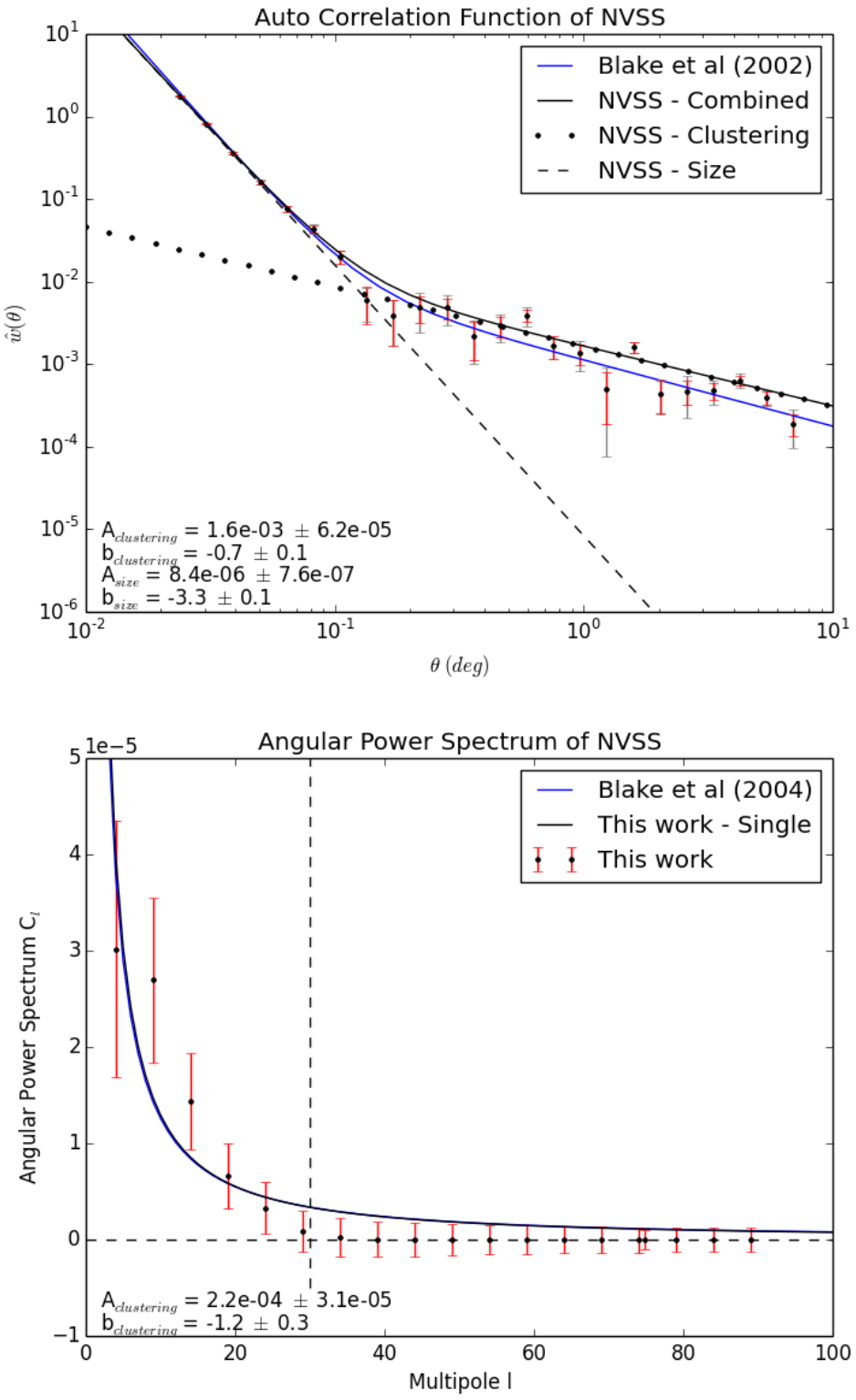

Figure 4.2: Top: The auto correlation function of the NVSS survey at 15mJy (black points with Poisson errors in red) alongside the Blake & Wall (2002a) fit to NVSS for reference (blue line). Bottom: The Angular Power Spectrum for the NVSS survey, is fitted at $\ell <$ 30 where power is detected, alongside the Blake et al. (2004) fit to NVSS (all color coded as above). Overall we find excellent agreement with the analysis of Blake & Wall (2002a); Blake et al. (2004); Chen & Schwarz (2016).

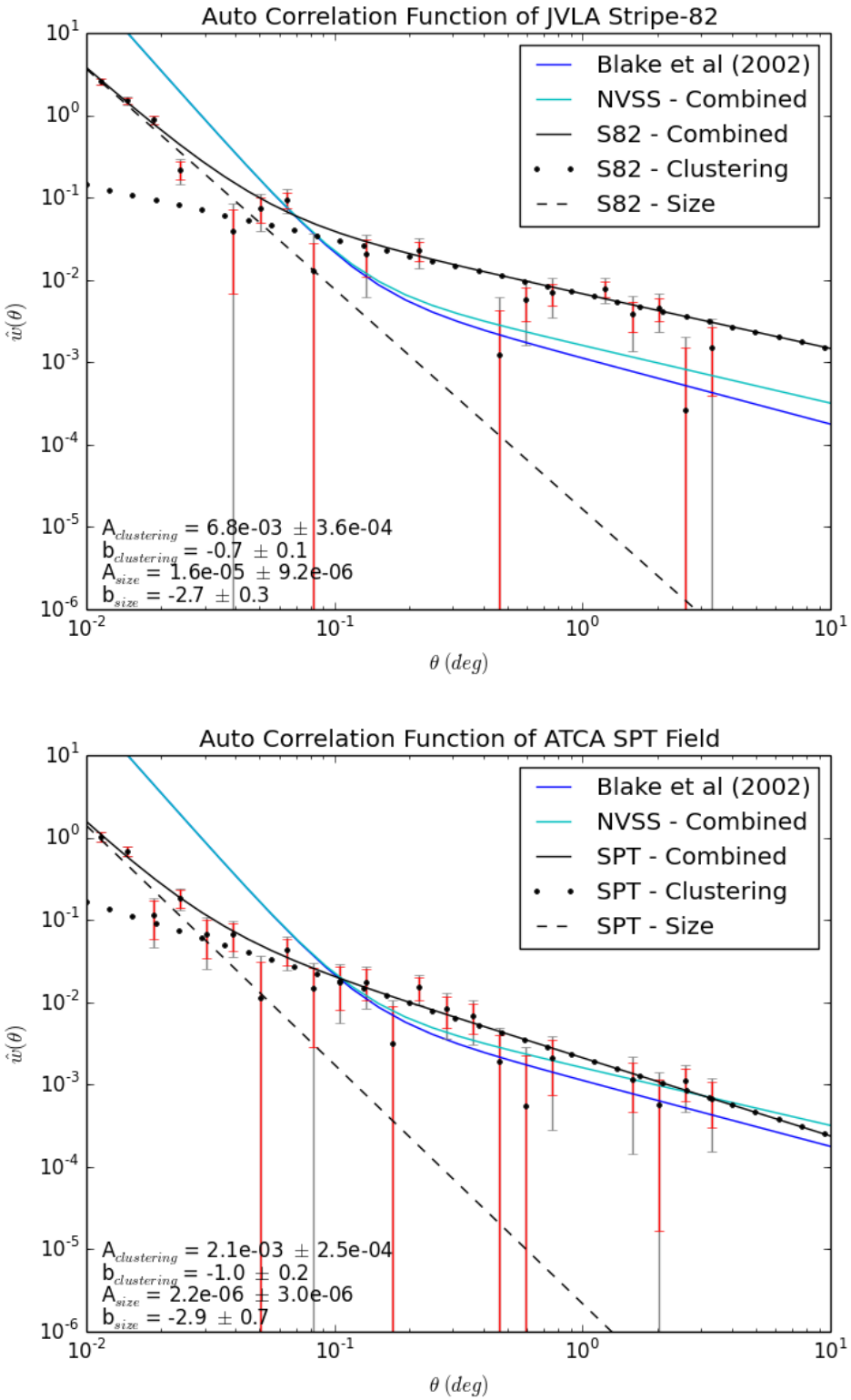

Figure 4.3: Top: The auto correlation function from a central 26 square degree patch of 88μJy JVLA Stripe-82 Eastern field (black points with Poisson and bootstrap errors shown as red and grey errorbars respectively). The displayed data is the mean of 1000 bootstrap samples. Only sources above 246μJy (3 sigma) are considered. A sum of two power-laws is fitted (black dots and dashes) alongside the Blake et al. (2004) fit to NVSS for reference (blue line). Bottom: The Auto Correlation Function from the central 89.0 square degree area of the ATLAS SPT field color-coded as before. Only sources above 300μJy (3 sigma) are considered.

sources. From the best fit of two power-laws we measure the clustering dominated power (θ > 0.1 degrees) to be best fit by a slope b = -0.7 ± 0.1 with a amplitude A = (6.9 ± 0.8) × 10^{-3} and find that this measurement does not change when fitting a single component power-law to scales greater than 0.1 degree only. Inverting these measurements using the Limber Inversion assuming a redshift distribution for p(z) taken from the SKADS Semi Empirical Extra Galactic Simulation cut at 246μJy we determine the spatial correlation length $r_0^{\epsilon=0}$ = (10.1 ± 0.7) h^{-1} Mpc. This is unreasonably strong clustering for radio-galaxies and is most likely due to the poor quality data and subsequent fit of the S82 observations.

4.5.3 ATLAS SPT

In the bottom panel of Figure 4.3 we show the auto correlation function for the ATLAS observations of the SPT field. With a measured clustering slope of -1.0 ± 0.2 and a clustering amplitude of 2.1 ± 0.4 × 10^{-3} the SPT correlation function appears to be consistent within 3 sigma of the NVSS fit but significantly offset from the best fit values of S82 (Table 4.1). We determine the spatial correlation length for the SPT survey to be $r_0^{\epsilon=0}$ = (12.2 ± 0.9) h^{-1} Mpc, using the SKADS p(z) for S > 300μJy sources. The spatial correlation length as a function of ϵ is given in Table 4.1.

4.6 Empirically modelling the μJy Auto Correlation Function

In this section we attempt to produce predicted Auto Correlation Functions for the μJy radio continuum sky using the empirical relations linking radio-AGN and radio star-forming activity to galaxy stellar-mass and star-formation rates discovered in Chapter 2.

Our Semi-Empirical model begins at the Theoretical Astrophysical Observatory (Bernyk et al., 2016) where we request the Millennium Simulation with an initial cosmology taken from WMAP-1 (Ω_m = 0.25, Ω_Λ = 0.705, Ω_b = 0.045, σ_8 = 0.9, h = 0.73, n = 1). This is then processed using the Semi Analytical Galaxy Evolution (SAGE Croton et al., 2016) software to produce a simulated catalogue of galaxies based on the Millennium simulation's underlying dark matter halos. Finally we take a single random light-cone through this simulation using the TAOs built in light-cone generator and request a stellar-mass-selected sample of all galaxies above 10^9 $M_\odot$ in a 10 × 10 degree field of view. Due to the computational requirements of such a large area we are forced to limit the simulation to cosmological redshifts of z < 2.0, though in practice the maximum 'observed' redshift returned by the simulation is slightly higher due to peculiar motion.

The resulting catalogue contains a full suit of galaxy and black hole properties along with predicted optical to infrared Skymapper (UVGIRZ), Spitzer (24μm) and PACs (70μm, 100μm, 160μm) fluxes for the 23 million galaxies in our simulation. This however is a stellar-mass-selected sample and thus not a fair comparison to our radio-selected ATLAS-SPT observations. To address this issue we now 'radioize' the simulations using a set of known empirical relations.

Table 4.1: Summary of the ACF best fit parameters for the three surveys and model. Note: As is standard practise, errors on all r_0 values assume the quoted measured value of γ. Accounting for errors in γ greatly increases the associate r_0 errors, by a factor of ≈ 4.0. Blake - Original refers to the Blake 2002 quoted fit parameters and correlation lengths. Blake - Remapped are the Blake & Wall (2002a) parameters projected to correlation length using the same p(z) distribution as our work.

Survey	Flux Limit	A_{size} ($\times 10^{-5}$)	b_{size}	A_{clust}($\times 10^{-3}$)	b_{clust}	Z_{mid}	$r_0^{\epsilon=0}$	$r_0^{\epsilon=\gamma-1}$	$r_0^{\epsilon=\gamma-3}$	χ^2_{red}
Blake - Original	15 mJy	0.58 ± 0.03	-3.4	1.12 ± 0.12	-0.8	-	$5.1^{+0.2}_{-0.2}$	$7.1^{+0.3}_{-0.3}$	$3.6^{+0.1}_{-0.1}$	1.78
Blake - Remapped	15 mJy				1.31	$5.4^{+0.2}_{-0.2}$	$7.1^{+0.3}_{-0.3}$	$3.1^{+0.1}_{-0.1}$	1.78	
NVSS	15 mJy	0.8 ± 0.1	-3.3 ± 0.1	1.6 ± 0.1	-0.7 ± 0.1	1.31	$5.5^{+0.2}_{-0.2}$	$6.1^{+0.3}_{-0.3}$	$3.3^{+0.1}_{-0.1}$	3.45
S82-East	246 μJy	1.6 ± 0.4	-2.7 ± 0.7	6.9 ± 0.8	-0.7 ± 0.1	1.08	$10.1^{+0.7}_{-0.7}$	$12.3^{+0.8}_{-0.9}$	$6.6^{+0.4}_{-0.5}$	2.20
SPT	300 μJy	0.2 ± 0.3	-2.9 ± 0.7	2.1 ± 0.3	-1.0 ± 0.2	1.08	$12.2^{+0.8}_{-0.9}$	$15.1^{+1.0}_{-1.1}$	$9.4^{+0.6}_{-0.7}$	1.54
SPT != 0.2-0.3 degrees	300 μJy	1.4 ± 1.4	-2.5 ± 0.5	1.6 ± 0.2	-0.8 ± 0.3	1.08	$2.2^{+3.4}_{-1.7}$	$2.5^{+4.6}_{-1.9}$	$1.7^{+3.1}_{-1.3}$	1.44
SPT-Model	300 μJy	-	-	1.2 ± 0.3	-1.0 ± 0.3	1.08	$9.2^{+1.1}_{-1.2}$	$11.4^{+1.3}_{-1.5}$	$7.1^{+0.8}_{-1.0}$	0.99

The extragalactic radio sky at 1.4 GHz is dominated by synchrotron emission from star-forming galaxies and AGN. To recreate this effect we first produce a baseline radio-luminosity for each galaxy due to star-formation rate (SFR). This is done by numerically inverting the Bell (2002) radio-luminosity to star-formation rate relation (Equation 4.32).

$$\psi(M_{\odot}\mathrm{yr}^{-1}) = \begin{cases} 5.52\times10^{-22}L_{1.4\,\mathrm{GHz}} & L > L_c \\ \frac{5.52\times10^{-22}}{0.1+0.9(L/L_c)^{0.3}}L_{1.4\,\mathrm{GHz}} & L \leq L_c, \end{cases} \tag{4.32}$$

where $L_c = 6.4\times10^{21}$, W Hz^{-1} is the radio luminosity at 1.4 GHz of a $\sim L_*$ galaxy ($V = -21$, or $L_{\mathrm{TIR}} \sim 2\times10^{10}L_{\odot}$).

If the simulated galaxy star-formation rate is lower than 0.025 M$_{\odot}$ yr^{-1} then the galaxy falls below the minimum luminosity possible in the Bell relation (1×10^{19} W Hz) and is assigned a radio luminosity of zero. It is not at this point removed from the output catalogues as it may yet be allocated some luminosity from radio-AGN activity.

Next we choose which of our simulated galaxies are going to host some level of radio-loud AGN activity. This is done by utilising the well known relation between stellar-mass and radio-loud AGN fraction (Best et al., 2005) which shows little evolution across the redshift range we are probing (Rees et al., 2016). A log linear fit is performed on the correlation found in (Rees et al., 2016) and used to weight the likelihood of each simulated galaxy containing a radio-AGN by its stellar-mass (Equation 4.33)

$$AGN_{Frac} = 10^{1.378\times M-16.964}, \tag{4.33}$$

where M is the host galaxies stellar-mass (M$_{\odot}$). For each galaxy a random number is generated between 0 and 1. If the generated number is less than the AGN fraction for that galaxies stellar-mass, then that galaxy is assigned as a radio-AGN host. We note that while the total number of simulated radio-AGN in our galaxy population is extremely sensitive to changes in this relation, the correlation function itself is remarkably insensitive to these variations.

Finally we assign each radio-AGN a luminosity based on the best fit of the local radio-loud AGN luminosity function of Mauch & Sadler (2007). The broken power-law of this luminosity function is as detailed in Equation 4.34

$$\Phi(P) = \frac{C}{(P/P^{\alpha}_{\star)} + (P/P^{\beta}_{\star)}}, \tag{4.34}$$

where C=$10^{-5.50\pm0.25}$ mag^{-1} Mpc^{-3}, P$_{\star}$=$10^{24.59\pm0.30}$ W Hz^{-1}, α=1.27 $\pm$ 0.18 and β=0.49 $\pm$ 0.04.

While this radio-AGN luminosity function is constrained between $1\times10^{20-26}$ WHz^{-1} the radio-AGN fraction is based only on AGN above 1×10^{24} WHz^{-1}. Hence we limit our radio-AGN luminosity function to sources above 1×10^{24} WHz^{-1} in order to match this constraint. This leads to an absence of low power (potentially radio-quiet) radio-AGN sources at low redshifts (z<1) and as such we note that because of this our simulation may under estimate power on large angular scales.

In addition to the above caveat, we must also consider that in the higher redshift universe radio-AGN become more powerful and hence the shape of their luminosity function may evolve. However, the luminosity threshold of an SPT-like survey at 4 sigma is already greater than $1{\times}10^{24}$ WHz^{-1} at z≈1. Since our AGN are limited to $1{\times}10^{24}$ WHz^{-1} and up, the radio-loud-AGN luminosity function actually has less impact on the simulation than might be expected.

Our last step is to 'observe' our radio sky. To do this we sum each galaxy's star-formation and AGN-driven radio luminosity and use the redshifts from the simulation to convert each galaxy's radio luminosity to radio flux, assuming an average spectral index of α = -0.7, where $S = \nu^{+\alpha}$. We then apply a flux cut, 3 sigma above the sensitivity of the real ATLAS-SPT observations (i.e $S > 300\mu Jy$). The resultant simulated catalogue contains 10453 sources of which 78.6 ± 0.4 % are AGN and 21.4 ± 0.4 % radio detected star-forming galaxies, in good agreement with what is expected from ATLAS-SPT and other similar fields.

Figure 4.4 shows the auto correlation function for our simulated radio sky along with its best fit single power law ($w(\theta) = a\theta^b$) of a = 1.2 ± 0.3 × 10^{-3}, b = -1.0 ± 0.3 which was fitted to the same angular scales as the observed data (0.01-10 degrees). We can clearly see a lack of extended source structure at scales smaller than 0.1 degrees (as no extended sources were placed in this simulation) but in general we have good agreement within errors at larger scales for both the amplitude and slope of the power law fit.

4.7 Numerical Cosmological Models

To compare our results to those predicted from theory we generate theoretical angular correlation functions using CAMB (the Code for Anisotropies in the Microwave Background). CAMB uses numerical models to produce the Spatial Power Spectrum, P(k) of dark matter halos in a universe with the specified cosmological parameters. This spatial power spectrum can then be sampled using theoretical radio-galaxy bias functions, b(z) and redshift distributions p(z), to produce the expected angular power spectrum of radio galaxies, C_ℓ. We note that these simulations are completely separate and distinct from the empirical simulations in the previous section.

$$C_\ell = \frac{2}{\pi}\int_0^\infty W_\ell(k)^2 P(k) k^2 dk, \tag{4.35}$$

where P(k) is the spatial power spectrum output by CAMB and $W_\ell(k)$ is the window function:

$$W_\ell(k) = \int_0^\infty j_\ell(kr) b(z) \frac{dp(z)}{dz} dr, \tag{4.36}$$

where j_ℓ is a Spherical Bessel Function, b(z) is a dimensionless bias of order unity and p(z) is the probability distribution of galaxies normalised such that

$$\int_0^\infty p(z) dz = 1. \tag{4.37}$$

For computational efficiency at large values of ℓ ($\ell > 100$) we use the Limber approximation of the Spherical Bessel Function such that

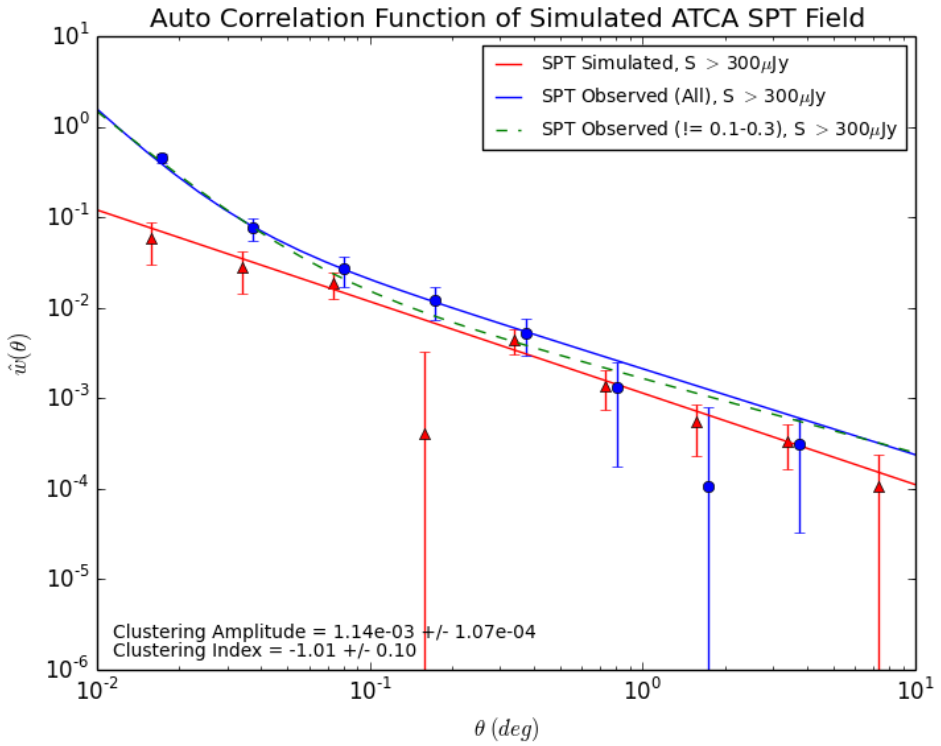

Figure 4.4: The simulated auto correlation function for the ATLAS SPT survey with bootstrapped errors (red triangles), fitted using a single power law (red line) alongside the observed SPT auto correlation function (blue circles), fitted using a double power law (blue line). Note the observed data points have been rebinned and shifted rightward by 10% for clarity.

$$W_\ell(k) \approx \frac{1}{\ell} f(\ell/k)^2 b(z) \frac{dp(z)}{dz} \tag{4.38}$$

Converting the Angular Power Spectrum C(ℓ) to a Angular Correlation function, $\omega(\theta)$ is then possible using Equation 4.39,

$$\omega(\theta) = \frac{1}{4\pi} \sum_0^\infty (2\ell + 1) C_\ell P_\ell(cos\theta) \tag{4.39}$$

where P_ℓ is the Legendre Polynomial, to sum the power contribution of each physical scale (k) to each angular scale (ℓ) across all spatial scales and distances.

For all of our fits we use p(z) distributions taken from the Wilman et al. (2008) SKA Design Studies Semi-Empirical Extra-Galactic Simulation (SKADS). To determine the p(z) we begin by cutting the simulations at our observed flux limits. We then sum the number of each type of galaxy (Star-forming Galaxy, Star-Burst Galaxy, Radio-Quiet Quasar, Fanaroff-Riley Type I, Fanaroff-Riley Type II, Seyfert I and Seyfert II) per redshift bin. The final p(z) used in all calculations is a interpolation of this combined p(z). The bias used in our simulations is a bias of b = 1.7 for NVSS (Blake et al., 2004) and b = 2.13 for the 300uJy SPT population, which is taken from the work of Lindsay (2015) which measures this bias

for S > 90uJy radio sources. The resultant predicted auto correlation function for a LCDM universe as viewed be the NVSS, and SPT surveys is shown in Figure 4.5.

4.8 Discussion

In the above sections we have measured and modelled the auto correlation function and angular power spectrum of the NVSS survey, along with two deep fields observed with the ATCA (SPT) and JVLA (Stripe 82).

We find the measured amplitude and slope of the NVSS correlation function at scales, θ < 10 degrees to be in good agreement with previous studies and LCDM, albeit with a slightly higher amplitude at $\theta > 0.1$ degrees than expected. Our analysis of the NVSS angular power spectrum is in excellent agreement with previous work (Blake et al., 2004; Chen & Schwarz, 2016).

We find that the JVLA Stripe-82 observations shows a significantly elevated clustering amplitude in the correlation function when fitted to the full available data set compared to the ATLAS-SPT observations. We attribute this to the elongated shape of the S82 field which severely limits the number of possible correlations on large scales in one direction, the low number of sources in such a small survey area, and the minor but not insignificant, sensitivity variation across the field caused by lost observing time. The last of these effects could possibly be mitigated by analysing only sources whose signal to noise ratio is greater than 5 or even 10 and could easily result in the removal of excess power at 0.1-0.2 degrees (the size of the telescope FOV) and at scales ≈1 degree which corresponds to scale of individual tiles in the mosaic. Unfortunately, due to a variety of observational reasons, this field already covers a much smaller area than originally planned, and as such, a move to higher signal to noise sources would decrease the number of galaxies beyond the point at which a meaningful analysis can be made. This emphasises the importance of survey uniformity for the EMU observations, as a great deal of the predicted cosmological sensitivity of such a survey may be lost if significant sensitivity variation limits any analysis to a very high S/N regime.

In contrast to the issues we find while using JVLA STRIPE-82, our SPT observations are of sufficient quality to allow meaningful analysis.

We find that in contrast to NVSS a singular power-law can be used to represent the data down to $\theta \approx 0.05$. This is primarily due to the low fraction of resolved sources in the SPT correlation function compared to NVSS.

It is apparent however that SPT (like STRIPE-82) shows an elevated clustering amplitude compared to NVSS. While this is well below the elevation seen in S82 it nonetheless results in a measured spatial correlation length (for 300μJy sources) that does not follow the trend seen in Overzier et al. (2003) towards decreasing spatial correlation length with flux. We have extensively tested our script to perform the Limber Inversion and note that it successfully reproduces the spatial correlation lengths of Blake & Wall (2002a), Overzier et al. (2003) and Lindsay (2015) when using their fitted parameters and assumptions and hence can rule out our inversion script as the cause of this discrepancy.

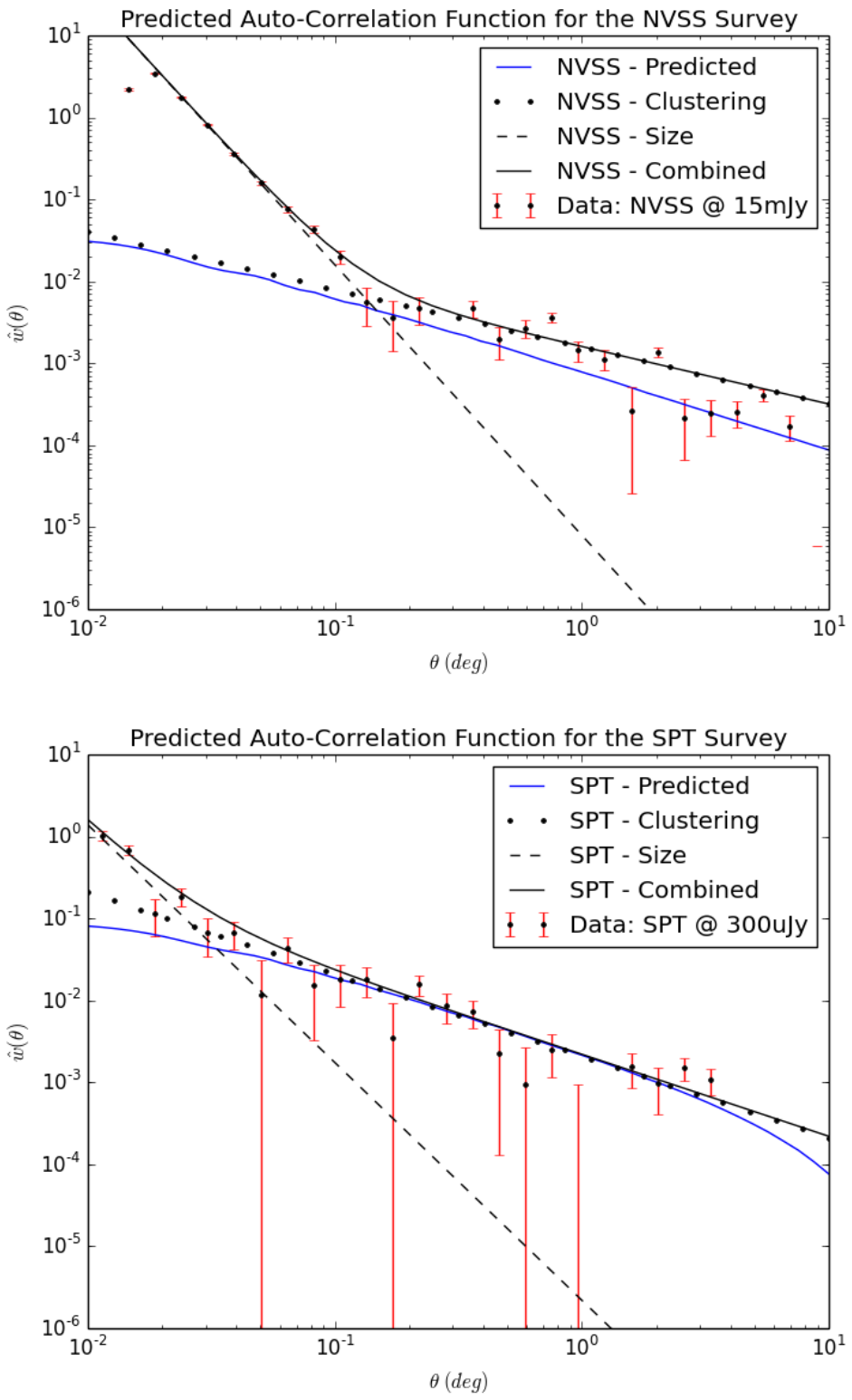

Figure 4.5: Top: The numerically simulated auto correlation function for a NVSS-like survey (blue line), alongside the observed ATLAS-SPT auto correlation function (black circles with red errorbars). Bottom: The same but for ATLAS-SPT.

Investigating the cause of this elevation it becomes apparent that an excess of power on scales of 0.1-0.3 degrees may be driving our fitting process, resulting in a poor fit and elevating our fitted amplitude (Figure 4.3: Bottom). Removing the three elevated data points in the SPT auto-correlation function between 0.2 and 0.3 degrees results in a better fit to the data and yields a lower amplitude and slope of A = (1.6 ± 0.24) × 10^{-3}, γ = 1.8 ± 0.3 and a $r_0^{\epsilon=0} = 2.2^{+3.4}_{-1.7}$ h^{-1} Mpc. This is in much better agreement with the observed relation between flux and correlation length at milli-Jansky levels, as well as the correlation length of 90μJy sources (Lindsay, 2015) of r_0 = 2-5 h^{-1} Mpc. Interestingly, a similar 'bump' in the correlation function at these scales was found in (Overzier et al., 2003), albeit for much brighter sources (S > 200mJy).

Given the complex nature of the radio sky, it may be somewhat surprising that our empirical radio version of the Millennium Simulation was able to reasonably reproduce the radio galaxy auto correlation function. However, given that the empirical relations chosen are well established and using them by definition selects a very similar population of galaxies to a radio selected sample, the primary source of error (if any) would likely have come from the SAGE software's dark matter to Galaxy population modelling. Given the size of the errorbars on current observations in relation to the amount of change expected in any cosmological properties, both our chosen relations and the SAGE modelling software has a substantial degree of lee-way. Nevertheless such good agreement is encouraging and while the current model is at its limits in terms of volume (it's not possible to fit much more than a 10 × 10 degree light-cone through the Millennium simulation) it would be interesting to see further refinements to this technique and some of these are outlined in Chapter5.

Finally while fitting cosmological models with a high number of variable parameters is (for now) still meaningless given the large errorbars associated with all existing radio surveys, our numerically modelled WMAP-1 LCDM correlation function (Figure 4.4), which assumes a constant linear bias of 1.89 for NVSS and 2.13 for SPT/S82, shows reasonable agreement with our observations. In the future, using these models and assuming a LCDM cosmology we hope to better constrain the radio galaxy bias as a function of redshift.

Interestingly we find that the NVSS prediction is somewhat low compared to our observed auto correlation function and appears to be in slightly better agreement with the fit of Blake & Wall (2002a). Our SPT predicted auto correlation function shows a drop off at either end of the plotted region. While the small angle scales are difficult to truly probe given the issues of source to component matching, it is possible that the drop off seen here is caused here by the SKADS redshift distribution, which is known to be poorly constrained for faint sources. Nevertheless, the rough general agreement between observations, numerical and empirical models is encouraging and in future observations, with extremely large source counts over significant fractions of the sky (such as Early-EMU and EMU-Full), it is hoped that fitting to these models will allow for the accurate recovery of a wide range of cosmological parameters.

4.9 Conclusions

Using two new surveys (ATLAS-SPT and JVLA observations of Stripe-82), of similar sensitivity to the upcoming all-sky EMU survey, we have measured the auto correlation function

of radio sources at unprecedented depths for scales of up to 10 degrees.

1. We measure the auto correlation functions of the JVLA and ATLAS-SPT observations at 240μJy and 300μJy. Both surveys yield a much higher correlation amplitude than expected based on previous results at higher fluxes. For the JVLA observations this is likely the result of a very small elongated survey area along with varying source surface density. For the ATLAS-SPT observations the elevated correlation function amplitude is driven by excess power at scales of 0.2-0.3 degrees. Removing these scales from our analysis we find good agreement with previous work and convert the best fit amplitude and slope to determine a spatial correlation length $r_0^{\epsilon=0} = 2.2^{+3.4}_{-1.7}$ h^{-1} Mpc.

2. We measure the NVSS auto correlation function (A = (1.6 ± 0.1) × 10^{-3}, γ = 1.7 ± 0.1) and angular power spectrum (A = (2.19 ± 0.3) × 10^{-4} , index = -1.23 ± 0.06) finding them in good agreement with previously reported results.

3. We design a method for empirically converting galaxy catalogues from semi-analytic simulations into the radio regime and test this technique using the Millennium Simulation. We find that the resultant radio auto correlation function agrees moderately well with the clustering of real sources.

4. Finally we numerically model the expected auto correlation function for a variety of surveys assuming a redshift and bias function from the SKADS extragalactic semi-empirical simulation, finding that the LCDM version of these models shows good agreement with the measured values despite the large errors associated with such small fields.

This research makes use of the Theoretical Astrophysical Observatory (TAO). TAO is part of the All-Sky Virtual Observatory (ASVO) and is funded and supported by Astronomy Australia Limited, Swinburne University of Technology and the Australian Government. The latter is provided through the Commonwealth's Education Investment Fund and National Collaborative Research Infrastructure Strategy, particularly the National eResearch Collaboration Tools and Resources (NeCTAR) and the Australian National Data Service Projects.

"It is well known that a vital ingredient of success is not knowing that what you're attempting can't be done"

Terry Pratchett

5 Future Work

While we have made good progress in both measuring and modelling clustering in the radio sky, this thesis is part of a much larger endeavour to produce high-quality cosmological constraints from of the next generation of radio continuum surveys. As such this chapter outlines the future work needed to reach that goal and provides the first documentation on the proposed Early EMU Cosmology (EEC) field, a project that I have had a significant input in designing.

I first outline improvements that can be made to our process for converting semi-analytic cosmology simulations into a radio cosmology simulation, before detailing the ongoing plan for a Early EMU Cosmology (EEC) field, which will be carried out as part of the ASKAP 12-antenna commissioning phase. The combined size and depth of EEC survey will allow us to truly test the cosmological competitiveness of EMU for the first time. Not only will the EEC operate on the brand new ASKAP array (and hence contain similar issues to what the final EMU survey may face) but also it may finally allow radio surveys to place competitive constraints on the properties of Dark Matter, Dark Energy and Modified gravity theories.

5.1 Simulating the radio sky using empirical relations

This final section contains a number of possible refinements to our empirical radio simulation. The first of these is the acquisition and application of more accurate AGN fractions and luminosity functions from the next generation of deep optical and near infrared surveys. Ideally with sufficient numbers we could constrain the AGN fraction as a function of luminosity, redshift and host type thereby minimizing the current method's sensitivity to changes in the AGN fraction, which can drastically change the number of radio sources simulated. In addition to this, an extension of the AGN fraction relation to higher redshifts is an important next step. A great deal of the cosmological constraining power of radio surveys comes from their high average redshift and limiting our simulation to a redshift of z=2.0 will have a negative impact on our ability to accurately reproduce the expected results of our other probes. In particular the Cosmic Magnification will be most heavily effected by this constraint as a

lack of high-z radio sources will diminish the 'background' sample required for this test.

The limits of our AGN fraction relation are not the only reason we limit our simulation to z=2. This is maximum redshift is also imposed by two separate computational constraints. The first of these limitations, is simply reaching the computational limits set by the TAO. This of course can be mitigated by the acquisition of dedicated super computer time. However the requirements of running SAGE increases drastically with greater redshift ranges and hence the CPU power required to extend this application further will be large. The second of our computational constraints is more problematic, by extending the redshift range or area of our simulated sky we will soon reach the volume limit of the Millennium Simulation. Because of this a much larger N-Body simulation is required in order to produce these simulations on scales similar to even the Early EMU Cosmology field. In the long term, we aim to apply these techniques to larger simulations, such as the Millenium XXL or MICE cosmology simulations

Finally we note that certain improvements can be made to the final 'observing' process of simulation. For example observational artefacts such as side-lobes, beam resolution and noise can be introduced and this will present the opportunity to test the impact of varying sensitivity across the field in a controlled environment.

5.2 The Early-EMU Cosmology Survey

We here outline the ongoing plan for a Early EMU Cosmology (EEC) field, which will be carried out as part of the ASKAP 12-antenna commissioning phase. The EEC survey will be used to create angular auto correlation functions of radio sources in late 2017 at multiple redshifts, cross-correlations of high redshift radio galaxies with low redshift optical counterparts and finally, the cross-correlation of radio galaxies with the CMB. As such it will provide not only a ideal test-bed for unexpected artefacts and issues in Phased Array Feed observations but a substantial radio galaxy population for both cosmological and galaxy evolution studies.

5.2.1 Primary Data

With the ASKAP 12-antenna system now entering its commissioning phase, there is an opportunity to acquire observations of a similar sensitivity to those analysed in this Thesis, but over a far larger area. As part of the ASKAP early science drive, the EMU team has proposed a 2100 square degree Early-EMU Cosmology (EEC) field to be observed down to a depth of 100μJy RMS. The field will be centred on RA=02:30:00 and DEC=-52:30:00 and consist of 60 pointings covering a RA range of 0 < RA < 5 and -65 < DEC < -25. Observations will total 200 hours of the 720 potentially available for early science and assuming the baseline configuration plan of 2016, the final angular resolution will be approximately 13-15$''$ at 1.4 GHz. The substantial area and depth of the proposed field places it in a previously unstudied region of the size/depth parameter space (Figure 5.1), and combined with its use of the actual ASKAP array data this project will be an invaluable step in preparing for many aspects of the full EMU survey. Finally the field has been selected to make use of the wealth of high quality optical and CMB data available in this region, thereby enabling the use of each of the

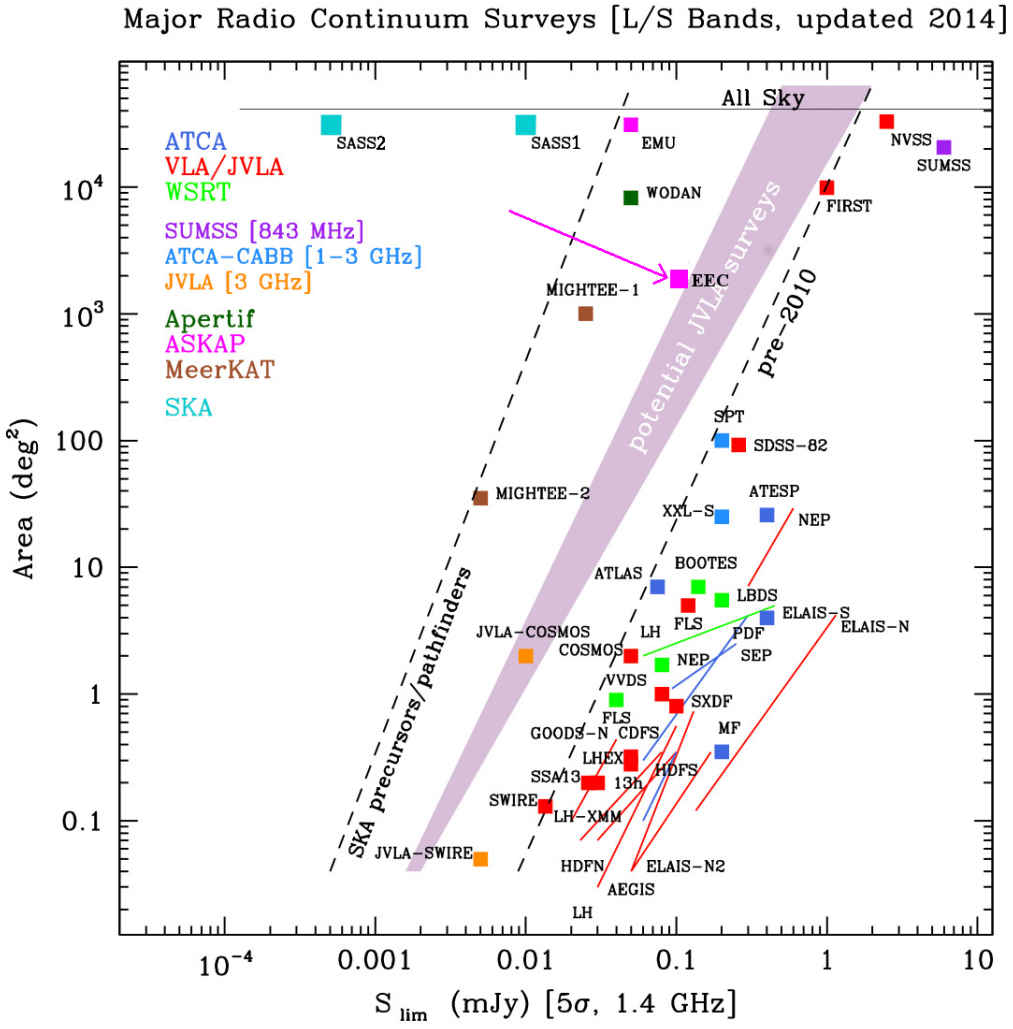

Figure 5.1: A comparison of upcoming and existing radio-continuum surveys taken from Norris et al. (2015). Added in is the proposed EEC field at 2100 square degrees (pink) and 100μJy RMS. The EEC survey probes a new region of the volume/sensitivity parameter space and will likely become available far in advance of the larger, deeper surveys which will eventually supersede it.

three cosmological probes planned for EMU.

5.2.2 Subsidiary Data

The EEC field has been chosen to overlap with both the Dark Energy Survey (DES, Dark Energy Survey Collaboration et al., 2016), for cross identifying to optical sources with high quality photometric redshifts, and the South Pole Telescope Sunyaev Zel'dovich field (SPT-SZ, Story et al. (2013)) for access to high resolution CMB data. The Dark Energy Survey will eventually cover 5000 square degrees of the southern sky down to a limiting i-band magnitude of 24.0. Utilising 6 optical filters (u,g,r,i,z and Y) it will produce accurate photometric redshifts out to z=1. Using this data we will be able to produce auto correlation functions for radio sources at multiple redshift bins as well as cross correlate high and low redshift bins to measure the Cosmic Magnification Effect. The additional CMB observations from SPT-SZ reach a RMS sensitivity 18μK-arcmin at 150 GHz and cover 2540 square degrees of

Table 5.1: Details of the depth of each ancillary data set, the percentage of the EEC covered by each ancillary data set as well as the expected fraction of EEC sources to have counterparts in the covered area and finally the fraction of all EEC sources to have ancillary data counterparts.

Survey	Depth	EEC Coverage	Counterpart Fraction	EEC Counterpart Fraction
DES - Year 1	22.5	63%	73^{+5}_{-7}%	47%
DES - Year 2	24.0	93%	83^{+4}_{-6}%	77%
SPT-SZ		63%	N/A	N/A

sky with arc-minute scale resolution. Using this data we will cross-correlate the CMB with EEC radio sources thereby measuring the Integrated Sachs-Wolfe (ISW) effect between $650 < \ell < 3000$.

Figure 5.2 shows the coverage of these ancillary data sets in relation to our planned EEC field. We can see that nearly 63% of the EEC field is covered by the SPT-SZ CMB data and DES Year-1. With the completion and release of DES Year 2, photometric redshifts will be available for approximately 93% of the EEC field. Based on our analysis of NMBS cross identifications, for a 300μJy field, 98^{+1}_{-4}% of radio sources have a K_s band counterpart. Assuming a DES Year-1 depth of 22.5 mag in the I band, we can expect 73^{+5}_{-7}% of EEC sources (in the area covered by DES Year 1) to have a counterpart (or $\approx$ 47% of all EEC sources). Once DES reaches its full depth this fraction will increase to 83^{+4}_{-6}% of sources covered, or 77% of all EEC sources. All errors are the 1-sigma BETA confidence intervals, (Cameron, 2013). These predictions are summarised in Table 5.1.

In addition to this the EEC field also overlaps with the Murchison Wide-field Array (MWA), Epoch of Re-ionisation (EOR) field. This overlap will allow for the cross-correlation of the angular power spectra from foreground radio galaxies and extremely high redshift radio galaxies, potentially providing a cosmic lensing test at far higher redshifts than previously possible.

5.2.3 Predicted Angular Clustering Sensitivity

With a target sensitivity of 100μJy across 2100 square degrees, the EEC survey is predicted to yield just over 450,000 radio sources, the vast majority of which will never have been studied before. This will allow us to probe the small scale clustering of radio sources with unprecedented accuracy. For comparison, our analysis of NVSS at 15mJy uses 420,196 sources, and the FIRST survey at 1 mJy yields nearly a million sources spread over 10,000 square degrees.While the EEC may at first seem to be the lesser of these three fields, it is important to consider the cosmologically useful area of FIRST and NVSS. For example, the FIRST catalogues are known to include a number of spurious side-lobe sources. Correcting for this using the techniques outlined by the FIRST team in White et al. (1997), reduces the number of available sources to approximately 725,000 and this can be reduced a great deal further by component to source matching, the limited continuous area of the separate fields and shrinkage of the total survey area when limiting to areas with consistent source surface density. For example in the analyses of Cress et al. (1996), Overzier et al. (2003) and Lindsay (2015), source counts of 138665, 188885 and 312645 respectively were used in across a continuous area of $\approx$ 5000-7000 square degrees.

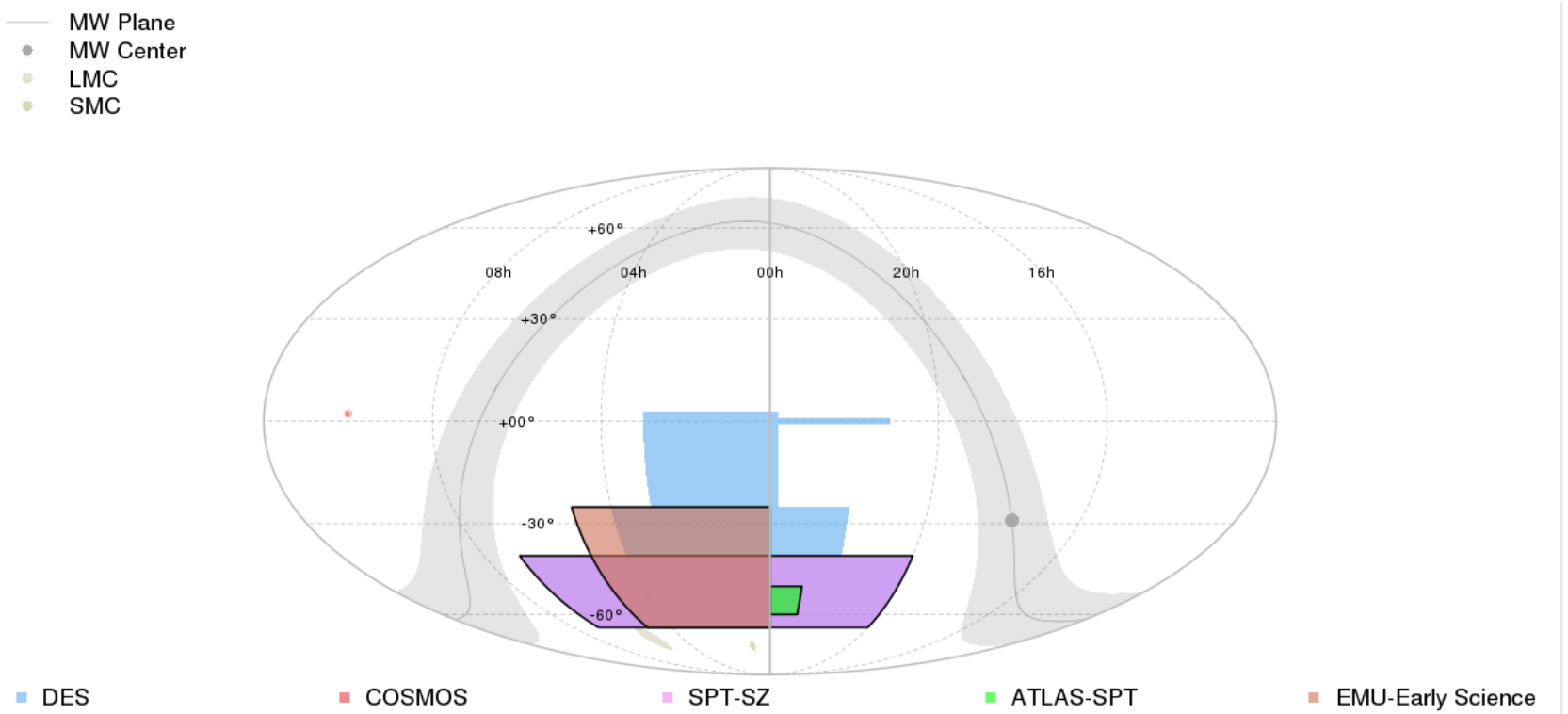

Figure 5.2: The Planned Early EMU Cosmology survey area (Orange). In comparison to the SPT-SZ field (lilac shading), the DES year 1 field (lilac shading) and the DES year 2 field (light blue and lilac shading). For reference the ATLAS-SPT field analysed in Chapter 4 and the Cosmos field analysed in Chapter 2 are also shown, along with the plane and core of the Milky-way shown (Grey shading and circle). This plot was created using the AstroMap software developed by Luke Davies (http://astromap.icrar.org/)

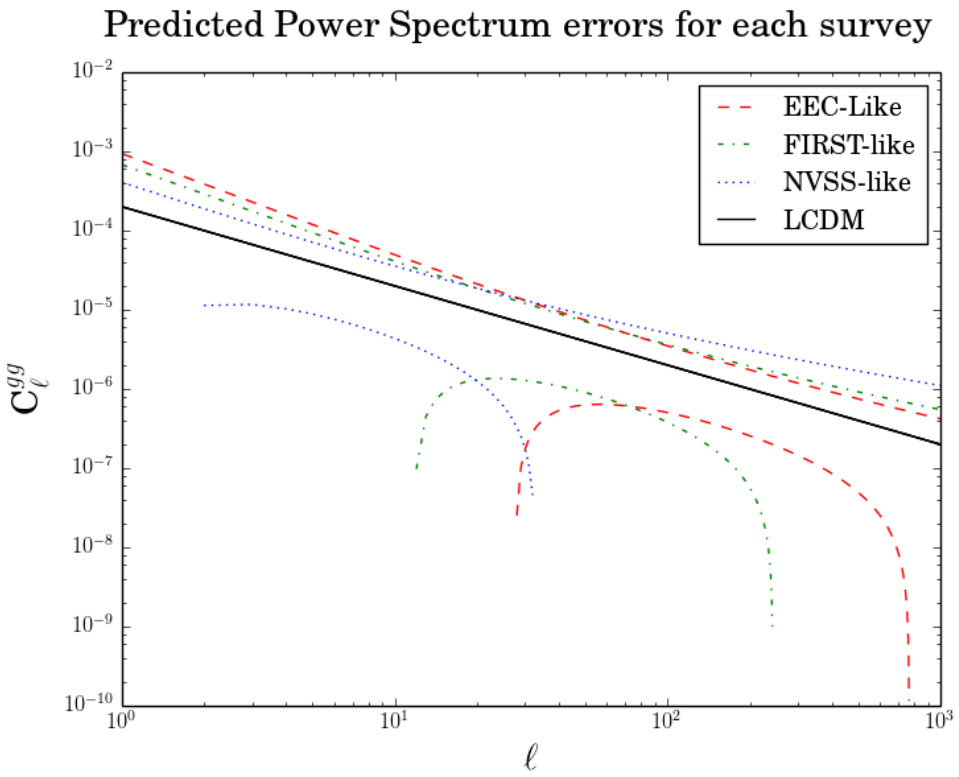

Figure 5.3: Predicted errorbars on the Angular Power Spectrum for a EEC like survey (red dashed line), a FIRST like survey (green dot-dashed line) and NVSS like survey (blue dotted line). Assuming the form of the power law remains the same as that measured for the NVSS survey in the above chapters.

With a minimum separation set by the resolution of the ASKAP beam (0.0041 degrees) and a maximum full count correlation length set by the minimum side-length of the survey area (40 degrees) the source counts of the EEC field are predicted to be comparable to the FIRST survey, but over a much smaller area. Because of this the EEC field is expected to be extremely sensitive to clustering on small scales and will provide new constraints on both the spatial correlation length and bias of radio galaxies at these fluxes. Figure 5.3 shows the predicted sensitivity of the EEC (300μJy, 2000 sq degrees), FIRST (1mJy, 5000 sq degrees) and NVSS (15mJy, 30000 sq degrees), assuming that the power spectrum at each level remains the same as the measured NVSS power spectrum. We can see that the three surveys are complementary, probing different parts of the angular power spectrum. Finally, this measurement assumes a complete lack of redshift information and as such significant improvements will be possible using the photometric redshifts from DES to select high and low redshift bins to correlate.

5.2.4 Planned Probes

For the EEC field we plan to test each of the cosmological effects outlined in Chapter 1. The software to perform the auto correlation function and angular power spectrum is already well established but the next stage of the pipeline development will require new tools to efficiently analyse and model both the cross power spectrum and cross correlation functions of radio data with secondary data sets. Doing so will allow the testing of the ISW and Cosmic

Magnification effects at ever increasing survey depths and scales, first in the Early EMU Cosmology field and ultimately in the full EMU survey.

For the EEC field we aim to measure the ISW effect we by correlating the full sample of radio galaxies with the high resolution data from the SPT-SZ observations of the CMB. While it is not expected that this probe will yield cutting edge cosmological constraints this is a much needed stepping block on the way to full EMU cosmology.

The Cosmic Magnification effect will be constrained using the EEC observations by cross-correlating a sample of foreground galaxies selected using their DES optical counterparts, with a background sample of radio galaxies that have no DES counterpart. This will allow for the selection of two rough redshift bins with minimal overlap. The resulting analysis will enable the determination of the radio galaxy bias as a function of redshift and galaxy type. While this study will be similar to the cross-correlation analysis recently performed for the FIRST/GAMA and VLA/VIDEO surveys (Lindsay, 2015) it will span the gap between those two studies in terms of sensitivity and survey area. This particular probe is expected to be the most powerful of the EEC cosmology tests and should result in new constraints on radio galaxy bias, dark energy and gravity parameters.

5.2.5 Observational Issues

The EEC observations will provide an ideal test-bed for the full EMU survey, as it will enable a better understanding of a large variety of observational effects unique to the ASKAP Phased Array Feeds. Such issues include updated estimates of the expected survey uniformity, the effects of the EMU data reduction pipeline (for example correlation functions have often been used to provide feedback on source finding programs) as well as the impact that such short ‘snap shot’ observations as proposed will have on cosmological analysis. The EEC field will permit a better quantification of the impact of extended sources at lower flux limits and test a variety of component to source matching algorithms to help minimize their impact. Finally and perhaps most importantly the nature of the EMU observations mean that much of the full EMU data will, by necessity, be discarded in the automatic reduction process. The Early EMU Cosmology field will provide us with the vital opportunity to discover unknown issues and potential optimisations *before* the EMU survey is carried out.

"The answer to life, the universe and everything"

Douglas Adams

6 Summary

At the beginning of this thesis we discuss the predicted cosmological sensitivity of the next generation of all sky radio continuum surveys. While these predictions are encouraging, there is often a large gap between any theory and reality. In this thesis we bring together the necessary deep understanding of the faint radio sky with the cosmological analysis and modelling techniques needed to perform a high precision cosmological study of galaxy clustering with EMU.

In Chapter 2 we analyse several existing 1.4 GHz radio continuum fields which reach a similar sensitivity to the upcoming all-sky radio continuum survey the Evolutionary Map of the Universe. By cross-matching these fields to the deep Near Infrared observations of the ZFOURGE and NMBS surveys we are able to determine the redshift, mass, star-formation rate and galaxy type for 412 radio galaxies ($S > 50\mu$Jy). After splitting our population into star-forming or AGN driven radio sources based on the ratio of their radio to optical+infrared star-formation rates (analogous to Radio-Loudness), we determine the AGN fraction as a function of redshift and mass finding that the fraction of galaxies that contain radio-AGN at a given stellar mass shows little dependence on redshift or star-formation activity but is strongly dependant on stellar mass. and note that radio-AGN become exceptionally rare below halo masses of 10^{12} $M_{\odot}$. Finally we use our radio selected sample of AGNs to investigate the effect radio-AGN have on their host galaxy when controlling for the effects of redshift and mass. Interestingly we find the radio-AGN hosts show a strong evolution with redshift. At high-z the majority of our radio-AGN hosts are dusty, star-forming galaxies with indications of a interacting or merger environment but by low redshifts ($z<1$) the typical radio-AGN host is quiescent. Despite this we find no evidence to suggest that the radio-AGN are responsible for this shut-down in star-formation as the trend seen to lower star-formation rates at low redshift is entirely consistent with the evolution of massive galaxies in general. Since we find no discrepancy between the hosts of radio-AGN and non-AGN this might suggest that either radio-AGN feedback is less important than first expected or that radio-AGN occur in the majority of high mass galaxies at some point in their life-cycle.

In Chapter 3 we extend on this work using a far more stringent identifier of radio-AGN

activity, detection using Very Long Baseline Interferometry. To be detectable at VLBI resolutions above z = 0.1, the brightness temperature of the emitting source at 10μJy would be in excess of 3×10^5K. This is inconsistent with emission from star-formation and as such VLBI detection of extra-galactic radio sources can be used to provide robust confirmation of AGN activity. Using wide area VLBI observations of the entire COSMOS field, we reproduce our analysis of Chapter 1. By cross matching VLBI sources with NMBS observations we find that VLBI selected radio-AGN hosts account for 49% of high-luminosity sources and show no difference from those selected by an excess of radio emission and are statistically representative of the whole radio-loud population in terms of stellar-mass, SSFRs, redshift and dust. Importantly we find that 20^{+6}_{-4}% of VLBI-detected sources are radio-quiet and hence may be miss-identified as star-forming sources in the EMU survey.

In Chapter 4 we use the relations found in Chapter 2 to devise a process for converting large semi-analytic simulations into a simulated radio sky. After populating the dark matter halos of the simulation using the SAGE galaxy evolution software, we invert the well known radio flux to star-formation rate equation of Bell (2002) to produce a baseline level of radio flux for each galaxy. We then use the redshift and mass dependant AGN fraction from our previous work to populate radio-AGN throughout the simulated galaxy population and utilise the Luminosity Function of Mauch & Sadler (2007) to select the expected radio luminosity of each radio-AGN powered source, though in practise exact luminosity function used here makes little difference to the simulated sky at EMU like flux levels. The radio luminosities are then summed and converted to fluxes using the simulated sources redshift information and 'imaged' with a flux criteria. We measure the auto correlation function of this simulated data set and find it in good agreement with a numerical model of the expected auto-correlation function for the WMAP-1 cosmology parameters used in the Millennium Simulation.

We measure the correlation function and angular power spectrum of the NVSS radio survey in order to both develop the tools needed for a cosmological analysis and to more fully understand the effects of observational artefacts at large scales. Two of the most important artefacts known on large scales are the removal of excess correlation on large scales due to bright extended sources and spurious local correlations caused by sources in the plane of the Milky Way. After correcting for these the NVSS auto correlation is found to have an amplitude of $1.6 \pm 0.1 \times 10^{-3}$, and slope of -0.7 ± 0.1 suggesting a high radio galaxy bias. Converting these measurements into a spatial correlation length assuming a redshift distribution from the SKADs simulation and assuming a stable clustering model we find $r_0^{\epsilon=0} = 5.4^{+0.2}_{-0.2}$ h^{-1} Mpc. We measure the angular power spectrum of at multipoles greater than 30 to be well fit by a power-law with an amplitude of $2.19 \pm 0.3 \times 10^{-4}$ and slope of = -1.23 ± 0.06, and note that all of these values are in good agreement with previous work.

In addition to this we also measure the the auto correlation functions on much smaller scales using two separate, deep radio surveys; the JVLA Stripe-82 and ATLAS-SPT observations at 240μJy and 300μJy. Both surveys yield much less power at scales less than 0.1 degrees than seen in NVSS, consistent with a relative decrease in the fraction of large extended sources. At larger separations, dominated by cosmological clustering, we find a much higher correlation amplitude than expected given previous work at 3 mJy levels. For the Stripe-82 observations we attribute this elevation to the much reduced and elongated survey area which was caused by missed observation time, along with the effects of varying

source surface density which cannot be mitigated by moving to higher S/N ratios without reducing the number of sources available below the point of meaningful analysis. In the ATLAS-SPT observations we find that the elevated correlation function amplitude is entirely driven by excess power at scales of 0.2-0.3 degrees and note that a similar bump at these scales has been noted before at much higher fluxes, in correlation function studies of the FIRST sample. While this 'bump' may be a systematic effect of high resolution surveys it is also possible that it represents the typical angular separation of interacting galaxies. Removing these scales from our analysis we find a correlation function amplitude of $1.6 \pm 0.24 \times 10^{-3}$ with a slope of -0.8 ± 0.3. This is still above the amplitude of the auto correlation function measured in the FIRST and NVSS surveys at 3mJy and may indicate that either clustering is stronger at these flux limits or that our deep surveys sample a volume with an over abundance of clustering compared to the total sky. Finally we convert this measured slope and amplitude into a spatial correlation length, despite the elevation in amplitude we find that the measured spatial correlation length $r_0^{\epsilon=0} = 2.2^{+3.4}_{-1.7}$ h^{-1} Mpc is in good agreement with an extrapolation of the flux independent trend seen in FIRST between 3-30mJy.

In Chapter 5 we discuss the future surveys for which the work in this thesis is applicable. It is hoped that using a combination of all of the cosmological effects outlined in Chapter 1 along with the new techniques outlined here, for simulating observable artefacts in cosmological simulations that the next generation of all-sky radio continuum surveys will reach their full potential, providing us with an unprecedented window into the inner workings of our Universe.

A

Appendix: Upcoming Surveys

SUPPLEMENTARY DATA: TABLE 1: List of major radio surveys

Name	date 1st pub	telescope	Technology	mean freq (MHz)	resolution (arcsec)	S-min (mJy)	# sources	area (sq deg)	Bibcode
Reber40	1940	Reber	dish	162	10800.0	9E+05	1	-1.0	1940ApJ....91..621R Reber
Reber44	1944	Reber	dish	160	10800	1.1E+04	6	30000.0	1944ApJ...100..279R Reber
Hey	1946	Yagi	other	64	21600	2.2E+08	1	28236.3	1946Natur.157..296H Hey
Bolton	1948	Sea interfer.	other	100	4000	80000	9	10178.2	1948Natur.162..141Bolton
1C	1950	MRAO	array	81	4000	30000	50	17052.0	1950MNRAS.110..508Ryle+
Stanley&Slee	1950		other	100	36000	1.0E+05	22	31614.0	1950AuSRA...3..234S
Mills	1952		other	101	3600	80000	77	36444.5	1952AuSRA...5..266Mills
Brown & Hazard	1953	Jodrell	dish	158	7200	5000	23	6126.0	1953MNRAS.113..123Hanbury Brown
BSS	1954	Sea interfer.	other	10	3600	40000	104	31614.0	1954AuJPh...7..110B Bolton
Shain & Higgins	1954	coplanar	other	18.3	62220	3.0E+06	37	24219.0	1954AuJPh...7..130Shain
2C	1955	MRAO	array	81	3600	10000	1936	33161.2	1955MmRAS..67..106Shakeshaft
MSH	1958	Mills cross	synth	85.5	3000	10000	2270	23968.0	1958AuJPh..11..360Mills
3C	1959	MRAO	array	159	3100	8000	471	27251.3	1959MmRAS..68...37Edge
3CR	1962	MRAO	array	178	2600	9000	328	22326.4	1962MmRAS..68..163Bennett
4C	1965	MRAO	array	178	90.0	2000	4843	23837.0	1967MmRAS..71...49Gower
OSS	1968	Ohio	other	1415	600	160	1200	28564.6	1968AJ.....73..381Dixon
PKS	1968	Parkes	dish	1,410	480	4000	1780	27693.0	1969AuJPA...7....3E J.Ekers
B2	1970	Bologna	cylinder	408	360.0	250	9929	5910.0	1970A&AS....1..281Colla,1974A&AS...18..147Fanti
GB	1972	Greenbank	dish	1400	600.0	90	1086	521.0	1972AcA....22..227Maslowski
Molonglo (MC1-MC4)	1973	Molonglo	cylinder	408	162.0	200	4160	1590.3	1973AuJPA..28....1Davies, 1974AuJPA..33....1Sutton,1976AuJPA..40....1Clarke 1975AuJPA..36....1Slee & Higgins;
CUL2	1975	Culgoora	synth	80	222.0	2000	2747	29133.3	1995AuJPh..48..143Slee
NAIC	1975	Arecibo	dish	611	756.0	350	3122	5203.3	1975NAICR..45....1Durdin
CUL3	1977	Culgoora	synth	160	114.0	1200	2045	25562.5	1977AuJPA..43....1Slee
GB2	1978	Greenbank	dish	1400	600.0	90	2022	919.1	1978AcA....28..367Machalski
MRC	1981	MOST	cylinder	408	120.0	700	12141	25938.0	1991Obs...111...72Large; 1981MNRAS.194..693Large
NAIC-GB	1983	Greenbank	dish	4775	168.0	30	2661	4435.0	1983ApJS...51...67Lawrence
6C	1985	MRAO	array	151	270.0	300	28000	10318.0	1993MNRAS.263...25H Hales

Figure A.1: Details of upcoming radio continuum surveys: Part 1. Reproduced with permission, Norris et al, Nature Astronomy, in press.

B3	1985	Bologna	cylinder	408	240.0	100	13354	2568.1	1985A&AS...59..255Ficarra, 1991A&A...241...35Basso
MIT-GB	1986	Greenbank	dish	4850	168.0	50	24180	16120.0	1986ApJS...61....1Bennett,1991ApJS...75..801Griffith
IPS	1987		array	82	12000.0	5000	1789	24065.0	1987MNRAS.229..589Purvis
Zelenchuk	1989	RATAN	dish	3900	1500.0	50	8503	5001.8	1985SoSAO..46...59Amirkhanyan, 1991SoSAO..68...14Larionov
87GB	1991	Greenbank	dish	4850	210.0	25	54579	19932.0	1991ApJS...75.1011Gregory
BWE	1991	Greenbank	dish	4850	210.0	25	53522	19823.0	1991ApJS...75....1Becker
Ratan	1991	Ratan	dish	3900	1500.0	15	1145	371.6	1991A&AS...87....1Parijskij,1992A&AS...96..583Parijskij
Wieringa327	1991	WSRT	synth	327	60.0	3	4500	95.0	1993BICDS..43...17W
WB92	1992	greenbank	dish	1400	600.0	100	30239	22233.0	1992ApJS...79..331White
PMN	1994	Parkes	dish	4850	294	30	50814	25862.0	1996ApJS..103..145Wright
VLA-NEP	1994	VLA	synth	1500	20.0	0.3	2435	29.3	1994ApJS...93..145Kollgaard
8C	1995	MRAO	array	38	270.0	1000	5859	2764.0	1995MNRAS.274..447Hales, 1990MNRAS.244..233Rees
GB6	1996	Greenbank	dish	4850	210.0	18	75162	20028.0	1996ApJS..103..427Gregory GB6
MIYUN	1996	Miyun	synth	232	228.0	200	34426	10178.0	1997A&AS..121...59Zhang
Texas	1996	texas	synth	365	10.0	400	66841	33420.5	1996AJ....111.1945Douglas
WENSS	1997	WSRT	synth	325	54	18	230000	10318.0	1997A&AS..124..259Rengelink
FIRST	1998	VLA	synth	1400	6.0	1	816331	10507.0	1995ApJ...450..559Becker , 1997ApJ...475..479White ,http://sundog.stsci.edu/
NVSS	1998	VLA	synth	1400	45.0	2.5	1773484	33818.0	1998AJ....115.1693Condon
7C	1999	MRAO	array	151	72.0	50	120000	13578.0	2007MNRAS.382.1639H Hales
SUMSS	1999	MOST	cylinder	843	42.0	6	211063	10318.0	2003MNRAS.342.1117M Mauch, http://www.astrop.physics.usyd.edu.au/sumsscat/
ATESP	2000	ATCA	synth	1400	12.0	0.4	2960	26.0	2000A&AS..146...41Prandoni
Bootes-WSRT	2002	WSRT	synth	1400	18.0	0.14	3172	7.0	2002AJ....123.1784deVries
WISH	2002	WSRT	synth	352	54.0	18	73570	5818.0	2002A&A...394...59De Breuck
CLASS	2003	VLA	synth	8460	0.0	2	13783	0.0	2003MNRAS.341....1Myers
FLS-VLA	2003	VLA	synth	1400	5	0.115	3565	5.0	2003AJ....125.2411Condon
Phoenix	2003	ATCA	synth	1400	9.0	0.06	2090	4.5	2003AJ....125..465Hopkins
VVDS	2003	VLA	synth	1400	6	0.08	1054	1.0	2003A&A...403..857Bondi
FLS-WSRT	2004	WSRT	synth	1400	12	0.02	1048	1.0	2004A&A...424..371Morganti
ATLAS	2006	ATCA	synth	1580	10	0.07	5118	7.0	2006AJ....132.2409Norris; 2015MNRAS.453.4020Franzen

Figure A.2: Details of upcoming radio continuum surveys: Part 2. Reproduced with permission, Norris et al, Nature Astronomy, in press.

Biggs-Ivison	2006	VLA	synth	1400	1.4	0.025	1243	0.3	2006MNRAS.371..963Biggs
AEGIS20	2007	VLA	synth	1400	3.8	0.13	1123	0.7	2007ApJ...660L..77Ivison
COSMOS	2007	VLA	synth	1400	1.5	0.04	3643	2.0	2007ApJS..172...46Schinnerer
FLS-GMRT	2007	GMRT	synth	610	6.0	0.12	3944	3.9	2007MNRAS.376.1251Garn
MRT	2007	Mauritius	synth	151	260.0	1300	2784	23968.0	2007HiA....14..385Pandey
VLSS	2007	VLA	synth	74	75.0	500	92964	30215.0	2007AJ....134.1245Cohen, 2014MNRAS.440..327Lane
ELAISN1-610	2008	GMRT	synth	610	6.0	0.14	2500	8.9	2008MNRAS.383...75Garn
LH-610	2008	GMRT	synth	610	5	0.36	7779	5.0	2008MNRAS.387.1037Garn, 2010BASI...38..103Garn
LH-Owen	2008	VLA	synth	1400	1.6	0.0135	2056	0.4	2008AJ....136.1889Owen
LH-Garn	2008	GMRT	synth	610	6.0	0.36	2845	5.0	2008MNRAS.387.1037Garn
SWIRE	2008	VLA	synth	1400	1.6	0.014	2056	0.4	2008AJ....136.1889Owen
COMA	2009	VLA	synth	1400	4.8	0.1	1030	1.0	2009AJ....137.4436Miller
ELAISN1-325	2009	GMRT	synth	325	9.0	0.27	1286	3.1	2009MNRAS.395..269Sirothia
LH-Ibar	2009	VLA+GMRT	synth	610	5	0.03	1587	1.5	2009MNRAS.397..281Ibar
SWIREII	2009	VLA	synth	327	6.2	0.3	1436	3.1	2009AJ....137.4846Owen
AT20G	2010	ATCA	other	20000	10	200	5890	20684.7	2010MNRAS.402.2403Murphy
ATLBS	2010	ATCA	synth	1388	50	0.4	1094	8.4	2010MNRAS.402.2792Subrahmanyan
PKS	1991	Parkes	dish	2700	480.0	60	8264	27546.7	1991PASAu...9..170Otrupcek
10C	2011	AMI	synth	15700	30.0	0.5	1897	27.0	2011MNRAS.415.2708AMI
GAMA-gmrt325	2013	GMRT	synth	325	19	1	5263	90.0	2013MNRAS.435..650Mauch
GLEAM	2016	MWA	MPA	151	120	50	305615	24296.3	2017MNRAS.464.1146Hurley-Walker
Stripe82	2016	VLA	synth	1500	13	0.44	8948	100.0	2016MNRAS.460.4433Heywood
ASKAP-BETA	2016	ASKAP	PAF	863	65	1.9	3722	150.0	2016MNRAS.457.4160Heywood
Bootes-LOFAR	2016	LOFAR	MPA	150	6.5	0.6	6276	19.0	2016MNRAS.460.2385Williams
TGSS	2016	GMRT	synth	147	25	12	623605	37101.2	2017A%26A...598A..78Intema, http://tgss.ncra.tifr.res.in/ 2011JApA...32..557Rottgering,
Apertif	2018	WSRT	PAF	1350	15	0.075	2.0E+07	10000.0	https://www.astron.nl/radio-observatory/apertif-surveys
ASKAP-ESP3	2017	ASKAP	PAF	1100	30.0	0.4	200000	2000.0	http://tinyurl.com/guvvj8e
ATLAS-SPT	2016	ATCA	synth	2100	10	0.4	9000	85.0	2016arXiv160201914O
LOFAR-Tier1	2017	LOFAR	MPA	145	6.5	0.5	5.0E+07	20636.0	2010iska.meetE..50Rottgering
MSSS-HBA	2017	LOFAR	MPA	144	120	100	175000	20028.1	2015A&A...582A.123Heald

Figure A.3: Details of upcoming radio continuum surveys: Part 3. Reproduced with permission, Norris et al, Nature Astronomy, in press.

EMU	2018	ASKAP	PAF	1250	10	0.05	7.0E+07	30000.0	2011PASA...28..215Norris
MIGHTEE	2018	Meerkat	synth	1400	6	0.005	200000	20.0	Jarvis & Taylor, 2017, PoS: MeerKat Science
VLASS	2018	VLA	synth	3000	2.5	0.35	1.0E+07	33900.0	https://science.nrao.edu/science/surveys/vlass
Chilesconpol	2020	VLA	synth	1400	4	0.002	8000	0.2	http://www.chilesconpol.com/

Notes to Table 1:

- For complex surveys, such as those made at more than one frequency, numbers in table are representative, and the cited paper should be consulted for full details.
- Where a survey has several data releases, these are generally merged into one or two references, which typically give the first and last (or major) publications on the survey
- Survey properties are those of the final published catalogue
- This list excludes:
    - Surveys with less than 1000 sources (except for historically significant surveys)
    - Surveys with no published source catalogue
- -1 in any entry means an unknown quantity

Figure A.4: Details of upcoming radio continuum surveys: Part 4. Reproduced with permission, Norris et al, Nature Astronomy, in press.

B

Appendix: ZFOURGE and NMBS Data Samples

RA [deg]	DEC [deg]	$PF_{1.4}$ [μJy]	$PE_{1.4}$ [μJy]	$IF_{1.4}$ [μJy]	$IE_{1.4}$ [μJy]	RMS [μJy]	KsLimit [mag]	Sep [arcsec]	KsNearest [mag]	Cmnt
149.7393292	2.4506194	69.0	12.0	69.0	12.0	12.0	23.73	3.49	23.05	-
149.7405542	2.6053000	125.0	14.0	125.0	14.0	14.0	23.55	0.20	16.81	-
149.7515542	2.5240667	46.0	13.0	46.0	13.0	13.0	24.02	4.44	23.65	-
149.7698083	2.2180667	44.0	12.0	44.0	12.0	12.0	23.97	1.15	22.06	-
149.7769625	2.4667833	50.0	13.0	50.0	13.0	13.0	24.19	2.00	21.43	-
149.7876500	2.2293944	47.0	11.0	47.0	11.0	11.0	24.00	3.58	22.53	-
149.7935083	2.2583306	57.0	10.0	57.0	10.0	10.0	23.81	2.48	22.78	-
149.8471583	2.2152889	65.0	11.0	65.0	11.0	11.0	24.19	1.34	22.11	-
149.8623292	2.4679250	41.0	11.0	41.0	11.0	11.0	24.19	4.66	21.34	-
149.8673417	2.2416222	87.0	11.0	87.0	11.0	11.0	24.21	4.46	20.7	-
149.8717583	2.2121917	67.0	12.0	67.0	12.0	12.0	24.20	4.07	21.84	-

Table B.1: Extract of the included data set detailing radio sources that have no detected counterpart within the NMBS COSMOS observations. RA is the right ascension of the radio source in decimal degrees, DEC is the declination of the radio source in decimal degrees. $PF_{1.4}$ is the 1.4 GHz peak radio flux in micro-Janskys, $PE_{1.4}$ is the error on the 1.4 GHz peak radio flux in micro-Janskys, $IF_{1.4}$ is the integrated 1.4 GHz flux in micro-Janskys and $IE_{1.4}$ is the error on the integrated flux in micro-Janskys. RMS is the local RMS at the source in micro-Janskys, KsLimit is the limiting Ks magnitude at the source position in magnitudes with a zero-point of 25. Sep is the separation between the radio source and the nearest Ks detected object in arc-seconds and KsNearest is the magnitude of this nearest Ks detected object, in magnitudes with a zero-point of 25. Comnt is an index referring to any comments on the source which are located at the top of the catalogue. This data is taken from the COSMOS Deep project catalogues. The full tables for each of our fields *Ks* non-detections are available online.

ID	RA [deg]	DEC [deg]	*Ks*-Band [MAG]	z_{phot}	z_{spec}	Stellar-mass [$M_\odot$]	$F_{1.4}$ [μJy]	$L_{1.4}$ [W Hz]	L_{IR} [W Hz]	L_{UV} [W Hz]	SFR_{Radio} [$M_\odot$ yr^{-1}]	SFR_{UV+IR} [$M_\odot$ yr^{-1}]	SFR-Ratio	Type
COSMOS-10055	150.14721680	2.33718370	19.87	0.74	0.73	10.69	67.0	1.13e+23	9.96e+11	1.24e+10	3.58e+01	1.13e+02	0.32	SF
COSMOS-10472	150.07937620	2.34056950	22.78	0.22	-	8.21	61.0	7.58e+21	1.42e+10	3.76e+07	2.41e+00	1.57e+00	1.54	SF
COSMOS-1055	150.05722050	2.20592760	18.62	0.09	0.19	9.43	446.0	9.08e+21	4.09e+10	2.28e+08	2.89e+00	4.54e+00	0.64	QU
COSMOS-1086	150.09982300	2.20327520	21.71	1.27	-	10.75	84.0	4.44e+23	1.27e+11	8.16e+09	1.41e+02	1.68e+01	8.42	SF
COSMOS-1096	150.05662540	2.20855470	18.79	0.21	-	10.13	342.0	4.02e+22	5.69e+11	1.20e+09	1.28e+01	6.25e+01	0.20	SF
COSMOS-11061	150.18797300	2.35292740	19.50	0.27	-	10.07	90.0	1.73e+22	7.78e+10	8.21e+08	5.50e+00	8.78e+00	0.63	SF
COSMOS-11391	150.17570500	2.35869840	18.36	0.21	-	10.51	94.0	1.10e+22	1.23e+11	4.08e+09	3.50e+00	1.49e+01	0.23	SF
COSMOS-11542	150.08515930	2.35732890	20.97	1.21	-	10.99	211.0	1.02e+24	5.51e+10	6.04e+09	3.24e+02	8.18e+00	39.61	QU
COSMOS-11559	150.14303590	2.35588170	24.20	3.00	-	10.45	517.0	1.51e+25	1.38e+13	2.74e+10	4.81e+03	1.52e+03	3.18	SF

Table B.2: Extract of the included data set. ID is the Field & ID of the ZFOURGE *Ks*-band object, RA is the right ascension of the ZFOURGE *Ks*-band object in decimal degrees, DEC is the declination of the ZFOURGE *Ks*-band object in decimal degrees, z_{phot} is the peak of photometric redshift probability distribution determined by EAZY for the ZFOURGE *Ks*-band object, Stellar-mass is the logged stellar-mass of the ZFOURGE *Ks*-band object in $M_\odot$, $F_{1.4}$ is the 1.4 GHz flux of the ZFOURGE *Ks*-band object in micro-Janskys assuming association of sources within 1", $L_{1.4}$ is the 1.4 GHz luminosity of the ZFOURGE *Ks*-band object assuming association of sources within 1″ and a spectral index of 0.5 in WHz, L_{IR} is the bolometric IR luminosity of the ZFOURGE *Ks*-band object assuming a Wuyts 2011 average SED template to extrapolate from 24um fluxes, L_{UV} is the EAZY interpolated rest-frame 2800 Å luminosity of the ZFOURGE *Ks*-band object, SFR_{Radio} is the 1.4 GHz luminosity of the radio object in $M_\odot$ per year, SFR_{UV+IR} is the combined SFR from L_{UV} & L_{IR} in $M_\odot$ per year and Type is the stellar population type of the *Ks*-band object based on our rest-frame UVJ color-color classification into Quiescent (QU) or Star-forming (SF) sources. The full table is available online.

ID	RA [deg]	DEC [deg]	*Ks*-Band [MAG]	z_{phot}	z_{spec}	Stellar-mass [$M_\odot$]	$F_{1.4}$ [μJy]	$L_{1.4}$ [W Hz]	L_{IR} [W Hz]	L_{UV} [W Hz]	SFR_{Radio} [$M_\odot$ yr^{-1}]	SFR_{UV+IR} [$M_\odot$ yr^{-1}]	SFR-Ratio	Type
NMBS-30222	149.75816471	2.18125926	19.66	0.93	-	10.76	83.0	2.60e+23	1.02e+11	6.16e+09	1.44e+02	1.30e+02	1.11	SF
NMBS-33599	150.17541090	2.42608575	18.29	0.31	0.31	9.91	112.0	3.00e+22	2.03e+10	8.52e+09	1.66e+01	3.58e+01	0.46	SF
NMBS-16854	150.00712980	2.45347805	18.65	0.76	-	11.23	761.0	1.54e+24	6.36e+08	3.75e+09	8.48e+02	6.59e+00	128.80	QU
NMBS-16644	149.85016665	2.45223286	19.41	0.72	0.71	10.55	1102.0	1.98e+24	1.17e+10	5.65e+09	1.10e+03	4.78e+01	22.91	SF
NMBS-13387	150.09534701	2.38475016	17.48	0.28	0.27	10.80	240.0	5.30e+22	9.06e+10	2.20e+09	2.93e+01	1.97e+01	1.49	SF
NMBS-31704	149.86023730	2.29759213	20.77	1.83	-	11.12	68.0	9.41e+23	5.07e+10	2.39e+10	5.20e+02	3.77e+02	1.38	SF
NMBS-11075	149.96143463	2.34943035	19.14	0.93	-	11.18	230.0	7.28e+23	2.07e+10	5.55e+09	4.02e+02	4.25e+00	94.59	QU
NMBS-2925	149.74311397	2.21380815	19.04	0.87	0.89	11.21	309.0	8.41e+23	2.21e+10	4.11e+09	4.64e+02	4.91e+00	94.65	QU
NMBS-6355	149.85677987	2.27315493	18.73	0.76	0.76	11.12	88.0	1.78e+23	2.21e+10	1.20e+10	9.81e+01	6.46e+01	1.52	SF
NMBS-7479	149.88340095	2.29052069	18.16	0.49	0.48	10.96	86.0	6.45e+22	2.13e+09	1.76e+09	3.56e+01	4.79e+00	7.43	QU
NMBS-23410	150.05479754	2.56948127	19.97	0.76	-	10.37	162.0	3.24e+23	2.31e+10	5.78e+09	1.79e+02	1.56e+02	1.15	SF

Table B.3: Extract of the included NMBS data set. As above. Full table is available online

C

Appendix: NVSS Masking Table

RA [deg]	DEC [deg]	Mask Size [deg]	Source Name
23.5	-36.5	1.0	NGC0612
24.4	33.3	1.0	3C48
50.0	41.6	1.4	3C84
50.5	-37.2	1.8	Fornax A
69.3	29.7	1.8	3C123
80.7	-36.6	1.4	-
83.6	22.6	4.4	3C144
83.7	-5.3	2.8	3C145
85.4	-2.0	1.6	3C147.1
85.7	49.9	1.6	3C147
88.5	-5.0	1.2	-
96.9	-5.8	1.4	3C161
139.5	-12.1	1.4	Hydra A
184.8	5.8	1.0	3C270
187.3	2.0	1.4	3C273
187.5	12.5	2.0	3C274
212.9	52.2	1.6	3C295
253.0	5.0	1.0	Hercules A
260.1	-1.0	1.4	3C353
276.0	1.7	1.0	-
291.0	-29.3	1.0	-
299.8	40.8	6.2	Cygnus A

Table C.1: The central position and half side length of each square region masked due to a known extended bright radio source. This mask is identical to that used in Blake et al 2012 and 2014 and was acquired by private communication. Since no obvious public record of it could be found it is reproduced here for reference purposes.

List of Acronyms

Acronym	Meaning
2MASS	2 Micron All Sky Survey
ACF	Angular/Auto Correlation Function
AGN	Active Galactic Nuclei
APERTIF	APERture Tile In Focus
APS	Angular Power Spectrum
ASKAP	Australian Square Kilometer Array Pathfinder
ASKAP-12	ASKAP Twelve Anttena Array
ATCA	Autralian Telescope Compact Array
ATLAS	ATCA Large Area Survey
ATLAS-SPT	ATLAS observations of the SPT field
BETA	The Beta Distribution Generator for Binomial Confidence Intervals
CAMB	Cosmic Anisotropy Microwave Background code
CANDELS	Cosmic Assembly Near-infrared Deep Extragalactic Survey
CCF	Cross Correlation Function
CDFS	Chandra Deep Field South
CMB	Cosmic Microwave Background
CO	Carbon Monoxide
COSMOS	The Cosmological Evolution Survey
DEC	Declination
DES	Dark Energy Survey
EAZY	Easy and Accurate Z_{phot} from Yale
EEC	Early EMU Cosmology Field
EMU	Evolutionary Map of the Universe
FAST	Fitting and Assessment of Synthetic Templates
FIR	Far Infrared
FIRST	Faint Images of the Radio Sky at Twenty centimers
FRI	Fanaroff and Riley Type I radio galaxy
FRII	Fanaroff and Riley Type II radio galaxy
FWHM	Full Width Half Maximum
GAMA	Galaxy And Mass Assembly
HEAO	High Energy Astrophysical Observatory
HM	High Mass
HST	Hubble Space Telescope
HT	Head Tail galaxy
IFRS	Infrared Faint Radio Source
IR	Infrared
ISW	Integrated Sachs-Wolfe Effect
JVLA	Jansky Very Large Array
KS-Test	KolmogorovSmirnov test
LCDM	Lambda Cold Dark Matter
LM	Low Mass
MAG	Cosmic Magnification
MICE	Marenostrum Institut de Ciencias de l'Espai Simulations
MIPS	The Multiband Imaging Photometer

Acronym	Meaning
NIR	Near Infrared
NMAD	Normalised Median Absolute Deviation
NMBS	Newfirm Medium Band Survey
NRAO	National Radio Astronomy Observatory
NVSS	NRAO Very Large Array Sky Survey
QU	Quiescent
QUASAR	Quasi-Stellar Radio Object
RA	Right Ascension
RMS	Root Mean Square
S/N	Signal to Noise
S^3-SEx (SKADS)	SKA Design Studies Simulated Skies: Semi-Empirical Extra Galactic Simulations
SAGE	Semi-Analytic Galaxy Evolution code
SDSS	Sloan Digital Sky Survey
SED	Spectral Energy Distribution
SF	Star-forming
SFG	Starforming Galaxy
SFR	Star-formation Rate
SKA	Square Kilometer Array
SMBH	Super Massive Black Hole
SN	Super Nova
Sne	Supernova Explosion
SNR	Supernova Remnant
SPT	South Pole Telescope
SPT-SZ	South Polar Telescope-Sunyarv-Zel'dovich
SSFR	Specific Star-formation Rate
SUMSS	Sydney University Molongo Sky Survey
TAO	Theoretical Astrophysical Observatory
UV	Ultra Violet
UVJ	The U, V and J bands
VIDEO	VISTA Deep Extragalactic Observations
VISTA	Visible and Infrared Survey Telescope for Astronomy
VLA	Very Large Array
VLBA	Very Long Baseline Array
VLBI	Very Long Baseline Interferometry
WAT	Wide Angle Tail galaxy
WENSS	Westerbork Northern Sky Survey
WISE	Widefield Infrared Survey Explorer
WMAP	Wilkinson Microwave Anisotropy Probe
WODAN	Westerbork Observations of the APERTIF Northern sky
ZFOURGE	FourStar Galaxy Evolution redshift survey

Symbol	Meaning	
Ω_m	Mass Density	0.25
Ω_Λ	Dark Energy Density	0.705
Ω_b	Baryonic Matter Density	0.045
σ_8	Linear power spectrum amplitude at 8 h^{-1} Mpc	0.9
H_0	Hubble Constant	0.73

References

Afshordi, N., Loh, Y.-S., & Strauss, M. A. 2004, Phys. Rev. D, 69, 083524

Alam, S., Albareti, F. D., Allende Prieto, C., et al. 2015, The Eleventh and Twelfth Data Releases of the Sloan Digital Sky Survey: Final Data from SDSS-III, Vol. 219, The Astrophysical Journal Supplement Series, 219, 12

Allen, S. W., Evrard, A. E., & Mantz, A. B. 2011, Cosmological Parameters from Observations of Galaxy Clusters, Vol. 49, Annual Review of Astronomy and Astrophysics, 49, 409

Allen, S. W., Mantz, A. B., Morris, R. G., et al. 2013, Measuring cosmic distances with galaxy clusters, ArXiv e-prints

Allen, S. W., Rapetti, D. A., Schmidt, R. W., et al. 2008, Improved constraints on dark energy from Chandra X-ray observations of the largest relaxed galaxy clusters, Vol. 383, Monthly Notices of the Royal Astronomical Society, 383, 879

Auriemma, C., Perola, G. C., Ekers, R. D., et al. 1977, A Determination of the Local Radio Luminosity Function of Elliptical Galaxies, Vol. 57, Astronomy and Astrophysics, 57

Banfield, J. K., Andernach, H., Kapińska, A. D., et al. 2016, Radio Galaxy Zoo: discovery of a poor cluster through a giant wide-angle tail radio galaxy, Vol. 460, MNRAS, 460, 2376

Bardeen, J. M., Bond, J. R., Kaiser, N., & Szalay, A. S. 1986, The statistics of peaks of Gaussian random fields, Vol. 304, The Astrophysical Journal, 304, 15

Becker, R. H., White, R. L., & Helfand, D. J. 1995, The FIRST Survey: Faint Images of the Radio Sky at Twenty Centimeters, Vol. 450, The Astrophysical Journal, 450, 559

Behroozi, P. S., Wechsler, R. H., & Conroy, C. 2013, The Astrophysical Journal, 770, 57

Bell, E. F. 2002, The Astrophysical Journal, 586, 794

Bell, E. F. 2003, The Astrophysical Journal, 586, 794

Bell, E. F., Papovich, C., Wolf, C., et al. 2005, The Astrophysical Journal, 625, 23

Bennett, C. L., Larson, D., Weiland, J. L., et al. 2013, Nine-year Wilkinson Microwave Anisotropy Probe (WMAP) Observations: Final Maps and Results, Vol. 208, The Astrophysical Journal, 208, 20

Bernyk, M., Croton, D. J., Tonini, C., et al. 2016, The Theoretical Astrophysical Observatory: Cloud-based Mock Galaxy Catalogs, Vol. 223, The Astrophysical Journals, 223, 9

Best, P. N., Kauffmann, G., Heckman, T. M., et al. 2005, Monthly Notices of the Royal Astronomical Society, 362, 25

Best, P. N., Von Der Linden, A., Kauffmann, G., Heckman, T. M., & Kaiser, C. R. 2007, Monthly Notices of the Royal Astronomical Society, 379, 894

Bicknell, G. V., Sutherland, R. S., van Breugel, W. J. M., et al. 2000, The Astrophysical Journal, 540, 678

Blake, C., Ferreira, P. G., & Borrill, J. 2004, Monthly Notices of the Royal Astronomical Society, 351, 923

Blake, C., Mauch, T., & Sadler, E. M. 2003, Angular clustering in the SUMSS radio survey, Vol. 347, Monthly Notices of the Royal Astronomical Society, Volume 347, Issue 3, pp. 787-794., 347, 787

Blake, C. & Wall, J. 2002a, Monthly Notices of the Royal Astronomical Society, 329, L37

Blake, C. & Wall, J. 2002b, Monthly Notices of the Royal Astronomical Society, 337, 993

Bonzini, M., Padovani, P., Mainieri, V., et al. 2013, The sub-mJy radio sky in the Extended Chandra Deep Field-South: source population, Vol. -1, Monthly Notices of the Royal Astronomical Society, -1, 2553

Boughn, S. & Crittenden, R. 2004, A correlation between the cosmic microwave background and large-scale structure in the Universe, Vol. 427, Nature, 427, 45

Brammer, G. B., van Dokkum, P. G., & Coppi, P. 2008, The Astrophysical Journal, 686, 1503

Brammer, G. B., Whitaker, K. E., van Dokkum, P. G., et al. 2011, The Number Density and Mass Density of Star-forming and Quiescent Galaxies at 0.4 <= z <= 2.2, Vol. 739, The Astrophysical Journal, 739, 24

Brown, M. J. I., Jannuzi, B. T., Floyd, D. J. E., & Mould, J. R. 2011, The Astrophysical Journal Letters, 731, L41

Brown, M. J. I., Zheng, Z., White, M., et al. 2008, Red Galaxy Growth and the Halo Occupation Distribution, Vol. 682, The Astrophysical Journal, 682, 937

Bruzual, G. & Charlot, S. 2003, Monthly Notices of the Royal Astronomical Society, 344, 1000

Cabré, A., Gaztañaga, E., Manera, M., Fosalba, P., & Castander, F. 2006, Cross-correlation of Wilkinson Microwave Anisotropy Probe third-year data and the Sloan Digital Sky Survey DR4 galaxy survey: new evidence for dark energy, Vol. 372, MNRAS, 372, L23

Camera, S., Santos, M. G., Bacon, D. J., et al. 2012, Monthly Notices of the Royal Astronomical Society, 427, 2079

Cameron, E. 2011, Publications of the Astronomical Society of Australia, 28, 128

Cameron, E. 2013, Publications of the Astronomical Society of Australia, 28, 128

Carilli, C. & Walter, F. 2013, Annual Review of Astronomy and Astrophysics, 51, 105

Carlberg, R. G., Yee, H. K. C., Morris, S. L., et al. 2000, Galaxy Clustering Evolution in the CNOC2 High-Luminosity Sample, Vol. 542, The Astrophysical Journal, 542, 57

Chabrier, G. 2003, Publications of the Astronomical Society of the Pacific, 115, 763

Chen, S. & Schwarz, D. J. 2015, The angular two-point correlation of NVSS galaxies revisited, Vol. 591, Astronomy & Astrophysics, Volume 591, id.A135, 11 pp., 591

Chen, S. & Schwarz, D. J. 2016, Angular two-point correlation of NVSS galaxies revisited, Vol. 591, Astronomy and Astrophysics, 591, A135

Chen, Y.-M., Kauffmann, G., Heckman, T. M., et al. 2013, Monthly Notices of the Royal Astronomical Society, 429, 2643

Chi, S., Barthel, P. D., & Garrett, M. A. 2013, Deep, wide-field, global VLBI observations of the Hubble deep field north (HDF-N) and flanking fields (HFF), Vol. 550, Astronomy & Astrophysics, 550, A68

Christiansen, W. N., Frater, R. H., Watkinson, A., et al. 1977, Observations of 15 southern extragalactic sources with the Fleurs synthesis telescope, Vol. 181, MNRAS, 181, 183

Collier, J. D., Banfield, J. K., Norris, R. P., et al. 2014, Infrared-faint radio sources: a new population of high-redshift radio galaxies, Vol. 439, MNRAS, 439, 545

Condon, J. J. 1992, Radio emission from normal galaxies, Vol. 30, ARA&A, 30, 575

Condon, J. J., Cotton, W. D., Greisen, E. W., et al. 1998, The NRAO VLA Sky Survey, Vol. 115, The Astrophysical Journal, 115, 1693

Condon, J. J., Huang, Z.-P., Yin, Q. F., & Thuan, T. X. 1991, Compact starbursts in ultraluminous infrared galaxies, Vol. 378, The Astrophysical Journal, 378, 65

Crenshaw, D. M., Kraemer, S. B., & Gabel, J. R. 2003, The Astronomical Journal, 126, 1690

Cress, C. M., Helfand, D. J., Becker, R. H., Gregg, M. D., & White, R. L. 1996, The Angular Two-Point Correlation Function for the FIRST Radio Survey, Vol. 473, The Astrophysical Journal, 473, 7

Croton, D. J., Springel, V., White, S. D. M., et al. 2006, Monthly Notices of the Royal Astronomical Society, 365, 11

Croton, D. J., Stevens, A. R. H., Tonini, C., et al. 2016, Semi-Analytic Galaxy Evolution (SAGE): Model Calibration and Basic Results, Vol. 222, The Astrophysical Journals, 222, 22

Daddi, E., Cimatti, A., Broadhurst, T., et al. 2002, The K20 survey. II. The different spatial clustering of z ˜ 1 old and dusty star-forming EROs, Vol. 384, Astronomy and Astrophysics, 384, L1

Dark Energy Survey Collaboration, Abbott, T., Abdalla, F. B., et al. 2016, The Dark Energy Survey: more than dark energy - an overview, Vol. 460, Monthly Notices of the Royal Astronomical Society, 460, 1270

Davis, M. & Peebles, P. J. E. 1983, A survey of galaxy redshifts. V - The two-point position and velocity correlations, Vol. 267, The Astrophysical Journal, 267, 465

De Breuck, C., van Breugel, W., Stanford, S. A., et al. 2002, The Astronomical Journal, 123, 637

de Zotti, G., Persic, M., Franceschini, A., et al. 1990, Constraints on large-scale clustering from the autocorrelation properties of the X-ray background, Vol. 351, The Astrophysical Journal, 351, 22

Deller, A. T. & Middelberg, E. 2014, The Astronomical Journal, 147, 14

Donley, J. L., Koekemoer, A. M., Brusa, M., et al. 2012, The Astrophysical Journal, 748, 142

Draper, A. R. & Ballantyne, D. R. 2012, The Astrophysical Journal, 751, 72

Dressel, L. L. 1981, A statistical study of radio emission in E and S0 galaxies, Vol. 245, The Astrophysical Journal, 245, 25

Dunkley, J., Komatsu, E., Nolta, M. R., et al. 2009, Five-Year Wilkinson Microwave Anisotropy Probe Observations: Likelihoods and Parameters from the WMAP Data, Vol. 180, The Astrophysical Journal Supplement, 180, 306

Dunlop, J. S. & Peacock, J. A. 1990, The Redshift Cut-Off in the Luminosity Function of Radio Galaxies and Quasars, Vol. 247, Monthly Notices of the Royal Astronomical Society, 247, 19

Eales, S., Rawlings, S., Law-Green, D., Cotter, G., & Lacy, M. 1997, A first sample of faint radio sources with virtually complete redshifts. I - Infrared images, the Hubble diagram and the alignment effect, Vol. 291, Monthly Notices of the Royal Astronomical Society, 291

Elyiv, A., Clerc, N., Plionis, M., et al. 2012, Angular correlation functions of X-ray point-like sources in the full exposure XMM-LSS field, Vol. 537, Astronomy and Astrophysics, 537, A131

Emonts, B. H. C., Feain, I., Mao, M., et al. 2008, Molecular CO (1-0) gas in the z 2 radio galaxy MRC 0152-209, Physics, 1

Emonts, B. H. C., Norris, R. P., Feain, I., et al. 2014, Monthly Notices of the Royal Astronomical Society, 438, 2898

Fabbiano, G., Gioia, I. M., & Trinchieri, G. 1989, Radio emission and the hot interstellar medium of early-type galaxies, Vol. 347, The Astrophysical Journal, 347, 127

Fanaroff, B. L. & Riley, J. M. 1974, The morphology of extragalactic radio sources of high and low luminosity, Monthly Notices of the Royal Astronomical Society, Vol. 167, p. 31P-36P (1974)

Fixsen, D. J., Cheng, E. S., Gales, J. M., et al. 1996, The Cosmic Microwave Background Spectrum from the Full COBE FIRAS Data Set, Vol. 473, The Astrophysical Journal, 473, 576

Fosalba, P., Crocce, M., Gaztañaga, E., & Castander, F. J. 2015, The MICE grand challenge lightcone simulation - I. Dark matter clustering, Vol. 448, Monthly Notices of the Royal Astronomical Society, 448, 2987

Giacconi, R., Rosati, P., Tozzi, P., et al. 2001, The Astrophysical Journal, 551, 624

Giannantonio, T., Crittenden, R., Nichol, R., & Ross, A. J. 2012, The significance of the integrated Sachs-Wolfe effect revisited, Vol. 426, Monthly Notices of the Royal Astronomical Society, 426, 2581

Giannantonio, T., Ross, A. J., Percival, W. J., et al. 2014, Physical Review D, 89, 023511

Giannantonio, T., Scranton, R., Crittenden, R. G., et al. 2008, Physical Review D, 77, 123520

Górski, K. M., Hivon, E., Banday, A. J., et al. 2005, HEALPix: A Framework for High-Resolution Discretization and Fast Analysis of Data Distributed on the Sphere, Vol. 622, The Astrophysical Journal, 622, 759

Griffith, M. R. 1993, The Parkes-MIT-NRAO (PMN) survey of the southern sky, PhD thesis, Massachusetts Institute of Technology

Grogin, N. A., Kocevski, D. D., Faber, S. M., et al. 2011, The Astrophysical Journal Supplement Series, 197, 35

Groth, E. J. & Peebles, P. J. E. 1977, Statistical analysis of catalogs of extragalactic objects. VII - Two- and three-point correlation functions for the high-resolution Shane-Wirtanen catalog of galaxies, Vol. 217, The Astrophysical Journal, 217, 385

Guesten, R. & Mezger, P. G. 1982, Star formation and abundance gradients in the galaxy, Vol. 26, Vistas in Astronomy, 26, 159

Guzzo, L., Strauss, M. A., Fisher, K. B., Giovanelli, R., & Haynes, M. P. 1997, Redshift-Space Distortions and the Real-Space Clustering of Different Galaxy Types, Vol. 489, The Astrophysical Journal, 489, 37

Hao, H., Sargent, M. T., Elvis, M., et al. 2014, Inter-comparison of Radio-Loudness Criteria for Type 1 AGNs in the XMM-COSMOS Survey, 12

Helou, G., Soifer, B. T., & Rowan-Robinson, M. 1985, Thermal infrared and nonthermal radio - Remarkable correlation in disks of galaxies, Vol. 298, The Astrophysical Journal, 298, L7

Herrera Ruiz, N., Middelberg, E., Norris, R. P., & Maini, A. 2016, Unveiling the origin of the radio emission in radio-quiet quasars, Vol. 589, A&A, 589, L2

Herzog, A., Norris, R. P., Middelberg, E., et al. 2015, Infrared-faint radio sources remain undetected at far-infrared wavelengths. Deep photometric observations using the Herschel Space Observatory, Vol. 580, A&A, 580, A7

Heywood, I., Jarvis, M. J., Baker, A. J., et al. 2016, A deep / wide 1-2 GHz snapshot survey of SDSS Stripe 82 using the Karl G. Jansky Very Large Array in a compact hybrid configuration, Vol. 460, Monthly Notices of the Royal Astronomical Society, Volume 460, Issue 4, p.4433-4452, 460, 4433

Hickox, R. C., Mullaney, J. R., Alexander, D. M., et al. 2014, The Astrophysical Journal, 782, 9

Hildebrandt, H., van Waerbeke, L., & Erben, T. 2009, CARS: The CFHTLS-Archive-Research Survey. III. First detection of cosmic magnification in samples of normal high-z galaxies, Vol. 507, Astronomy and Astrophysics, 507, 683

Hivon, E., Hansen, F. K., Wandelt, B. D., et al. 2016, HEALPix Fortran Facility User GUide

Ho, S., Hirata, C., Padmanabhan, N., Seljak, U., & Bahcall, N. 2008, Physical Review D, 78, 043519

Hodge, J. A., Becker, R. H., White, R. L., Richards, G. T., & Zeimann, G. R. 2011, The Astronomical Journal, 142, 3

Hopkins, P. F. & Elvis, M. 2010, Monthly Notices of the Royal Astronomical Society, 401, 7

Hopkins, P. F., Hernquist, L., Cox, T. J., & Kereš, D. 2008, The Astrophysical Journal Supplement Series, 175, 356

Hunter, J. D. 2007, Computing In Science & Engineering, 9, 90

Jarvis, M., Bacon, D., Blake, C., et al. 2015, Cosmology with SKA Radio Continuum Surveys, Advancing Astrophysics with the Square Kilometre Array (AASKA14), 18

Jarvis, M. J., Rawlings, S., Eales, S., et al. 2001, A sample of 6C radio sources designed to find objects at redshift > 4: III — imaging and the radio galaxy K-z relation, Monthly Notices of the Royal Astronomical Society, Volume 326, Issue 4, pp. 1585-1600., 21

Johnston, H. M., Sadler, E. M., Cannon, R., et al. 2008, Monthly Notices of the Royal Astronomical Society, 384, 692

Jones, E., Oliphant, T., Peterson, P., et al. 2001–, SciPy: Open source scientific tools for Python, [Online; accessed 2015-02-18]

Jones, P. A. & McAdam, W. B. 1996, The head-tail and wide-angle-tail radio galaxies in cluster A3627, Vol. 282, MNRAS, 282, 137

Kaiser, N. 1984, On the spatial correlations of Abell clusters, Vol. 284, The Astrophysical Journall, 284, L9

Karim, A., Schinnerer, E., Martínez-Sansigre, A., et al. 2011, The Astrophysical Journal, 730, 61

Karouzos, M., Britzen, S., Eckart, A., Witzel, A., & Zensus, A. 2010, Tracing the merger-driven evolution of active galaxies using the CJF sample, Vol. 519, Astronomy and Astrophysics, 519, A62

Karouzos, M., Jarvis, M. J., & Bonfield, D. 2014, Monthly Notices of the Royal Astronomical Society, 439, 861

Kauffmann, G., Heckman, T. M., & Best, P. N. 2008, Monthly Notices of the Royal Astronomical Society, 384, 953

Kawinwanichakij, L., Papovich, C., Quadri, R. F., et al. 2014, The Astrophysical Journal, 792, 103

Keel, W. C., White III, R. E., Owen, F. N., & Ledlow, M. J. 2006, The Astronomical Journal, 132, 2233

Kellermann, K. I. 1994, The Astronomical Journal, 108

Kellermann, K. I., Sramek, R., Schmidt, M., Shaffer, D. B., & Green, R. 1989, VLA observations of objects in the Palomar Bright Quasar Survey, Vol. 98, The Astronomical Journal, 98, 1195

Kennicutt, R. C. 1998, The Astrophysical Journal, 498, 541

Kewley, L. J., Heisler, C. A., Dopita, M. A., et al. 2000, The Astrophysical Journal, 530, 704

Kim, J.-W., Edge, A. C., Wake, D. A., & Stott, J. P. 2011, Clustering properties of high-redshift red galaxies in SA22 from the UKIDSS Deep eXtragalactic Survey, Vol. 410, Monthly Notices of the Royal Astronomical Society, 410, 241

Kimball, A. E., Kellermann, K. I., Condon, J. J., & Perley, R. A. 2011, The Two-Component Radio Luminosity Function of QSOs: Star Formation and AGN, ApJ Letters EVLA Special Edition, 1

Kooiman, B. L., Burns, J. O., & Klypin, A. A. 1995, Two-Point Angular Correlation Function for the Green Bank 4.85 GHz Sky Survey, Vol. 448, The Astrophysical Journal, 448, 500

Kovač, K., Somerville, R. S., Rhoads, J. E., Malhotra, S., & Wang, J. 2007, Clustering of Lyα Emitters at z ˜ 4.5, Vol. 668, The Astrophysical Journal, 668, 15

Kowalski, M., Rubin, D., Aldering, G., et al. 2008, Improved Cosmological Constraints from New, Old, and Combined Supernova Data Sets, Vol. 686, The Astrophysical Journal, 686, 749

Kriek, M., van Dokkum, P. G., Labbé, I., et al. 2009, The Astrophysical Journal, 700, 221

Kundić, T. 1997, The Quasar-Quasar Correlation Function in the Palomar Transit Grism Survey, Vol. 482, The Astrophysical Journal, 482, 631

Lacki, B. C., Thompson, T. A., & Quataert, E. 2010, The Physics of the Far-infrared-Radio Correlation. I. Calorimetry, Conspiracy, and Implications, Vol. 717, The Astrophysical Journal, 717, 1

Laing, R. A., Riley, J. M., & Longair, M. S. 1983, Bright radio sources at 178 MHz - Flux densities, optical identifications and the cosmological evolution of powerful radio galaxies, Vol. 204, Monthly Notices of the Royal Astronomical Society (ISSN 0035-8711), 204, 151

Landy, S. D. & Szalay, A. S. 1993, Bias and variance of angular correlation functions, Vol. 412, The Astrophysical Journal, 412, 64

Le Fevre, O., Hudon, D., Lilly, S. J., et al. 1996, The Canada-France Redshift Survey. VIII. Evolution of the Clustering of Galaxies from Z approximately 1, Vol. 461, The Astrophysical Journal, 461, 534

Ledlow, M. J., Owen, F. N., Yun, M. S., & Hill, J. M. 2001, The Astrophysical Journal, 552, 120

Lilly, S. J. & Longair, M. S. 1984, Stellar populations in distant radio galaxies, Vol. 211, Monthly Notices of the Royal Astronomical Society (ISSN 0035-8711), 211, 833

Lilly, S. J. & Prestage, R. M. 1987, Surface photometry of powerful radio galaxies. II - Relations with the radio, optical, and clustering properties, Vol. 225, Monthly Notices of the Royal Astronomical Society (ISSN 0035-8711), 225, 531

Limber, D. N. 1953, The Analysis of Counts of the Extragalactic Nebulae in Terms of a Fluctuating Density Field., Vol. 117, The Astrophysical Journal, 117, 134

Lindsay, S. N. 2015, Tracing Large-Scale Structure with Radio Sources, PhD thesis, University of Hertfordshire

Lindsay, S. N., Jarvis, M. J., & McAlpine, K. 2014, Evolution in the bias of faint radio sources to z = 2.2, Vol. 440, Monthly Notices of the Royal Astronomical Society, 440, 2322

Lindsay, S. N., Jarvis, M. J., Santos, M. G., et al. 2014, Galaxy and Mass Assembly (GAMA): The evolution of bias in the radio source population to z ˜ 1.5, Vol. 440, Monthly Notices of the Royal Astronomical Society, Volume 440, Issue 2, p.1527-1541, 440, 1527

Loan, A. J., Wall, J. V., & Lahav, O. 1997, The correlation function of radio sources, Vol. 286, Monthly Notices of the Royal Astronomical Society, 286, 994

Longair, M. S. & Seldner, M. 1979, The clustering of galaxies about extragalactic radio sources, Vol. 189, MNRAS, 189, 433

Mantz, A., Allen, S. W., Rapetti, D., & Ebeling, H. 2010, The observed growth of massive galaxy clusters - I. Statistical methods and cosmological constraints, Vol. 406, Monthly Notices of the Royal Astronomical Society, 406, 1759

Mao, M. Y., Huynh, M. T., Norris, R. P., et al. 2011, The Astrophysical Journal, 731, 79

Mao, M. Y., Huynh, M. T., Norris, R. P., et al. 2012, Proceedings of the International Astronomical Union, 7, 404

Mao, M. Y., Norris, R. P., Emonts, B., et al. 2014a, Monthly Notices of the Royal Astronomical Society: Letters, 440, L31

Mao, M. Y., Owen, F., Duffin, R., et al. 2014b, Monthly Notices of the Royal Astronomical Society, 446, 4176

Mauch, T., Murphy, T., Buttery, H. J., et al. 2003, SUMSS: a wide-field radio imaging survey of the southern sky - II. The source catalogue, Vol. 342, Monthly Notices of the Royal Astronomical Society, 342, 1117

Mauch, T. & Sadler, E. M. 2007, Monthly Notices of the Royal Astronomical Society, 375, 931

McCarthy, P. J., Carlberg, R. G., Chen, H.-W., et al. 2001, The Las Campanas Infrared Survey: Early-Type Galaxy Progenitors beyond z=1, Vol. 560, The Astrophysical Journal Letters, 560, L131

McCracken, H. J., Le Fèvre, O., Brodwin, M., et al. 2001, The Canada-France deep fields survey. I: 100,000 galaxies, 1 deg^2: a precise measurement of omega(theta) to I(AB) ˜ 25, Vol. 376, Astronomy and Astrophysics, 376, 756

McNamara, B. R., Nulsen, P. E. J., Wise, M. W., et al. 2005, Nature, 433, 45

Mellier, Y., Waerbeke, L. V., Bernardeau, F., & Tereno, I. 2003, Cosmological Weak Lensing, in Astronomy, Cosmology and Fundamental Physics, ed. P. A. Shaver, L. Dilella, & A. Giménez, 25

Middelberg, E., Deller, A., Morgan, J., et al. 2011, Wide-field VLBA observations of the Chandra deep field South, Vol. 526, Astronomy & Astrophysics, 526, A74

Middelberg, E., Deller, A. T., Norris, R. P., et al. 2013, Mosaiced wide-field VLBI observations of the Lockman Hole/XMM, Vol. 551, Astronomy & Astrophysics, 551, A97

Miller, L., Peacock, J. A., & Mead, A. R. G. 1990, The bimodal radio luminosity function of quasars, Vol. 244, Royal Astronomical Society, 244, 207

Miller, N. A., Bonzini, M., Fomalont, E. B., et al. 2013, The Astrophysical Journal Supplement Series, 205, 13

More, S., van den Bosch, F. C., Cacciato, M., et al. 2009, Monthly Notices of the Royal Astronomical Society, 392, 801

Morganti, R., Frieswijk, W., Oonk, R. J. B., Oosterloo, T., & Tadhunter, C. 2013, Tracing the extreme interplay between radio jets and the ISM in IC 5063, Vol. 552, Astronomy & Astrophysics, 552, L4

Morić, I., Smolčić, V., Kimball, A., et al. 2010, The Astrophysical Journal, 724, 779

Moster, B. P., Somerville, R. S., Maulbetsch, C., et al. 2010, The Astrophysical Journal, 710, 903

Nesvadba, N. P. H., Boulanger, F., Salomé, P., et al. 2010, Energetics of the molecular gas in the H 2 luminous radio galaxy 3C 326: Evidence for negative AGN feedback, Vol. 521, Astronomy and Astrophysics, 521, A65

Nolta, M. R., Wright, E. L., Page, L., et al. 2004, First Year Wilkinson Microwave Anisotropy Probe Observations: Dark Energy Induced Correlation with Radio Sources, Vol. 608, The Astrophysical Journal, 608, 10

Norberg, P., Baugh, C. M., Hawkins, E., et al. 2002, The 2dF Galaxy Redshift Survey: the dependence of galaxy clustering on luminosity and spectral type, Vol. 332, Monthly Notices of the Royal Astronomical Society, 332, 827

Norris, R., Basu, K., Brown, M., et al. 2015, The SKA Mid-frequency All-sky Continuum Survey: Discovering the unexpected and transforming radio-astronomy, Advancing Astrophysics with the Square Kilometre Array (AASKA14), 86

Norris, R. P., Afonso, J., Appleton, P. N., et al. 2006, The Astronomical Journal, 132, 2409

Norris, R. P., Hopkins, A. M., & Afonso, J. 2011, Publications of the Astronomical Society of Australia, 28, 215

Norris, R. P., Tingay, S., Phillips, C., et al. 2007, Monthly Notices of the Royal Astronomical Society, 378, 1434

Nulsen, P. E. J. & McNamara, B. R. 2013, AGN feedback in clusters: shock and sound heating, Astronomische Nachrichten, Vol.334, Issue 4-5, p.386, 4

O'Brien, A., Norris, R., Tothill, N. F. H., & Filipovic, M. D. 2015, The ATLAS-SPT radio survey of cluster galaxies, in The Many Facets of Extragalactic Radio Surveys: Towards New Scientific Challenges, 45

Oosterloo, T., Verheijen, M., & van Cappellen, W. 2009, Apertif - the focal-plane array system for the WSRT, 7

Overzier, R. A., Röttgering, H. J. A., Rengelink, R. B., & Wilman, R. J. 2003, The spatial clustering of radio sources in NVSS and FIRST; implications for galaxy clustering evolution, Vol. 405, Astronomy and Astrophysics, 405, 53

Owen, F. N. & Laing, R. A. 1989, CCD surface photometry of radio galaxies. I - FR class I and II sources, Vol. 238, Monthly Notices of the Royal Astronomical Society (ISSN 0035-8711), 238, 357

Padovani, P., Miller, N., Kellermann, K. I., et al. 2011, The VLA Survey of the Chandra Deep Field South. V. Evolution and Luminosity Functions of sub-mJy radio sources and the issue of radio emission in radio-quiet AGN, 19

Papovich, C., Labbé, I., Quadri, R., et al. 2014, ZFOURGE/CANDELS: On the Evolution of M* Galaxy Progenitors from z=3 to 0.5, ArXiv e-prints

Parra, R., Conway, J. E., Aalto, S., et al. 2010, The Astrophysical Journal, 720, 555

Peebles, P. J. E. 1980, The large-scale structure of the universe

Percival, W. J., Reid, B. A., Eisenstein, D. J., et al. 2010, Baryon acoustic oscillations in the Sloan Digital Sky Survey Data Release 7 galaxy sample, Vol. 401, Monthly Notices of the Royal Astronomical Society, 401, 2148

Pérez, F. & Granger, B. E. 2007, Computing in Science and Engineering, 9, 21

Phillipps, S., Fong, R., Fall, R. S. E. S. M., & MacGillivray, H. T. 1978, Correlation analysis deep galaxy samples - 1. Techniques with applications to a two-colour sample, Vol. 182, MNRAS, 182, 673

Planck Collaboration, Ade, P. A. R., Aghanim, N., et al. 2016, Planck 2015 results. XVI. Isotropy and statistics of the CMB, Vol. 594, Astronomy and Astrophysics, 594, A16

Planck Collaboration, Ade, P. A. R., Aghanim, N., et al. 2013, Planck 2013 results. XVI. Cosmological parameters, eprint arXiv:1303.5076

Raccanelli, A., Zhao, G.-B., Bacon, D. J., & Jarvis, M. J. 2011, Cosmological Measurements with Forthcoming Radio Continuum Surveys, eprint arXiv:1108.0930

Raccanelli, A., Zhao, G.-B., Bacon, D. J., et al. 2012, Monthly Notices of the Royal Astronomical Society, 424, 801

Rafter, S. E., Crenshaw, D. M., & Wiita, P. J. 2011, Radio Properties of Low-redshift Broad-line Active Galactic Nuclei Including Extended Radio Sources, Vol. 141, AJ, 141, 85

Ramos Almeida, C., Levenson, N. A., Rodríguez Espinosa, J. M., et al. 2010, Proceedings of the International Astronomical Union, 5, 132

Rassat, A., Land, K., Lahav, O., & Abdalla, F. B. 2007, Cross-correlation of 2MASS and WMAP 3: implications for the integrated Sachs-Wolfe effect, Vol. 377, MNRAS, 377, 1085

Reddick, R. M., Wechsler, R. H., Tinker, J. L., & Behroozi, P. S. 2013, The Astrophysical Journal, 771, 30

Rees, G. A., Norris, R. P., Spitler, L. R., Herrera-Ruiz, N., & Middelberg, E. 2016, Are the hosts of VLBI-selected radio-AGN different to those of radio-loud AGN?, Vol. 458, MNRAS, 458, L49

Rees, G. A., Spitler, L. R., Norris, R. P., et al. 2016, Monthly Notices of the Royal Astronomical Society, 455, 2731

Rengelink, R. & et al. 1998, Astrophysics and Space Science Library, Vol. 226, The Westerbork Northern Sky Survey: Current Status of the Survey and the Study of Large Scale Structure, ed. M. N. Bremer, N. Jackson, & I. Perez-Fournon, 226, 143

Rieke, G. H., Young, E. T., Engelbracht, C. W., et al. 2004, The Astrophysical Journal Supplement Series, 154, 25

Robitaille, T. P., Tollerud, E. J., Greenfield, P., et al. 2013, Astropy: A community Python package for astronomy, Vol. 558, Astronomy & Astrophysics, 558, A33

Rocca-Volmerange, B., Drouart, G., De Breuck, C., et al. 2013, Monthly Notices of the Royal Astronomical Society, 429, 2780

Sabater, J., Best, P. N., & Argudo-Fernandez, M. 2013, Monthly Notices of the Royal Astronomical Society, 430, 638

Sachs, R. K. & Wolfe, A. M. 1967, Perturbations of a Cosmological Model and Angular Variations of the Microwave Background, Vol. 147, The Astrophysical Journal, 147, 73

Sadler, E. M., Jenkins, C. R., & Kotanyi, C. G. 1989, Low-luminosity radio sources in early-type galaxies, Vol. 240, MNRAS, 240, 591

Schawinski, K., Urry, C. M., Simmons, B. D., et al. 2014, Monthly Notices of the Royal Astronomical Society, 440, 889

Schinnerer, E., Carilli, C. L., Scoville, N. Z., et al. 2004, The Astronomical Journal, 128, 1974

Schinnerer, E., Sargent, M. T., Bondi, M., et al. 2010, The Astrophysical Journal Supplement Series, 188, 384

Scranton, R., Connolly, A. J., Nichol, R. C., et al. 2003, Physical Evidence for Dark Energy, ArXiv Astrophysics e-prints

Scranton, R., Ménard, B., Richards, G. T., et al. 2005, Detection of Cosmic Magnification with the Sloan Digital Sky Survey, Vol. 633, The Astrophysical Journal, 633, 589

Seymour, N., Altieri, B., De Breuck, C., et al. 2012, The Astrophysical Journal, 755, 146

Seymour, N., Dwelly, T., Moss, D., et al. 2008, Monthly Notices of the Royal Astronomical Society, 386, 1695

Silk, J. & Nusser, A. 2010, The Astrophysical Journal, 725, 556

Simpson, C., Westoby, P., Arumugam, V., et al. 2013, The prevalence of AGN feedback in massive galaxies at z˜1

Skrutskie, M. F., Cutri, R. M., Stiening, R., et al. 2006, The Two Micron All Sky Survey (2MASS), Vol. 131, The Astronomical Journal, 131, 1163

Smoot, G. F., Bennett, C. L., Kogut, A., et al. 1992, Structure in the COBE differential microwave radiometer first-year maps, Vol. 396, The Astrophysical Journal Letters, 396, L1

Spergel, D. N., Bean, R., Dore, O., et al. 2007, The Astrophysical Journal Supplement Series, 170, 377

Spitler, L. R., Labbé, I., Glazebrook, K., et al. 2012, The Astrophysical Journal, 748, L21

Spitler, L. R., Straatman, C. M. S., Labbé, I., et al. 2014, The Astrophysical Journal, 787, L36

Springel, V., White, S. D. M., Jenkins, A., et al. 2005, Nature, 435, 629

Stevens, J. A., Ivison, R. J., Dunlop, J. S., et al. 2003, The formation of cluster elliptical galaxies as revealed by extensive star formation, Nature, Volume 425, Issue 6955, pp. 264-267 (2003).

Story, K. T., Reichardt, C. L., Hou, Z., et al. 2013, A Measurement of the Cosmic Microwave Background Damping Tail from the 2500-Square-Degree SPT-SZ Survey, Vol. 779, The Astrophysical Journal, 779, 86

Straatman, C. M. S., Labbé, I., Spitler, L. R., et al. 2014, The Astrophysical Journal, 783, L14

Straatman, C. M. S., Spitler, L. R., Quadri, R. F., et al. 2016, The Astrophysical Journal, 830, 51

Szapudi, I., Prunet, S., Pogosyan, D., Szalay, A. S., & Bond, J. R. 2001, The Astrophysical Journal, 548, L115

Szapudi, I., Prunet, S., Pogosyan, D., Szalay, A. S., & Bond, J. R. 2001, Fast Cosmic Microwave Background Analyses via Correlation Functions, Vol. 548, The Astrophysical Journal Letters, 548, L115

Tilvi, V., Papovich, C., Tran, K.-V. H., et al. 2013, The Astrophysical Journal, 768, 56

Tomczak, A. R., Quadri, R., Tran, K., et al. 2014, Galaxy Stellar Mass Functions from ZFOURGE/CANDELS: An Excess of Low-Mass Galaxies Since z=2 and the Rapid Buildup of Quiescent Galaxies, American Astronomical Society

Ulvestad, J. S., Antonucci, R. R. J., & Barvainis, R. 2005, The Astrophysical Journal, 621, 123

Urry, C. M. & Padovani, P. 1995, Unified Schemes for Radio-Loud Active Galactic Nuclei, Vol. 107, Publications of the Astronomical Society of the Pacific, 107, 803

van der Kruit, P. C. 1973, High-resolution Radio Continuum Observations of Bright Spiral Galaxies at 1415 MHz: A General Discussion, Vol. 29, A&A, 29, 263

van der Wel, A., Franx, M., van Dokkum, P. G., et al. 2014, The Astrophysical Journal, 788, 28

Vron-Cetty, M. P. & Vron, P. 2001, Astronomy and Astrophysics, 375, 791

Wake, D. A., Whitaker, K. E., Labbé, I., et al. 2011, Galaxy Clustering in the NEWFIRM Medium Band Survey: The Relationship Between Stellar Mass and Dark Matter Halo Mass at $1 < z < 2$, Vol. 728, The Astrophysical Journal, 728, 46

Wang, L., Cooray, A., Farrah, D., et al. 2011, HerMES: detection of cosmic magnification of submillimetre galaxies using angular cross-correlation, Vol. 414, Monthly Notices of the Royal Astronomical Society, 414, 596

Wayth, R. B., Lenc, E., Bell, M. E., et al. 2015, GLEAM: The GaLactic and Extragalactic All-Sky MWA Survey, Vol. 32, Publications of the Astronomical Society of Australia, 32, e025

Webster, A. & Pearson, T. J. 1977, The clustering of radio sources. IV - The 5C 5, 5C 6 and 5C 7 surveys, Vol. 179, Monthly Notices of the Royal Astronomical Society, 179, 517

Whitaker, K. E., Labbe, I., van Dokkum, P. G., et al. 2011, The NEWFIRM Medium-band Survey: Photometric Catalogs, Redshifts and the Bimodal Color Distribution of Galaxies out to z˜3, 24

White, R. L., Becker, R. H., Helfand, D. J., & Gregg, M. D. 1997, A Catalog of 1.4 GHz Radio Sources from the FIRST Survey, Vol. 475, The Astrophysical Journal, 475, 479

White, R. L., Helfand, D. J., Becker, R. H., Glikman, E., & de Vries, W. 2007, The Astrophysical Journal, 654, 99

Whittam, I. 2014, Exploring the faint source population at 15.7 GHz, PhD thesis, Cavendish Astrophysics, University of Cambridge

Willmer, C. N. A., da Costa, L. N., & Pellegrini, P. S. 1998, Southern Sky Redshift Survey: Clustering of Local Galaxies, Vol. 115, The Astronomical Journal, 115, 869

Wilman, R. J., Miller, L., Jarvis, M. J., et al. 2008, A semi-empirical simulation of the extragalactic radio continuum sky for next generation radio telescopes, Vol. 1348, Monthly Notices of the Royal Astronomical Society, 1348, 1335

Wood, K. S., Meekins, J. F., Yentis, D. J., et al. 1984, The HEAO A-1 X-ray source catalog, Vol. 56, The Astrophysical Journal Supplement Series, 56, 507

Wright, E. L., Eisenhardt, P. R. M., Mainzer, A. K., et al. 2010, The Wide-field Infrared Survey Explorer (WISE): Mission Description and Initial On-orbit Performance, Vol. 140, The Astronomical Journal, 140, 1868

Wuyts, S., Förster Schreiber, N. M., Lutz, D., et al. 2011, The Astrophysical Journal, 738, 106

Wuyts, S., Labbe, I., Franx, M., et al. 2007, The Astrophysical Journal, 655, 51

Xia, J.-Q., Viel, M., Baccigalupi, C., et al. 2010, Primordial Non-Gaussianity and the NRAO VLA Sky Survey, Vol. 717, The Astrophysical Journall, 717, L17

Yang, X., Mo, H. J., & van den Bosch, F. C. 2009, The Astrophysical Journal, 693, 830

York, D. G., Adelman, J., Anderson, Jr., J. E., et al. 2000, The Sloan Digital Sky Survey: Technical Summary, Vol. 120, The Astronomical Journal, 120, 1579

Yuan, T. T., Nanayakkara, T., Kacprzak, G. G., et al. 2014, KECK/MOSFIRE spectroscopic confirmation of a Virgo-like cluster ancestor at z=2.095, 6

Zehavi, I., Zheng, Z., Weinberg, D. H., et al. 2011, Galaxy Clustering in the Completed SDSS Redshift Survey: The Dependence on Color and Luminosity, Vol. 736, The Astrophysical Journal, 736, 59

Zinn, P.-C., Middelberg, E., Norris, R. P., & Dettmar, R.-J. 2013, The Astrophysical Journal, 774, 66